NONLINEAR REDUCED ORDER MODELS AND DAMAGE DETECTION IN SYSTEMS WITH COMPLEX GEOMETRY

by

Chulwoo Jung

A dissertation submitted in partial fulfillment
of the requirements for the degree of
Doctor of Philosophy
(Mechanical Engineering)
in The University of Michigan
2013

Doctoral Committee:

Associate Professor Bogdan I. Epureanu, Chair
Professor Ronald G. Larson
Assistant Professor Kenn R. Oldham
Professor Armin W. Troesch

To my lovely wife and family

ACKNOWLEDGEMENTS

I would like to express my sincere gratitude to my advisor and chair of my doctoral committee, Professor Bogdan I. Epureanu for giving me the opportunity to pursue my doctoral degree. His continuous support and guidance have made this dissertation possible. I am also thankful to the remaining members of my doctoral committee, Professor Larson, Professor Oldham, and Professor Troesch for their valuable comments and suggestions. I would also like to thank the current and former members of Vibrations and Acoustics Laboratory, including Seunghun Baek, Kiran D'Souza, Colin Fitzner, Darren Holland, Sung-Kwon Hong, Anish Joshi, Joosup Lim, Andrew Madden, Olguta Marinescu, Woochul Nam, Akira Saito, Andrew Sloboda, and Weihan Tang for their insights, suggestions, and friendship. Finally, I would like to express my appreciation to my lovely wife Inae Chung, parents, and sisters for their love, patience, and encouragements.

TABLE OF CONTENTS

LIST OF FIGURES

Figure

LIST OF TABLES

Table

CHAPTER I

Introduction

1.1 Dissertation Objective

The quest for high performance mechanical systems often forces dynamic structures to adopt complex geometry. A well studied example includes the complex geometry of blades inside gas turbine engines. Because the geometry of the blade can have significant effects on turbine performance, a number of research endeavors have been carried out to find better geometry to increase performance. As a consequence, blade geometries continue to evolve in complexity. As the geometric complexity of these and other similar structures grows, the uncertainty in computational predictions of vibration responses also increases. Therefore, it is important to monitor the vibration characteristics (such as frequency and amplitude) for safety of the structures, especially for large and complex air and space structures.

Vibration monitoring systems are greatly needed to forecast sudden failures caused by damages or fatigue fracture. Such vibration monitoring is used to diagnose structural health by analyzing vibrations of the system. However, vibrations of turbomachinery rotors can be affected by several factors, such as multi-stage structural coupling, aerodynamic coupling, damping, damage (i.e., cracks), and mistuning. The vibration analysis of bladed disks in a turbomachinery can be carried out easily if it is assumed that all of

their sectors are identical because cyclic symmetry can be employed. In reality, however, there are unavoidable small differences among the structural properties or geometric characteristics between individual sectors due to manufacturing tolerances, material deviations, and non-uniform operational wear. These small differences are commonly referred to as mistuning. Even though the mistuning level is typically small in terms of individual blade properties, this small mistuning can have a considerable impact on the forced response. Namely, mistuning can cause a localization of vibration to a few blades, which leads to a drastic increase in the response amplitude for those blades. Vibration localization can be induced not only by mistuning but also by damages to the bladed disk, such as cracks. Damages can result during operation, from material defects, and from fatigue. It is well known that cracks can induce a nonlinearity due to crack-closing effect which is a displacement-dependent nonlinearity caused by repetitive opening and closing of crack surfaces. Since the crack-induced nonlinearity can change a vibration localization, it is important to be able to accurately predict the vibration of dynamical systems with piece-wise linear nonlinearity to detect cracks.

Finite element analysis (FEA) has been used to analyze the vibration of structures. If a structure is small and its geometry is simple, then it can be modeled using low dimensional finite element (FE) models. For low dimensional models, full order analysis can be used. For large and complex structures such as turbine bladed disks, however, the system is modeled using high dimensional FE models for accurate analysis. Thus, the computational cost required to analyze full order FE models can often be prohibitive. Thus, reduced order modeling methods have been investigated. However, many methods have been focused on obtaining reduced order models (ROMs) for linear systems. ROMs for linear systems can be efficiently constructed by using approaches based on linear transformations such as component mode synthesis (CMS). Constructing ROMs for systems with nonlinearity

(caused for example by intermittent contact) require careful treatment and new modeling methods. For example, mistuned bladed disks can experience nonlinear vibrations due to cracks. To capture the nonlinearity, the physical degrees of freedom (DOFs) of the nodes on the crack surfaces are typically chosen as active DOFs in the ROMs so that the motion of the nodes in the physical three-dimensional space can be tracked. Therefore, the number of nodes on the crack surfaces significantly affects on the size of the ROMs.

Vibration characteristics such as frequency and amplitude can be used to diagnose damages in dynamic systems. Among the vibration characteristics used, the vibration amplitude is especially important because it can directly affect the life of the system. Predicting the vibration amplitude with efficiency requires the calculation of nonlinear forced responses. One way to obtain the nonlinear forced responses is to use ROMs with direct numerical integration (e.g., by using a variable step Runge-Kutta method). That approach incurs a large computational cost despite the fact that the ROMs are low dimensional. Therefore, to obtain the amplitude of vibration at the resonant frequencies, nonlinear forced responses need to be calculated using more efficient numerical methods such as hybrid frequency/time domain (HFT) methods, which employs the harmonic balanced method. However, computational cost is still large especially when the size of the ROMs is large (e.g., due to a large number of DOFs involved in the nonlinearity). Also, the method requires a iterative calculations to obtain converged solutions.

The primary purpose of this research is to develop efficient and accurate reduce order modeling methods for nonlinear vibration analysis of dynamic structures with complex geometries, and use the modeling methods to detect damages. In particular, the objectives of this research can be summarized as follows:

- To develop an efficient vibration analysis method for analyzing the effect of aerodynamic coupling with structural models in turbomachinery;

- To develop an efficient method to predict nonlinear forced responses of mistuned blade disks with a crack and a novel method to detect cracks in the bladed disks;
- To develop a novel technique to approximate the vibration amplitude at the resonant frequencies of dynamical systems with piecewise-linear nonlinearity;
- To develop efficient reduced order models to capture the effects of (nonlinear) Coulomb friction on the dynamics of combustors.

1.2 Dissertation Background

Vibration monitoring is desirable for robust diagnosis (and prognosis) of structural health. Many systems have coupling between structures, coupling between fluids and structures, and friction damping. In addition, some other factors can induce nonlinear vibrations during operation, such as damages (i.e., cracks).

In this dissertation, novel and efficient methods are developed for capturing the dynamics of the structures subjected to 1) coupling between structures, 2) coupling between fluids and structures, 3) cracks, and 4) friction damping.

1.2.1 Reduced order modeling methods developed for analyzing aerodynamic effects on structures with complex geometry such as bladed disks

Turbomachinery rotors experience aerodynamic loads that induce fluid-structural coupling as well as interblade coupling. These couplings can significantly change the vibration response of mistuned bladed disks. Thus, to carry out accurate vibration analysis, one needs to consider aerodynamic effects. A large amount of research has been performed for coupling aerodynamic and structural models. Early aeroelastic models used simple lumped parameter models for the structure [2–5], which did not quantitatively capture the dynamics of industrial bladed disks. To obtain better quantitative results, structural ROMs

were developed from FE models of the structure, and cantilever blade modes were used to compute the aerodynamic forcing. To understand the aerodynamic coupling between blades and the mistuning effects, Pierre and Murthy [6] used perturbation methods. Later, an iterative approach to determine the eigenvalues and eigenvectors of an aeroelastic system was proposed by Moyroud *et al.* [7]. A technique that uses the ROMs of a structural model developed by Bladh *et al.* [8, 9] combined with inviscid fluid dynamic models investigated flutter and the forced response of single-stage bladed disks [10, 11]. An iterative aeroelastic coupling method that models the aerodynamics by a quasi-three dimensional potential flow and the structure using component mode mistuning (CMM) [12] was developed by He *et al.* [13, 14].

1.2.2 Reduced order modeling approach for analyzing dynamics of structures with nonlinearity and complex geometry

Health monitoring systems for structures with complex geometry (such as turbomachinery rotors) may use measured vibration data. For instance, vibration localization in bladed disks can be detected by monitoring vibration amplitudes. This vibration localization is caused mainly by two reasons: mistuning and damages (such as cracks).

Mistuning refers to small deviations among the structural properties or geometric characteristics of the blades. Even small mistuning may cause localization of vibration energy to a few blades (which can increase vibration amplitudes and stresses). Also, mistuning destroys the cyclic symmetry of bladed disks. A number of studies have been conducted to investigate the effects of mistuning on bladed disks [15–17]. Some of the early studies used lumped parameter models [18–26]. In general, the effects of mistuning can be understood qualitatively by these simple models (in single stage systems) [27–29]. However, these models are only partially able to accurately predict the vibration characteristics of bladed disks [13, 14, 30–32] especially in multi-stage systems [1]. For efficient modeling of blade

mistuning, Lim *et al.* [12] developed the CMM method to generate ROMs for mistuned bladed disks. In CMM, the mistuned bladed disk is partitioned into a tuned bladed disk component and a virtual blade mistuning component. The mistuning component is defined by the differences between the mistuned and the tuned blade mass and stiffness matrices. For the case of small stiffness-only blade-to-blade variations, mistuning becomes simply an eigenvalue mistuning, and can be defined as the difference between the eigenvalues of the mistuned cantilevered blades and the tuned cantilevered blade.

Vibration localization can be induced not only by mistuning but also by damages to the bladed disk. Several investigators have tackled vibration localization due to cracks by assuming that the cracked blade is an Euler-Bernoulli beam or by using a lumped-mass beam model [33–38]. In those studies, the nonlinearity caused by the crack opening and closing was not considered. However, this piece-wise linear nonlinearity may change the dynamic response of the cracked blades significantly [39–41]. The effects of intermittent crack opening and closing have been investigated by a few researchers using time marching and frequency responses based on a bi-linear oscillator representation [42]. Those studies were later extended to a cracked beam model [43] which was validated by comparing the predicted lowest natural frequencies of the cracked beam with experimentally measured values. Effects of multiple closing cracks on a beam were also investigated using dynamic responses [44]. Although these studies succeeded in capturing the effects of the nonlinearity due to cracks, they were limited because the systems considered were very simple structures.

Recently, Saito *et al.* [45,46] presented an efficient reduced-order modeling method for mistuned bladed disks with a cracked blade. They used a hybrid CMS method to obtain ROMs. To calculate the nonlinear forced responses, they used a HFT method based on the harmonic balanced method [47] and fast Fourier transforms. A modal analysis of the

full mistuned bladed disk with a cracked blade was employed to obtain ROMs. Therefore, the computational costs was significant especially when many mistuning patterns have to be considered. This is important when investigating real bladed disks because mistuning patterns are always present and they are usually random.

Nonlinear forced responses of cracked structures can be calculated by a HFT method based on the harmonic balanced method [47]. In particular, the HFT method of Guillen and Pierre [48, 49] was extended to obtain a compact size of ROM by removing linear DOFs [50] using the Craig-Bampton method [51]. The method has been applied for analyzing the vibration of systems with intermittent contact [52, 53]. The HFT method has been numerically validated by comparisons with direct time integration for both simple and complex systems. For example, the HFT method has been validated numerically for ROMs of a cantilevered cracked beam by comparisons with direct time integration [54].

1.2.3 Damage detection in complex structures using vibration characteristics

The reliability and safety of air and space structures are very important. To ensure safety, real-time and on-board health monitoring systems are needed. During normal operation cycle, turbine engines experience high centrifugal stresses as well as high thermal stresses. Because of those stresses, damages can be induced in bladed disks. More importantly, these damages can create a crack over time. If the length of the crack reaches a critical size, it can eventually lead to the burst of the bladed disk and failure of the engine. Thus, it is important to have robust on-board health monitoring systems. Vibration data can be used to monitor structural health. Vibration data can be measured using tip timing [55] in an engine during operation. Tip timing is a non-contacting measurement method which uses optical probes. It can be used to measure the vibration displacements and frequencies of every blade on a rotating bladed disk.

To study vibrations of damaged structures, FEA is often employed. However, the computational cost required to analyze the vibration of full order FE model is frequently prohibitive. To circumvent this difficulty, a novel reduced order modeling approach is introduced. Saito *et al.* [45, 46] presented an reduced order modeling method for mistuned bladed disks with a cracked blade using a hybrid CMS method. They investigated forced responses of a mistuned bladed disk with a cracked blade using a nonlinear cracked blade model [54]. They showed that cracks may lead to nonlinear behavior and the resonant peaks associated with the cracked blade are nonlinear (e.g., for the 10^{th} mode family) in terms of both the amplitude of vibration and the peak frequency. They suggested that localization due to cracks may be distinguishable from localization due to mistuning because localization at the cracked blade was observed to occur for various mode families. However, that observation alone is not sufficient to establish a metric for differentiating localization due to mistuning from localization due to a crack and identifying blades which have cracks.

1.3 Dissertation Outline

The remaining chapters of this dissertation are intended to be self-contained. Therefore, some of the materials are repetitive.

Chapter II introduces efficient reduced order modeling methods to investigate the effects of aerodynamic coupling with structural multi-stage turbomachinery models. The method consists of first creating efficient structural ROMs of a multi-stage rotors. Cyclic symmetry and CMM are used to form single-stage ROMs (using only single sector models and single sector calculations). The approach then combines these single-stage ROMs by projecting the motion at the interface between stages along a set of harmonic shape functions. Next, complex aerodynamic matrices are iteratively calculated for each stage using

an inviscid, irrotational and isentropic flow solver based on the full potential equation. The multi-stage complex aerodynamic matrix is then assembled using each of the single-stage complex aerodynamic matrices. Aeroelastic ROMs are constructed by combining the multi-stage aerodynamic matrix with the multi-stage structural ROMs developed. In this chapter, the effects of a frequency shift due to mistuning on the complex aerodynamic matrix is also accounted for using liner interpolations between columns of the aerodynamic matrix. Additionally, a new classification of complex multi-stage aeroelastic modes is introduced. This classification method first distinguishes the energy distribution of modes amongst stages, and then determines the alignment of the aeroelastic multi-stage modes with single stage modes. Furthermore, the effects of the aerodynamics and mistuning on the multi-stage forced response are explored.

Chapter III proposes a novel methodology to detect the presence of a crack and to predict the nonlinear forced response of mistuned turbomachinery rotors with a cracked blade and mistuning. The combined effects of the crack and mistuning are captured using a novel reduced order modeling method. This method differs from previous techniques which need full-order analysis to construct ROMs for a mistuned bladed disk with a cracked blade whenever mistuning patterns change. First, a hybrid interface method based on CMS is employed to develop ROMs of the tuned system with a cracked blade. Constraint modes are added to model the displacements due to the intermittent contact between the crack surfaces. The DOFs on the crack surfaces are retained as active DOFs so that the physical forces due to the contact/interaction (in the three-dimensional space) can be accurately modeled. Next, the presence of mistuning in the tuned system with a cracked blade is modeled. CMM is used to account for mistuning present in the uncracked blades while the cracked blade is considered as a reference (with no mistuning). By using CMM, high efficiency is obtained when calculating system normal modes of a mistuned

bladed disk for many mistuning patterns, which is one of the important contributions of the proposed modeling method. Next, the resulting (reduced-order) nonlinear equations of motion are solved by applying an alternating frequency/time-domain method. Using these efficient ROMs in a forced response analysis, it is found that the new modeling approach provides significant computational cost savings, while ensuring good accuracy relative to full-order finite element analyses. Furthermore, the effects of the cracked blade on the mistuned system are investigated. A new method is proposed for damage detection. For the first time the proposed approach is able to detect statistically the presence of a crack and to identify which blade of a full bladed disk is cracked. In particular, it is shown that cracks can be distinguished from mistuning.

Chapter IV is devoted to the development of an efficient method to predict vibration amplitudes at the resonant frequencies of dynamical systems with piecewise-linear nonlinearity. This technique is referred to as the bilinear amplitude approximation (BAA). Previously, the amplitudes at the resonant frequencies of piecewise-linear systems were calculated using nonlinear forced responses across frequency ranges of interest using full-order models or (nonlinear) ROMs. The BAA enable accurate predictions of the resonant amplitudes using only a few linear calculations. BAA constructs a single vibration cycle at each resonant frequency to approximate the periodic steady-state response of the system. It is postulated that the steady-state response is piece-wise linear and can be approximated by analyzing the response over two time intervals during which the system behaves linearly. Overall the dynamics is nonlinear, but the system is in a distinct linear state during each of the two time intervals. Thus, the approximated vibration cycle is constructed using linear analyses. The equation of motion for analyzing the vibration of each state is projected along the overlapping space spanned by the linear mode shapes active in each of the states. This overlapping space is where the vibratory energy is transferred from one state to

the other when the system switches from one state to the other. The overlapping space can be obtained using singular value decomposition. The space where the energy is transferred is used together with transition conditions of displacement and velocity compatibility to construct a single vibration cycle and to compute the amplitude of the dynamics. Since the BAA method does not require numerical integration of nonlinear models, computational costs are very low, which is one of the important contributions of the BAA method. In this chapter, the BAA method is first applied to a single-DOF system. Then, a three-DOF system is introduced to demonstrate a more general application of BAA. Finally, the BAA method is applied to a full bladed disk with a crack. Results comparing numerical solutions from full-order nonlinear analysis and results obtained using BAA are presented for all systems.

Chapter V presents an efficient methodology to capture the nonlinear responses of combustor systems with pre-stress and friction. Instead of using direct numerical integration with full-order models, one can use the proposed ROMs to investigate the nonlinear dynamics of systems with Coulomb friction. Combustor systems experience wear at the interface between components due to flow-induced vibrations. In particular, wear has been observed at the interface between the transition piece and the hula seal, and at the interface between the hula seal and the liner. These interfaces are pre-stressed, and their vibratory response has a softening nonlinearity caused by Coulomb friction combined with micro-slip. In addition, the contact between the hula seal and the transition piece is that between a convex surface and a concave surface. Hence, geometric nonlinearity of the contact stiffness in the normal direction is present also. These phenomena are hard to capture by full order finite element approaches because they require time marching or harmonic balancing of very large models. To address this issue, we develop ROMs which are specifically designed to capture Coulomb friction (combined with micro-slip and macro-slip).

To demonstrate the proposed approach, a simplified hula seal is placed between two very rigid plates (which relate to the transition piece and the liner). Contact elements are used to model the interface between the plates and the hula seal. Transient dynamic analysis (TDA) in ANSYS is applied to the full-order model. The model is shown to exhibit softening nonlinearity and micro-slip at all levels of pre-stress. To show that ROMs for this system are possible, we use proper orthogonal decomposition to show that the dynamics is dominated by a low number of spatial coherences. For a variety of frequency ranges and pre-stress levels, we show that a single such coherence is dominant. Next, low order models are proposed and their parameters are identified. A systematic method to identify these parameters is developed. Particular attention is paid to the amount of calculations needed for obtaining these parameters. The ROMs are validated by comparing their predictions with results from TDA for the full-order model. It is shown that these ROMs can accurately predict the nonlinear response of the system with considerable savings in computational costs.

Finally in Chapter VI, conclusions are addressed and the contributions of this dissertation are summarized. Ideas for future work are discussed also.

CHAPTER II

Analyzing Mistuned Multi-Stage Turbomachinery Rotors with Aerodynamic Effects

2.1 Introduction

Turbomachinery modeling and analysis is an active area of research. A comprehensive review of research in this field was conducted by [17]. The initial modeling approach for these systems used simple lumped parameter models that usually contained one or two degrees of freedom per sector of a single-stage rotor [19, 20, 23–25]. These models were useful in gaining an understanding of the qualitative properties of bladed disks such as mistuning. Mistuning is small blade-to-blade differences in a bladed disk, which are inherent due to manufacturing processes and can be further exacerbated from operational wear. Mistuning is important in bladed disks because it breaks the designed cyclic symmetry of the system, which can lead to a localization of the vibration energy to a few sectors of the bladed disk in the operating frequency range. Due to the innate randomness of mistuning it must be studied in a statistical manner using many different mistuning realizations for a given design. The simple lumped parameter models were well suited for statistical study due to their low dimensionality; however, analyses of these systems do not provide accurate quantitative results for realistic industrial bladed disks.

High dimensional finite element models (FEMs) of bladed disks were developed to

obtain accurate quantitative results for these systems. Although running simulations on some of these FEMs is possible, performing a statistical analysis on a realistic model of an industrial bladed disk, to understand for example the effect of mistuning on a particular bladed disk design, would have a prohibitive computational expense. To overcome this high computational cost, reduced order models (ROMs) based on component mode synthesis [51, 56] (CMS) were developed. Eventually powerful ROMs were created that were of the order of the number of sectors in a bladed disk yet very accurate over a specified frequency range. [57] introduced the first of these powerful ROMs called the subset of nominal modes method. The key idea behind this approach is that for small mistuning the tuned system modes make an excellent basis for the mistuned modes. Component mode mistuning [12] (CMM) is another powerful ROM for bladed disks and it uses the blade component modes in addition to the system normal modes. The mistuning is handled in a systematic manner using the blade alone frequencies and the cantilever blade modes.

Although much research has been conducted on single-stage models, in practical applications there are multiple stages in a turbomachinery rotor. [58] showed that important multi-stage effects occur in certain frequency ranges where the motion of the disk is dominant. Multi-stage lumped parameter models were used by [59] to gain a qualitative understanding of the dynamics of these systems, but were not useful in quantitatively analyzing realistic multi-stage systems. [60] developed a novel way to create ROMs of multi-stage turbomachinery FEMs by projecting the motion along the interfaces between stages along a common set of harmonic basis functions and then enforcing compatibility. Their method was combined with CMM [12] to create compact multi-stage turbomachinery ROMs with mistuning. Their method was further developed to show its applicability to mistuning identification and structural health monitoring [61, 62]. A similar approach to [60] was later developed by [63, 64], and used to perform forced response and modal analysis cal-

culations on multi-stage turbomachinery bladed disks. There has also been recent work on the effects of coupling flexible rotors and shafts [65–69]. Recently, a novel way to create and analyze robust multi-stage ROMs was introduced using only single sector models of the stages [1, 39]. These works also demonstrate the effects of cracks in multi-stage models [39] and introduce a new way to classify structural multi-stage modes [1].

A considerable amount of research has also been conducted on coupling the aerodynamics with the structural models. One area of particular importance is the instabilities that can occur due to the aerodynamics [70–74]. Just as in the structure only case, early aeroelastic models used simple lumped parameter models for the structure [2–5], which did not quantitatively capture the dynamics of industrial bladed disks. To obtain better quantitative results, structural ROMs were developed from FEMs of the structure, and cantilever blade modes were used in computing the aerodynamic forcing. To understand the aerodynamic coupling between blades and the mistuning effects, [6] used perturbation methods. Later, an iterative approach to determine the eigenvalues and eigenvectors of an aeroelastic system was proposed by [7]. A technique that uses the ROMs of a structural model developed by [8,9] combined with inviscid fluid dynamics models investigated flutter and the forced response of single-stage bladed disks [10, 11]. An iterative aeroelastic coupling method that models the aerodynamics by a quasi-three dimensional potential flow and the structure using CMM was developed by [13, 14].

In this work, the aerodynamics are coupled with structural *multi-stage* turbomachinery models for the first time. The aerodynamic models are developed using the method of [13, 14, 32], while the structural models are created using the method of [1] and [39], which only requires single sector models of each stage. A new generalized characterization of the multi-stage *aeroelastic* modes is also developed based on a method to characterize structural modes [1]. The methodology for constructing multi-stage ROMs with

aerodynamic effects and the classification of the *complex* modes are flexible and work for any frequency domain aerodynamic models such as linearized or harmonic balance methods [75–78]. Also, the novel formulation of the multi-stage ROMs with aerodynamic effects accounts for the shift in frequency due to mistuning when computing the complex aerodynamic matrix. Many numerical simulations are performed to demonstrate the effectiveness of the methodology for Monte Carlo simulations and explore the interactions of the aerodynamics, the mistuning, and the damping in multi-stage systems.

2.2 Methodology

In this section, a brief overview of the construction of multi-stage ROMs with aerodynamic effects is given. Also, an approach to handle the shift in frequency due to mistuning in aeroelastic systems is discussed. After that, a new classification scheme for multi-stage systems with complex modes is introduced.

2.2.1 Multi-Stage Reduced Order Models with Aerodynamic Effects

A general procedure for constructing multi-stage models and account for the aerodynamics in tuned and mistuned systems is presented using previously developed structural methods [1, 12, 39, 51, 60]. The aerodynamic model [13, 14, 32, 79] is separately applied to each single-stage. The approach developed in this work for constructing aeroelastic ROMs is general and can be applied with alternative techniques for obtaining the complex aerodynamic matrix such as those based on linearized or harmonic balance methods [75–78]. Also, a new metric to characterize the combined effects of the mistuning and the aerodynamics is introduced.

A key advantage of the multi-stage structural ROM is that it can be constructed using single-sector models of each stage. The single-sector modeling takes advantage of the inherent cyclic symmetry of each tuned stage. The first step in the modeling procedure

is to use CMS [51] to divide each single-stage sector model into active interface degrees of freedom (DOFs) and fixed interface normal modes. The interface DOFs correspond to the interstage boundary DOFs that are used later to couple all stages together. The normal modes are then used with CMM to efficiently account for mistuning in each stage [12]. Finally, the active DOFs along the interstage boundary are projected onto a set of harmonic basis functions and compatibility is enforced between stages. The result yields reduced order mass $\mathbf{M}^{\mathrm{ROM},m}$ and stiffness $\mathbf{K}^{\mathrm{ROM},m}$ matrices for the mistuned multi-stage system. These structural ROMs can be created quickly and efficiently for many mistuning patterns and levels.

The complex aerodynamic matrix can be computed in a variety of ways including new linearized and harmonic balance methods [75–78]. In this work, the method developed by [13, 14, 32] and [79] is used to compute the complex aerodynamic matrix of the system $\mathbf{K}^{a}(\omega)$. This matrix is calculated in the space of generalized/reduced coordinates $\mathbf{q}$ which represent complex amplitudes of multi-stage modes without mistuning. The method has been validated by comparing its results with that of other unsteady codes and experimental results [80–82] for (single-stage) cascade flows. The method uses the full potential equation in a quasi-three dimensional model of a cascade discretized by a Galerkin formulation [83]. The flow is thus considered inviscid, irrotational and isentropic. In this work, the complex aerodynamic matrix is calculated separately for each stage using the same subspace of modes as that used in the structural model. The multi-stage complex aerodynamic matrix is then assembled using each of the single-stage complex aerodynamic matrices. The result is an aeroelastic system that is not aerodynamically coupled between stages (it is structurally coupled); therefore, there is no influence of the upstream aerodynamics on the downstream stages or vice versa. Note that the decoupling of the aerodynamics is due to the choice of aerodynamic solver used to extract the complex aero-

dynamic matrix and is not a limitation to the approach in general. Also, the aerodynamic effects (on each stage) have multi-stage consequences because of the structural coupling between stages. For example, if a multi-stage mode is exposed to an increased aerodynamic damping on stage 1, its amplitude is reduced in stage 2 also (not just in stage 1). This occurs even though the flow solver is not multi-stage. Thus, the aerodynamic effects have complex multi-stage consequences.

The forced response in the reduced coordinates for the mistuned system is given by

$$[-\omega^2\mathbf{M}^{\mathrm{ROM},m} + (1+j\gamma)\mathbf{K}^{\mathrm{ROM},m} + \mathbf{K}^a(\omega)]\mathbf{q} = \mathbf{F}(\omega), \tag{2.1}$$

where j is the imaginary unit, γ is the structural damping, $\mathbf{F}(\omega)$ is the forcing projected onto the reduced coordinates, and ω is the excitation frequency.

For forced response calculations, the frequency of the response is established by the forcing frequency ω. Thus, using Eq. (2.1) requires the calculation of $\mathbf{K}^a$ at that frequency. However, for free response calculations, the eigenvectors and eigenfrequencies are affected by mistuning. Accounting for the frequency dependence of $\mathbf{K}^a$ is the primary concern because $\mathbf{K}^a(\omega)$ is expressed in the space of multi-stage modes *without* mistuning. That is possible because, when mistuning is small, the mistuned aeroelastic modes can be represented by a linear combination of multi-stage modes without mistuning.

The shape of the vibratory motion of each multi-stage structural mode (without mistuning) is used to compute the corresponding column of $\mathbf{K}^a(\omega)$. The dependence of $\mathbf{K}^a(\omega)$ on the multi-stage mode shapes (without mistuning) is very strong because these mode shapes have different interblade phase angles, and the aerodynamics is strongly dependent on these angles. However, the dependence of $\mathbf{K}^a(\omega)$ on ω is quite smooth.

For free response calculations, the frequencies of the mistuned system are calculated iteratively. First, $\mathbf{K}^a$ is computed at the frequencies of the structure-only mistuned system.

The aeroelastic frequencies are then computed using Eq. (2.1) with $\mathbf{F}(\omega) = \mathbf{0}$. Next, $\mathbf{K}^a$ is calculated at those aeroelastic frequencies. The process is repeated until convergence of the aeroelastic frequencies is obtained. Typically, only $2-3$ iterations are needed [32]. This process requires repetitive calculations of $\mathbf{K}^a$ at various frequencies. Similarly, forced response predictions require computations at many different frequencies.

To alleviate the high computational cost of these calculations, the smooth dependence of $\mathbf{K}^a$ on ω can be exploited. Complex aerodynamic matrices $\mathbf{K}^a(\omega_s)$ are calculated for frequencies ω_s in increments of 1% to $\pm 5\%$ of the structure-only natural frequencies (i.e., $s = 1, \ldots, 11$). These matrices are then used to evaluate $\mathbf{K}^a(\omega)$ by interpolations based on ω. Specifically, the columns of $\mathbf{K}^a(\omega)$ are estimated by linearly interpolating between the columns of $\mathbf{K}^a(\omega_s)$ matrices based on ω. For example, consider the case where the mistuning has increased the j^{th} frequency ω of the system by 4.2%. This frequency value is between the values of 4% ($s = 10$) and 5% ($s = 11$). The j^{th} column of the mistuned complex aerodynamic matrix $\mathbf{K}^a_j(\omega)$ is approximated by linear interpolation,

$$\mathbf{K}^a_j(\omega) = 0.8 * \mathbf{K}^a_j(\omega_{10}) + 0.2 * \mathbf{K}^a_j(\omega_{11}). \tag{2.2}$$

This procedure is carried out for each column of the complex aerodynamic matrix for the mistuned system.

2.2.2 Generalized Classification of Complex Multi-Stage Mode

In this section, a new generalized classification scheme is developed for multi-stage systems with *complex* modes. This scheme generalizes the classification method developed by [1] that was designed to show the effects of the inter-stage coupling and mistuning on structure-only models of multi-stage systems. The generalized classification is based on two principles, namely the energy distribution and the modal alignment. The strain

energy E_{ij}^a in the i^{th} aeroelastic mode of the j^{th} stage is given by

$$E_{ij}^a = \text{real}(\phi_{ij}^a)^{\text{T}} \mathbf{K}_j^{\text{ROM},t} \text{real}(\phi_{ij}^a), \tag{2.3}$$

where $\mathbf{K}_j^{\text{ROM},t}$ is the structure only stiffness of the j^{th} stage in the reduced coordinates, and ϕ_{ij}^a is the portion of the aeroelastic mode that corresponds to the j^{th} stage. Only the real part of the aeroelastic mode is used because for the strain energy only the energy from the physical displacement of the structure is of interest. Similarly, only the motion of the structure is of concern for the energy in the stages, so the aeroelastic stiffness matrix is not included in the strain energy calculation. Note that since these calculations are done in the reduced order space, they can be done very efficiently. The strain energy ratio can be calculated for the i^{th} mode of stage 1 of a two stage aeroelastic system as

$$ER_{i1}^a = \frac{E_{i1}^a}{E_{i1}^a + E_{i2}^a}, \tag{2.4}$$

and for stage 2 as

$$ER_{i2}^a = \frac{E_{i2}^a}{E_{i1}^a + E_{i2}^a}. \tag{2.5}$$

The energy ratios ER_{i1}^a and ER_{i2}^a indicate the distribution of the strain energy of each aeroelastic mode in each stage.

The modal alignment criterion for the classification of the aeroelastic modes is different from the classification of structure only modes due to the additional imaginary component of the aeroelastic modes. A similar method to the modal assurance criterion (MAC) is once again used. The MAC number is a quantitative measure of the alignment of two modes, where the MAC is one if the modes are parallel, and zero if the modes are orthogonal. Complex aeroelastic modes can be separated into their real and imaginary parts, thus forming a plane in the N_j dimensional space, where N_j is the size of the reduced order model of the j^{th} stage. A complex MAC number MAC^c can be defined from the

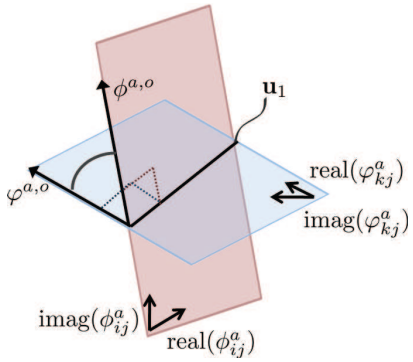

Figure 2.1: Schematic of the intersection of two planes in an N_j dimensional space.

alignment of these planes. The plane defined by the complex mode ϕ^a_{ij} can be defined as $\mathbf{\Phi}^{a,m}_{ij} = [\text{real}(\phi^a_{ij})\ \text{imag}(\phi^a_{ij})]$. The alignment of this plane must be compared against the complex modes φ^a_{kj}, which are the single-stage aeroelastic modes of the j^{th} stage, where $k \in n_j$ and n_j is the set of single j^{th} stage modes that are within a particular frequency range. The plane formed by φ^a_{kj} can be similarly defined as $\mathbf{\Phi}^{a,s}_{kj} = [\text{real}(\varphi^a_{kj})\ \text{imag}(\varphi^a_{kj})]$. The frequency range when single-stage aeroelastic modes will be checked against the multi-stage mode is given by

$$\varepsilon \geq \frac{\mid \omega_i - \omega_{kj} \mid}{\mid \omega_i \mid}, \tag{2.6}$$

where ω_i is the i^{th} multi-stage frequency, ω_{kj} is the k^{th} single-stage frequency of the j^{th} stage, and ε is the tolerance, which in this work was set to 10%.

To determine the angle between the planes defined by two complex aeroelastic modes in an N_j dimensional space one can take a singular value decomposition of the composite system $\mathbf{\Phi}^{a,c}_{kij} = [\mathbf{\Phi}^{a,m}_{ij}\ \mathbf{\Phi}^{a,s}_{kj}]$ to obtain

$$\mathbf{\Phi}^{a,c}_{kij} = [\mathbf{u}_1\ \mathbf{u}_2\ \mathbf{u}_3\ \mathbf{u}_4]\text{diag}(\sigma_1, \sigma_2, \sigma_3, \sigma_4)\mathbf{V}^{\text{T}}, \tag{2.7}$$

where σ_p are positive numbers called singular values, $\mathbf{u}_p$ are $N_j \times 1$ orthonormal left singular vectors, and $\mathbf{V}$ is a 4×4 matrix which contains the right singular vectors. The

singular values are ordered from highest to lowest and can be thought of as the level of contribution of the left singular vectors to the range space of $\mathbf{\Phi}^{a,c}_{kij}$. If $\sigma_4 > 0$, then the two planes do not intersect in the N_j dimensional space, and $\mathrm{MAC}^c_{ij} = 0$. If $\sigma_4 = 0$ and $\sigma_3 = 0$, then the subspace inhabited by the two planes is two dimensional, which means the planes inhabit the same subspace and $\mathrm{MAC}^c_{ij} = 1$. If $\sigma_4 = 0$ and $\sigma_3 > 0$, then the planes intersect but do not overlap, and the line of intersection is the dominant portion of the range space, which is given by $\mathbf{u}_1$. To quantitatively determine the alignment of these planes one must first find a line on each plane that is orthogonal to $\mathbf{u}_1$. Then, by finding the alignment of these two vectors using a MAC calculation one also determines the alignment of the planes. Using the Gram-Schmidt process one can identify a vector $\varphi^{a,o}_{kj}$ that is orthogonal to $\mathbf{u}_1$ within the space spanned by $\mathbf{\Phi}^{a,s}_{kj}$ as

$$\varphi^{a,o}_{kj} = \mathrm{real}(\varphi^a_{kj}) - (\mathbf{u}_1^{\mathrm{T}}\mathrm{real}(\varphi^a_{kj}))\mathbf{u}_1. \tag{2.8}$$

Similarly, one can find a vector $\phi^{a,o}_{ij}$ that is orthogonal to $\mathbf{u}_1$ within the space spanned by $\mathbf{\Phi}^{a,m}_{ij}$ as

$$\phi^{a,o}_{ij} = \mathrm{real}(\phi^a_{ij}) - (\mathbf{u}_1^{\mathrm{T}}\mathrm{real}(\phi^a_{ij}))\mathbf{u}_1. \tag{2.9}$$

The physical idea behind this approach is shown in Fig. 2.1 for the case where there is an intersection of the two planes in the N_j dimensional space. The MAC number can then be computed for these two vectors as

$$\mathrm{MAC}^c_{ij} = \max_{k \in n_j} \sqrt{\frac{((\varphi^{a,o}_{kj})^{\mathrm{T}}\phi^{a,o}_{ij})^2}{\| \varphi^{a,o}_{kj} \| \| \phi^{a,o}_{ij} \|}}. \tag{2.10}$$

The multi-stage complex modes can now be classified using Eqs. 2.4, 2.5 and 2.10. First, the modes can be classified by the energy distribution to determine whether the energy is isolated to a single-stage or whether it is split amongst the stages. Next, the modes are classified on their alignment with single-stage modes. A summary of the classification types of multi-stage *complex* modes for a two stage system are given in Tab. 2.1.

Mode Classification	Energy Distribution	Modal Alignment	Symbol
Stage 1 - single-stage mode ($S1$)	$ER_1^a > 0.9$	$MAC_1^c > 0.9$	△
Stage 1 - multi-stage mode (M_{S1})	$ER_1^a > 0.9$	$MAC_1^c < 0.9$	▲
Stage 2 - single-stage mode ($S2$)	$ER_2^a > 0.9$	$MAC_2^c > 0.9$	○
Stage 2 - multi-stage mode (M_{S2})	$ER_2^a > 0.9$	$MAC_2^c < 0.9$	●
Multi-stage - double single-stage mode ($M_{S1,S2}$)	$ER_1^a < 0.9$ AND $ER_2^a < 0.9$	$MAC_1^c > 0.9$ AND $MAC_2^c > 0.9$	□
Multi-stage mode ($M_{1,2}$)	$ER_1^a < 0.9$ AND $ER_2^a < 0.9$	$MAC_1^c < 0.9$ OR $MAC_2^c < 0.9$	■

Table 2.1: Classification of six types of aeroelastic modes using the energy distribution and the modal alignment criterion.

Figure 2.2: Multi-stage turbomachinery rotor.

2.3 Results

The system analyzed in this section is shown in Fig. 2.2. This system has 25 blades in the first stage and 23 blades in the second stage. Many multi-stage ROMs with aerodynamic effects were created from this system using a variety of mistuning levels and patterns by following the procedure highlighted in Sec. 2.2.1. The aeroelastic ROMs have 592 DOFs, which is about 0.5% of the original FEM size. The structural portion of the ROMs were developed from single sector models of each stage of the system. The stages were connected by projecting the motion along the interstage boundary onto 23 harmonic basis functions. The construction of the full multi-stage FEM shown in Fig. 2.2 was done

for validation of the structural ROMs, which has been presented in the literature [39]. The complex aerodynamic matrix was calculated using a flow solver for inviscid, irrotational, isentropic flow [13, 14, 32, 79, 82]. The validation of the aerodynamic code has been presented in the literature [13, 14, 32, 79]. The reduced frequency was approximately 6.15 and 7.65 near the hub for the frequency range of the first mode family of the first and second stage, respectively. The reduced frequency is based on the half chord and inlet velocity near the hub. The upstream far-field Mach number near the hub is 0.25. These flow conditions are below the flutter speed.

Many structural ROMs were developed at different mistuning levels and for different randomly chosen mistuning patterns. A complex aerodynamic matrix $\mathbf{K}^a$ was calculated at each eigenfrequency of each realization of the system by using a linear interpolation based on the $\mathbf{K}^a(\omega_s)$ matrices as described in Sec. 2.2.1. The ROMs developed were valid for the frequency range $0 - 20$ kHz; however the results in this work are focused on the narrower range $0 - 7$ kHz. Since, the flow conditions are below the flutter speed, the analyses focus on the forced response of the fluid-structural system rather than on self-excited vibrations (flutter). The response corresponds to forcing due to interactions with other stages, the rotor, or other forces applied to the two stage system. In this context, the fluid-structure interaction adds mass, stiffness, and damping effects. Thus, the fluid-structure interaction changes the forced response, but it is not the cause of the dynamics or of any instability such as flutter.

The first set of multi-stage results are presented in Fig. 2.3. Fig. 2.3(a) is the classification of the tuned aeroelastic multi-stage modes using the classification criteria presented in Tab. 2.1. The *x*-axis is the eigenvalue index, while the *y*-axis is the real part of the multi-stage frequency. For comparison, the classification of the tuned multi-stage modes (without aerodynamic effects) [1] is presented in Fig. 2.3(b). The influence of each stage

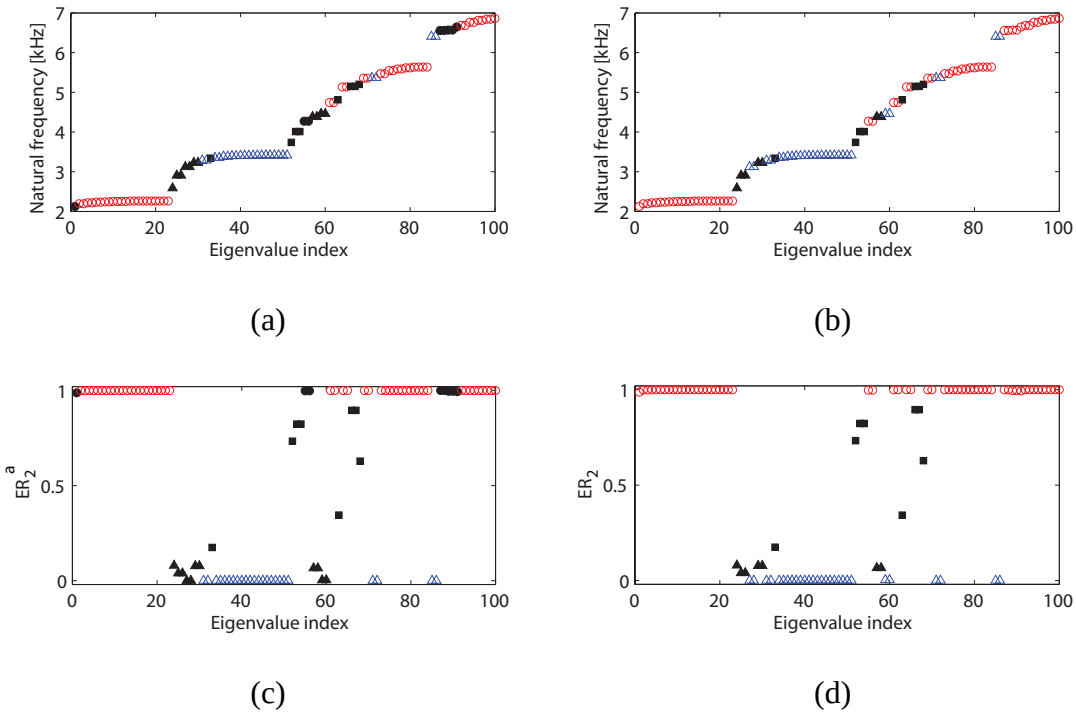

Figure 2.3: Frequencies and classification of the tuned multi-stage system (a) with aerodynamics effects and (b) without aerodynamic effects [1]. Energy distribution for the tuned multi-stage modes (c) with aerodynamics effects and (d) without aerodynamic effects [1].

is indicated by the shape of the symbol in the plots. These symbols are explained in Tab. 2.1 (i.e., the triangles correspond to stage 1 modes, the circles to stage 2 modes, and the squares to multi-stage modes). There is an added complexity when modeling the aerodynamic effects which results in more multi-stage M_{S1} and M_{S2} modes occurring in the multi-stage frequency ranges (near 3 kHz, 4.5 kHz and 6.5 kHz). The energy distribution for the system with aerodynamics is shown in Fig. 2.3(c) and for the system without aerodynamic effects [1] in Fig. 2.3(d). These plots show that for the *tuned* case the energy distribution between stages does not change due to the aerodynamic effects. However, the complex multi-stage modes are less likely to align with their single-stage counterparts. This suggests the need for multi-stage analysis which accounts for aerodynamic effects

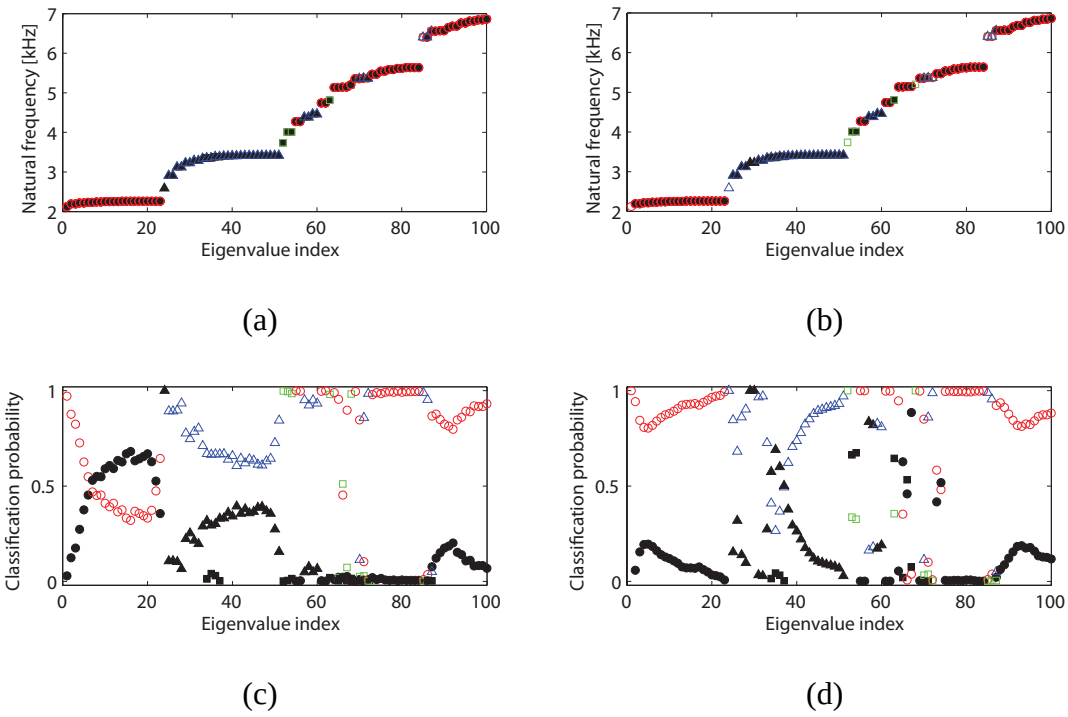

Figure 2.4: Frequencies and classification of the mistuned multi-stage system (a) with aerodynamics effects and (b) without aerodynamic effects [1]. Probability of classification for the mistuned multi-stage modes (c) with aerodynamics effects and (d) without aerodynamic effects [1].

in tuned systems over all frequency ranges, as opposed to the narrow frequency ranges $2 - 2.4$ kHz and $6.5 - 7$ kHz where a single-stage analysis would be valid for the tuned multi-stage system without aerodynamics.

Next, the effect of mistuning on the classification of aeroelastic multi-stage modes were studied using $1,000$ different mistuning patterns with a standard deviation of the mistuning of 5%. The results are presented in Fig. 2.4, where the layout of Fig. 2.4(a) and Fig. 2.4(b) are the same as Fig. 2.3(a). Since many different mistuning patterns are simultaneously being classified, multiple classification symbols can be plotted at each index. Fig. 2.4(a) corresponds to the mistuned systems with aerodynamic effects, while Fig. 2.4(b) corresponds to the mistuned systems without aerodynamic effects [1]. To gain a

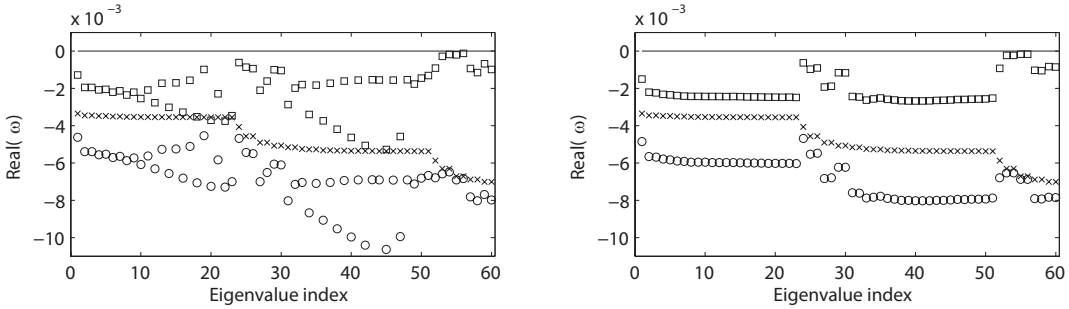

(a) (b)

Figure 2.5: Damping in the (a) tuned and (b) mistuned multi-stage systems for the structure only [−] , aeroelastic system [□], structure with structural damping [x], and aeroelastic system with structural damping [○].

clearer idea of the likelihood of a particular mode at a given index occuring, the probability of each classification of the aeroelastic system is shown in Fig. 2.4(c), and the probability of classification of each mode for the structure only system [1] is given in Fig. 2.4(d). Note that there is not a large difference between Fig. 2.4(a) and Fig. 2.4(b) or Fig. 2.3(a) and Fig. 2.3(b). The physical reason for this is the fact that the aerodynamic matrix has a much larger influence on damping than on stiffness. The aerodynamic stiffness contribution is very small compared to the structural stiffness. However, the damping contribution of the aerodynamic matrix is comparable with the structural damping. Figures 2.4(a), 2.4(b), 2.3(a) and 2.3(b) are based on the mode shapes of the multi-stage system. Note that, the flow influences these mode shapes and their damping. When mistuning is present, it is clear from Fig. 2.4(c) and Fig. 2.4(d) that the probability distribution of the mode types does change considerably due to the aerodynamic effects. Thus, in both the structural and aeroelastic cases, multi-stage analysis is needed due to the very complex interactions and possibilities that exist when considering mistuning in multi-stage systems.

The main impact of considering the aerodynamics with the structure is how the damp-

ing is affected. To understand how the damping changes with the inclusion of the aerodynamics, the imaginary part of the multi-stage natural frequency is investigated for several cases. The results for the tuned case are summarized in Fig. 2.5(a), while the results for the mistuned case are summarized in Fig. 2.5(b). For each eigenvalue index four different values are reported corresponding to four distinct cases. The first case is the structural system with no added structural damping and this corresponds to the case with the least damping. The second case is the aeroelastic system with no added structural damping. The next case is the structural system with structural damping of the form $j\gamma\mathbf{K}^{\mathrm{ROM},m}$ (where $\gamma = 0.0005$) included. The final case is the aeroelastic system with structural damping included and that has the most damping. The overall impact of the aeroelastic damping will vary greatly depending on the relative size of the aeroelastic and structural damping. In this work the influence of the aeroelastic damping is very significant since it is of the same order as the structural damping. For the mistuned case, the average value of the imaginary part of the natural frequencies for the $1,000$ mistuning patterns are plotted in Fig. 2.5(b). The standard deviation tends to be very small ($< 3\%$) so standard deviation bars are not plotted to avoid making the figure difficult to read. In analyzing Fig. 2.5(b), one can note that the aeroelastic damping tends to equalize across mode families due to the mistuning. For example the flat region associated with indices $1 - 23$ correspond to the first mode family of the second stage. For (higher) indices $24 - 28$, there is a mix of multi-stage modes and stage 1 dominated modes. Next is the rest of the first family of stage 1 dominated modes (from eigenvalue indices 29-51). For the tuned case the aeroelastic damping is less uniform as is shown in Fig. 2.5(a).

To understand the effects of the aerodynamics on the system, forced response simulations were performed. The results are summarized in Figs. 2.6 and 2.7. A structural damping of $\gamma = 0.0005$ was used for all the forced response calculations. Forces were

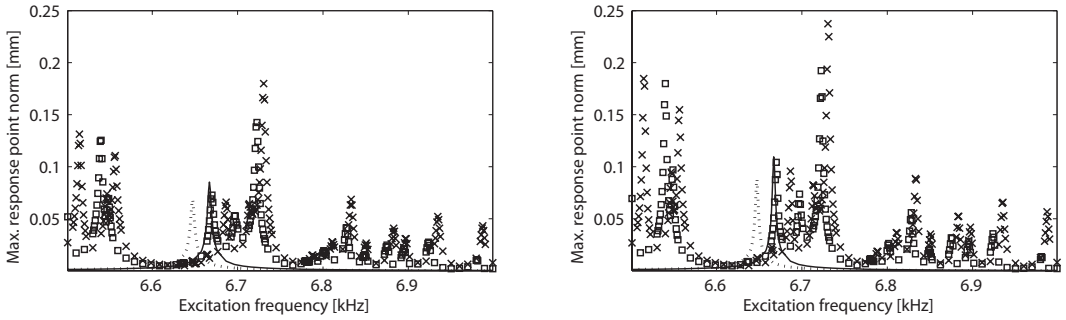

(a) (b)

Figure 2.6: Forced response of stage 2 for the system (a) with aerodynamics effects and (b) without aerodynamics effects for the tuned system using a single-stage analysis [−], mistuned system using a single-stage analysis [x], tuned system using a multi-stage analysis [. . .], and mistuned system using a multi-stage analysis [□].

applied at the tips of the blades on each stage with specified engine order excitations. The maximum of the response at the excited nodes of each stage was used as the maximum response for that stage. First, an engine order zero excitation was applied to each stage at 512 equally spaced frequencies from 6.5 kHz to 7.0 kHz. The results are summarized for the system with aerodynamic effects in Fig. 2.6(a) and without aerodynamic effects in Fig. 2.6(b) for stage 2 for four cases. The first case is the tuned response using a single-stage analysis. The second case is a sample mistuned response using a single-stage analysis. The third case is the tuned response using a multi-stage analysis. The final case is a sample mistuned response using a multi-stage analysis. The results for stage 1 are omitted for this analysis because the response is negligible for stage 1 in this frequency range. This is because the energy is concentrated in stage 2 over this frequency range, which can be seen by inspecting the types of modes in this frequency range using Figs. 2.3 and 2.4. The x-axis in each plot is the frequency of excitation, while the y-axis is the maximum response for stage 2. A key observation when comparing Fig. 2.6(a) with Fig. 2.6(b)

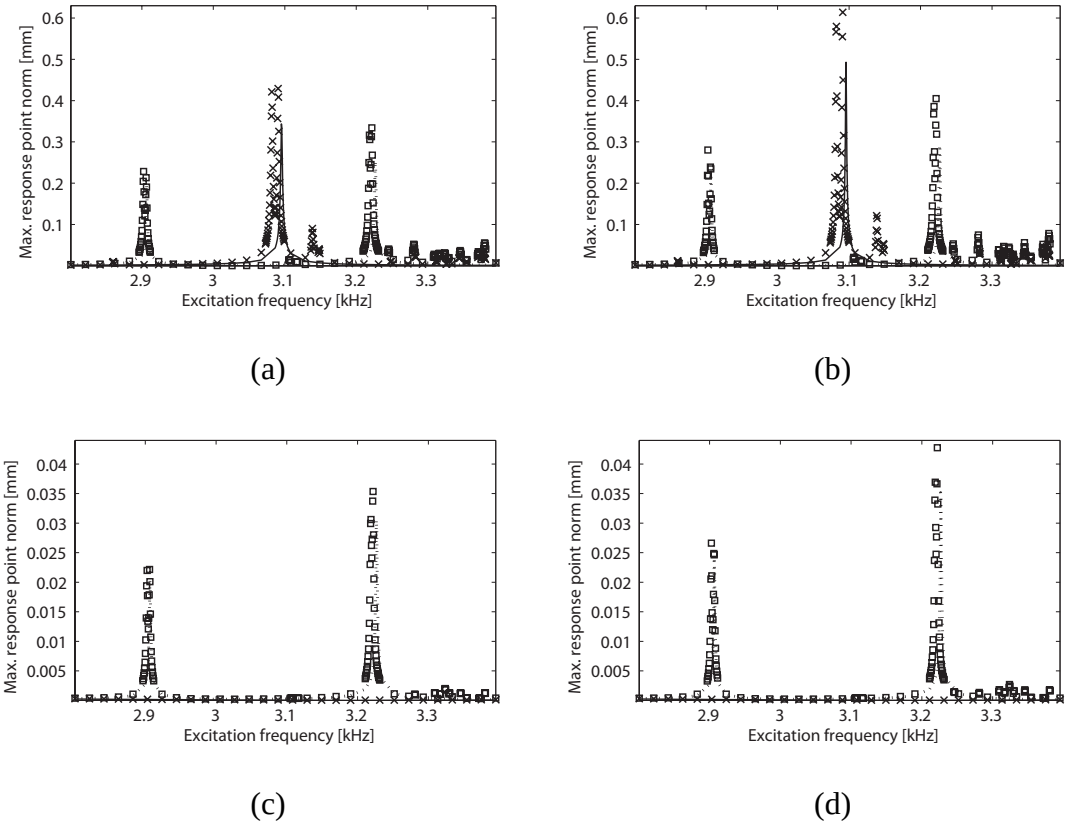

Figure 2.7: Forced response of stage 1 (a) with aerodynamics effects and (b) without aerodynamic effects, and of stage 2 (c) with aerodynamics effects and (d) without aerodynamic effects for the tuned system using a single-stage analysis [$-$], mistuned system using a single-stage analysis [x], tuned system using a multi-stage analysis [$\ldots$], and mistuned system using a multi-stage analysis [$\square$].

is that the responses in all cases tend to be approximately 20% lower for the aeroelastic system. The peaks at each frequency, however, do not scale by the exact same value. This is to be expected since the aeroelastic damping is not the same across all modes (as can be seen in Fig. 2.5). Fig. 2.6 highlights the need for a multi-stage analysis to be carried out irrespective if one is accounting for aerodyanmic effects (even when exploring a frequency range that is dominated by motion in a single-stage).

The results of an engine order one excitation applied to each stage at $1,024$ equally spaced frequencies from 2.8 kHz to 3.4 kHz is summarized in Fig. 2.7. The plots are

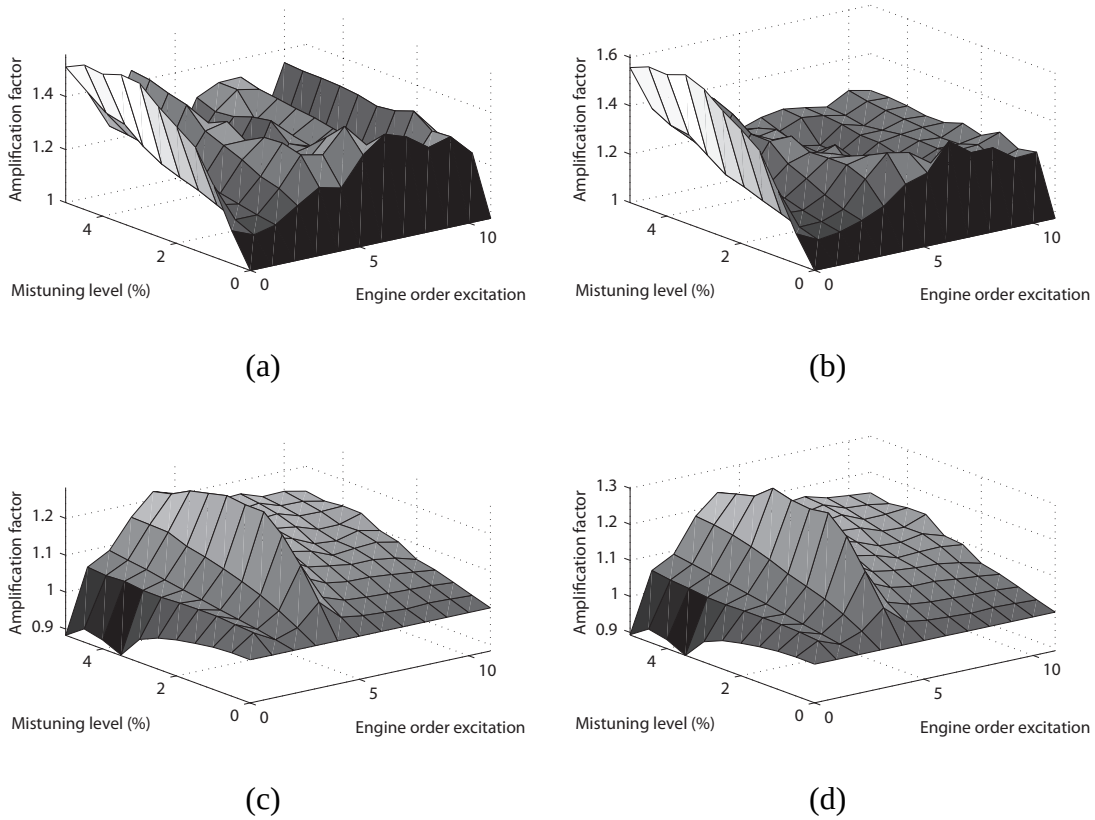

Figure 2.8: Force amplification factor versus mistuning level and engine order excitation for the multi-stage system for stage 1 (a) with aerodynamic effects and (b) without aerodynamic effects, and stage 2 (c) with aerodynamic effects and (d) without aerodynamic effects.

laid out in the same way as in Fig. 2.6 with the same four cases being considered. Stage 1 and stage 2 results are plotted for this case since this frequency range has modes with energy split between both stages making the response significant in both stages. These results highlight similar observations from the previous forced response case. Namely, accounting for the aerodynamics introduces additional damping that reduces the response by approximately 20%. However, this level varies at different frequencies. Also, multi-stage modeling is once again important for accurate aeroelastic or purely structural analysis, and in this particular frequency range multi-stage effects are paramount.

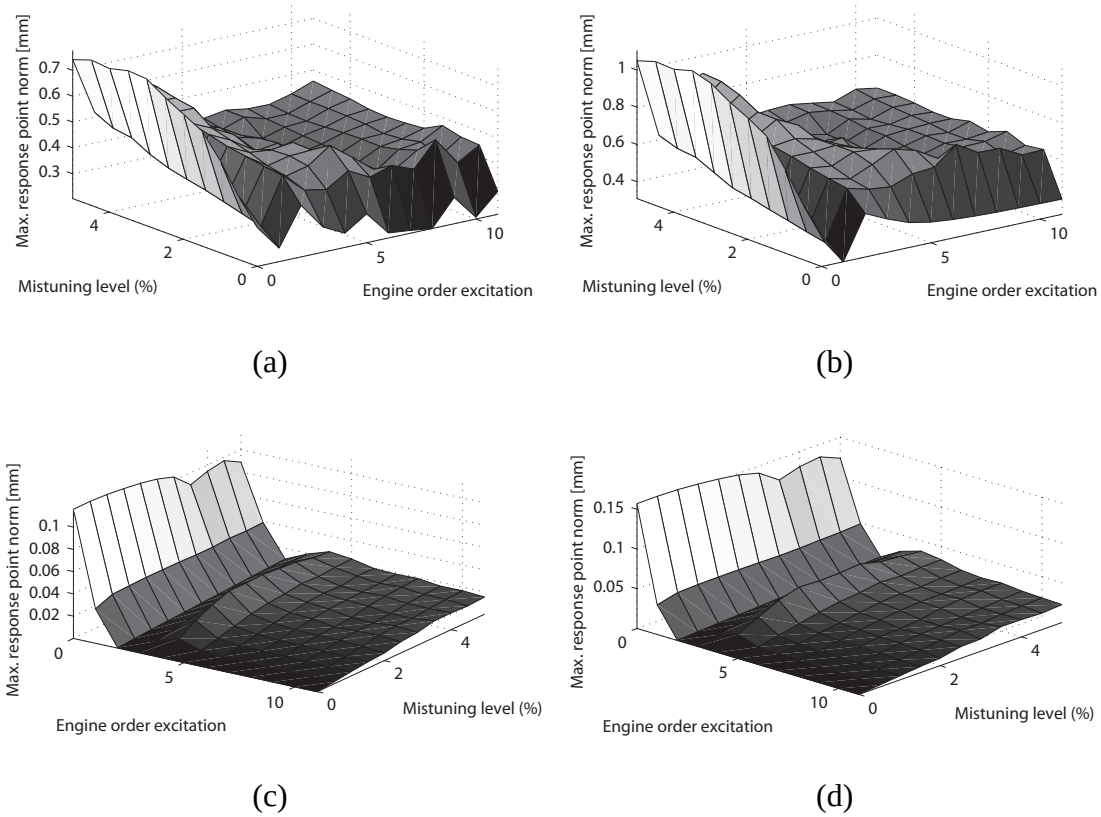

Figure 2.9: Maximum force response versus mistuning level and engine order excitation for the multi-stage system for stage 1 (a) with aerodynamic effects and (b) without aerodynamic effects, and stage 2 (c) with aerodynamic effects and (d) without aerodynamic effects.

To better understand the effects of mistuning on structural and aeroelastic systems, amplification factor plots for stage 1 and 2 were generated. The results are summarized in Fig. 2.8 and contain the 99^{th} percentile response of 100 mistuning patterns for engine order excitation 0 to 11 and mistuning levels from 0% to 5% over the frequency range $2.8 - 3.6$ kHz. One hundred separate forced response calculations were performed at each unique mistuning level and engine order excitation combination. To account for a low response of the tuned system of a stage at a particular engine order excitation of the multi-stage system, a modified amplification factor is used. This amplification factor for a system

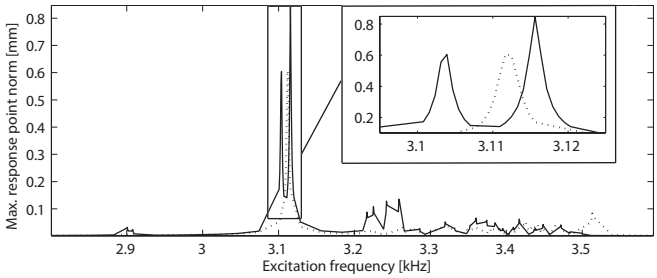

Figure 2.10: Maximum forced response of stage 1 for 100 mistuning realizations of the structural system $[-]$ and the aeroelastic system $[\ldots]$ for engine order 2 excitation.

with a given mistuning level and engine order excitation is defined as the maximum response of the mistuned systems plus the maximum tuned response across all engine order excitations divided by the tuned response (at the particular engine order excitation) plus the maximum tuned response across all engine order excitations. This definition avoids confusion which appear when the response is very low at particular engine order excitations. The corresponding maximum forced response for the structural and aeroelastic systems are shown in Fig. 2.9. The key physical insight that can be gained from Figs. 2.8 and 2.9 is that multi-stage effects affect the mistuned response, and this should be considered because it can lead to very different amplification factors compared to single-stage calculations.

An interesting point in both the structural and the aeroelastic systems is that for engine order 0 excitation in stage 2 the amplification factor is below one. This is due to multi-stage interactions where the mistuning effects are combined with the interstage coupling effects, and energy is transferred from stage 2 to stage 1. Also, the response for the aeroelastic system is lower than the structural system as expected due to the additional damping. Moreover, the amplification factor of the aeroelastic system is lower than that of

the structural system. This can be explained by the fact that mistuning tends to equalize damping across the modes, as was shown in Fig. 2.5(b), thus lowering the response of the mistuned systems. Additionally, when studying stage 1 it is clear that the topology of both the response and amplification factor plots are different for the structural and aeroelastic systems. This occurs because of the aeroelastic damping, which can cause systems with different mistuning patterns to have a larger response. To explore this, a forced response comparison is done at engine order excitation 2 with a 5% standard deviation of mistuning for the maximum response for both the aeroelastic and structural system. The results are plotted in Fig. 2.10. Note that a different mistuning pattern leads to the maximum response in the structural system versus the aeroelastic system.

2.4 Conclusions

A new approach to construct multi-stage reduced order models (ROMs) with aerodynamic effects was presented. The method can efficiently compute many realizations of the structural portion of the system for many different mistuning patterns. The method requires only single sector models of each stage, and uses cyclic symmetry analysis, component mode mistuning, and a projection of the interstage degrees of freedom onto a set of harmonic basis functions. The aerodynamics are then included in the model by computing the complex aerodynamic matrix for the system. In general this can be done with a variety of techniques. In this work, the complex aerodynamic matrices were calculated separately for each tuned stage using an inviscid, irrotational and isentropic flow solver based on the full potential equation. Only a tuned analysis of the flow is necessary because a new approximation of the complex aerodynamic matrices for mistuned systems was developed. The approximation accounts for the shift in structural frequencies due to mistuning. The proposed approach is general and can be used when other methods are employed to com-

pute the complex aerodynamic matrix. Also, a new classification method was developed for categorizing complex multi-stage modes. This classification method first distinguishes the energy distribution of the modes amongst stages, and then determines the alignment of the aeroelastic multi-stage modes with single-stage modes. Due to the fact that the aeroelastic modes are complex, they are separated into real and imaginary parts forming a plane in a higher dimensional subspace, and a new method is presented for determining the alignment of these planes in a higher dimensional space.

The modeling procedure was carried out for the tuned case and many mistuned realizations of a two stage bladed disk. The interactions of structural and aerodynamic damping, mistuning and multi-stage structural coupling were investigated. Several conclusions can be drawn from this work. First, the construction of multi-stage systems with aerodynamic effects is important for both tuned and mistuned systems to understand the dynamic response and characteristics of these systems. The aerodynamics can have a large impact on the damping of the multi-stage system, and mistuning tends to equalize the aerodynamic damping over the mode families. Due to the fact that the aerodynamic damping can be of the same order as the structural damping, it can have a significant impact on lowering the vibrational response of the system. Thus, classifications and forced responses of the system must be explored in a probablistic manner to understand the true impact of random mistuning on aeroelastic systems. Finally, it was shown that multi-stage modeling is critical for analysis of both purely structural and aeroelastic systems.

The analysis in this work is for a multi-stage structure with the loads from the aerodynamics computed at a stage level. The methodology presented can be used the same way when the unsteady flow field accounts for all aerodynamic multi-stage effects. Thus, accounting for the full multi-stage aerodynamics is a component of future work. The results presented take into account certain aspects of the aerodynamics (although the aero-

dynamics is not multi-stage). The results are useful because they are a step forward in increasing the accuracy of multi-stage structural analyses (which typically do not account for aeroelastic effects at all). Future work in this area includes developing a method for efficiently computing multi-stage complex aerodynamic matrices that couple the upstream and downstream stages, and experimental validation of the analysis.

CHAPTER III

Detection of Cracks in Mistuned Bladed Disks using Reduced Order Models and Vibration Data

3.1 Introduction

The vibration analysis of bladed disks in a turbine engine rotor can be conducted easily if it is assumed that all of their sectors are identical because cyclic symmetry can be employed. In reality, however, there are unavoidable small differences among the structural properties or geometric characteristics between individual sectors due to manufacturing tolerances, material deviations, and non-uniform operational wear. These small differences are commonly referred to as mistuning. Even though the mistuning level is typically small in terms of individual blade properties, this small mistuning can have a considerable impact on the forced response. Namely, mistuning can cause a localization of vibration to a few blades, which leads to a drastic increase in the response amplitude for those blades. A number of studies have been conducted to investigate the effects of mistuning on bladed disks [15–17]. Some of the early studies have been based on lumped parameter models [18–26]. In general, the effects of mistuning can be understood qualitatively by these simple models (in single stage systems) [27–29]. However, these models are only partially able to predict accurately the vibration characteristics of bladed disks [13, 14, 30–32], especially in multi-stage systems [1].

Vibration localization can be induced not only by mistuning but also by damages to the bladed disk, such as cracks. Damages can result during operation, from material defects, and from fatigue. Several investigators have tackled vibration localization due to cracks by assuming that the cracked blade is an Euler-Bernoulli beam or by using a lumped-mass beam model [33–38]. In those studies, the nonlinearity caused by the crack opening and closing was not considered. However, this piece-wise linear behavior may change the dynamic response of the cracked blades significantly [39–41]. Recently, Saito *et al.* [45, 46] presented an efficient reduced-order modeling method for mistuned bladed disks with a cracked blade. They used a hybrid component mode synthesis (CMS) method to obtain reduced order models (ROMs). To calculate the nonlinear forced responses, they used a hybrid frequency/time domain (HFT) method based on the harmonic balanced method [47] and fast Fourier transforms. A modal analysis of the full mistuned bladed disk with a cracked blade was employed to obtain ROMs. Therefore, the computational costs are significant especially when many mistuning patterns have to be considered. This is important when investigating real mistuned bladed disks because mistuning patterns are usually random. For efficient projection of blade mistuning, Lim *et al.* [12] developed the component mode mistuning (CMM) method to generate ROMs for mistuned bladed disks. In CMM, the mistuned bladed disk is partitioned into a tuned bladed disk component and a virtual blade mistuning component. The mistuning component is defined by the differences between the mistuned and the tuned blade mass and stiffness matrices. For the case of small stiffness-only blade-to-blade variations, the mistuning becomes an eigenvalue mistuning, and can be defined as the difference between the eigenvalues of the mistuned cantilevered blades and the tuned cantilevered blade.

In this paper, a novel nonlinear vibration analysis method that predicts the forced response of mistuned bladed disks with a cracked blade is presented. In addition, the mode

localizations due to mistuning and cracks are examined, and a method to detect the presence of cracks is presented. In this novel method, the mistuned bladed disk with a cracked blade is partitioned into a tuned bladed disk with a cracked blade and blade mistuning on the uncracked blades. A hybrid CMS is used to generate ROMs of tuned bladed disks with a cracked blade. The interface degrees of freedom (DOFs) on the crack surfaces are retained as active DOFs for evaluation of the nonlinear boundary conditions, while the other DOFs are condensed using modal analysis. Also, CMM is employed to project blade mistuning on the modes of the tuned system with a cracked blade. Nonlinear steady-state response analyses are performed using a HFT method.

This paper is organized as follows. First, the mathematical formulation of the reduced-order modeling approach is presented. Then, the formulation is applied to the vibration analysis of a mistuned bladed disk with a cracked blade. The results are validated by comparisons with a previous study by Saito *et al.* [45]. In addition, the distinct mode localizations across mode families due to mistuning and cracks are discussed. Finally, a novel method to distinguish cracks in mistuned bladed disks is presented.

3.2 Methodology

In this section, the equations of motion for a mistuned bladed disk with a cracked blade are presented first. Next, the reduced order modeling procedure is explained. Then, a mode localization parameter is introduced. Finally, the residual of the normal modes of a mistuned bladed disk with a cracked blade is introduced.

3.2.1 Equations of Motion

The mistuned bladed disk with a cracked blade is modeled as a linear elastic structure, and the related governing equation is spatially discretized by the finite element method.

The discretized form of the governing equation can be written as

$$\mathbf{M}\ddot{\mathbf{u}}(t) + \mathbf{C}\dot{\mathbf{u}}(t) + \mathbf{K}\mathbf{u}(t) = \mathbf{b}(t) + \mathbf{f}(\mathbf{u}), \tag{3.1}$$

where m is the number of DOFs and $\mathbf{u} \in \mathbb{R}^m$ is the vector of nodal displacements of a full order finite element model of the entire mistuned bladed disk with a cracked blade. $\mathbf{M}$, $\mathbf{C}$, $\mathbf{K} \in \mathbb{R}^{m \times m}$ are mass, damping, and stiffness matrices, $\mathbf{b} \in \mathbb{R}^m$ is the external force vector, and $\mathbf{f}(\mathbf{u}) \in \mathbb{R}^m$ is the nonlinear force vector caused by the intermittent contact at the crack surfaces. The external force acting on each blade is assumed to be a traveling wave excitation with a frequency ω related using the engine order excitation C to the rotational speed of the bladed disk. The force $\mathbf{b}_i(t)$ acting on blade i is expressed as

$$\mathbf{b}_i(t) = \boldsymbol{\beta} \cos(\omega t - \phi_i), \quad i = 1, ..., N, \tag{3.2}$$

where i is the blade number, N is the number of blades, and $\boldsymbol{\beta}$ is the forcing amplitude vector (which is the same for all blades). Vector $\boldsymbol{\beta}$ has a size equal to the number of forced DOFs on a blade. Thus, vector $\mathbf{b}(t)$ contains all vectors $\mathbf{b}_i(t)$ and also zeroes (corresponding to the DOFs which are not forced). The angle ϕ_i is the interblade phase angle, defined as $\phi_i = (i-1)2\pi C/N$.

3.2.2 Reduced-Order Modeling

Typically, finite element models (FEMs) of complex structures such as bladed disk assemblies have many DOFs. In this paper, such an FEM is employed as the starting point in constructing ROMs for a mistuned bladed disk with a cracked blade. The model is partitioned into a tuned bladed disk component with a cracked blade and a blade mistuning component. To combine the tuned system and mistuning components, a hybrid CMS is employed. The tuned system is treated as a free-interface component, whereas the mistuning component is treated as a fixed-interface component. For the tuned system

component, free-interface normal modes, attachment modes, and constraint modes are employed. Because the tuned system component is a free-interface component, the normal modes are simply the modes of the tuned bladed disk with a cracked blade. The attachment modes are obtained by applying a unit force to each interface DOF successively. The constraint modes are obtained by enforcing a unit displacement at each interface DOF on the crack surfaces.

The constraint modes are needed to account for the displacement due to intermittent contacts between the crack surfaces. Since cracks are localized on (the blades of) some sectors, one can assume that the other sectors (which have uncracked blades) are not affected by the enforced unit displacements at the interface DOFs on the crack surfaces. Therefore, the partitions in the constraint modes for the uncracked blades and disk are assumed to be zero.

Let the vector of nodal displacements $\mathbf{u}^S$ of the tuned bladed disk with a cracked blade be partitioned into cracked blade interior DOFs (except DOFs on the crack surfaces) $\mathbf{u}_i^S$, uncracked blade DOFs $\mathbf{u}_b^S$, disk DOFs $\mathbf{u}_d^S$, and crack surface DOFs $\mathbf{u}_c^S$. To represent $\mathbf{u}^S$, a truncated set of normal modes $\mathbf{\Phi}^S$, a complete set of attachment modes $\mathbf{\Psi}^S$, and constraint modes $\mathbf{\Psi}^C$ are employed. In the following, the matrices $\mathbf{\Phi}^S$, $\mathbf{\Psi}^S$, and $\mathbf{\Psi}^C$ are each partitioned into four components: (1) one component contains all the cracked blade interior DOFs (indicated by subscript i), (2) one component contains all the uncracked blade DOFs (indicated by subscript b), (3) one component contains all the disk DOFs (indicated by subscript d), (4) and one component contains all the DOFs on the crack surfaces (indicated by subscript c). By denoting the coordinates of the truncated set of

normal modes and attachment modes as $\mathbf{p}_\phi^S$ and $\mathbf{p}_\psi^S$ respectively, $\mathbf{u}^S$ can be represented as

$$\mathbf{u}^S = \begin{bmatrix} \mathbf{u}_i^S \\ \mathbf{u}_b^S \\ \mathbf{u}_d^S \\ \mathbf{u}_c^S \end{bmatrix} = \begin{bmatrix} \hat{\mathbf{\Phi}}^S & \hat{\mathbf{\Psi}}^S & \mathbf{\Psi}^C \end{bmatrix} \begin{bmatrix} \mathbf{p}_\phi^S \\ \mathbf{p}_\psi^S \\ \mathbf{u}_c^S \end{bmatrix}, \tag{3.3}$$

$$\hat{\mathbf{\Phi}}^S = \begin{bmatrix} \hat{\mathbf{\Phi}}_i^S \\ \mathbf{\Phi}_b^S \\ \mathbf{\Phi}_d^S \\ \mathbf{0} \end{bmatrix}, \hat{\mathbf{\Psi}}^S = \begin{bmatrix} \hat{\mathbf{\Psi}}_i^S \\ \mathbf{\Psi}_b^S \\ \mathbf{\Psi}_d^S \\ \mathbf{0} \end{bmatrix}, \tag{3.4}$$

where $\hat{\mathbf{\Phi}}_i^S = \mathbf{\Phi}_i^S - \mathbf{\Psi}_i^C \mathbf{\Phi}_c^S$, and $\hat{\mathbf{\Psi}}_i^S = \mathbf{\Psi}_i^S - \mathbf{\Psi}_i^C \mathbf{\Psi}_c^S$. By using this projection, the reduced mass and stiffness matrices can be obtained as follows

$$\boldsymbol{\mu}^S = \begin{bmatrix} \hat{\mathbf{\Phi}}^{S^{\mathrm{T}}} \mathbf{M}^S \hat{\mathbf{\Phi}}^S & \hat{\mathbf{\Phi}}^{S^{\mathrm{T}}} \mathbf{M}^S \hat{\mathbf{\Psi}}^S & \hat{\mathbf{\Phi}}^{S^{\mathrm{T}}} \mathbf{M}^S \mathbf{\Psi}^C \\ \hat{\mathbf{\Psi}}^{S^{\mathrm{T}}} \mathbf{M}^S \hat{\mathbf{\Phi}}^S & \hat{\mathbf{\Psi}}^{S^{\mathrm{T}}} \mathbf{M}^S \hat{\mathbf{\Psi}}^S & \hat{\mathbf{\Psi}}^{S^{\mathrm{T}}} \mathbf{M}^S \mathbf{\Psi}^C \\ \mathbf{\Psi}^{C^{\mathrm{T}}} \mathbf{M}^S \hat{\mathbf{\Phi}}^S & \mathbf{\Psi}^{C^{\mathrm{T}}} \mathbf{M}^S \hat{\mathbf{\Psi}}^S & \mathbf{\Psi}^{C^{\mathrm{T}}} \mathbf{M}^S \mathbf{\Psi}^C \end{bmatrix}, \tag{3.5}$$

$$\boldsymbol{\kappa}^S = \begin{bmatrix} \hat{\mathbf{\Phi}}^{S^{\mathrm{T}}} \mathbf{K}^S \hat{\mathbf{\Phi}}^S & \hat{\mathbf{\Phi}}^{S^{\mathrm{T}}} \mathbf{K}^S \hat{\mathbf{\Psi}}^S & \hat{\mathbf{\Phi}}^{S^{\mathrm{T}}} \mathbf{K}^S \mathbf{\Psi}^C \\ \hat{\mathbf{\Psi}}^{S^{\mathrm{T}}} \mathbf{K}^S \hat{\mathbf{\Phi}}^S & \hat{\mathbf{\Psi}}^{S^{\mathrm{T}}} \mathbf{K}^S \hat{\mathbf{\Psi}}^S & \hat{\mathbf{\Psi}}^{S^{\mathrm{T}}} \mathbf{K}^S \mathbf{\Psi}^C \\ \mathbf{\Psi}^{C^{\mathrm{T}}} \mathbf{K}^S \hat{\mathbf{\Phi}}^S & \mathbf{\Psi}^{C^{\mathrm{T}}} \mathbf{K}^S \hat{\mathbf{\Psi}}^S & \mathbf{\Psi}^{C^{\mathrm{T}}} \mathbf{K}^S \mathbf{\Psi}^C \end{bmatrix}. \tag{3.6}$$

It should be noted that $\hat{\mathbf{\Phi}}^{S^{\mathrm{T}}} \mathbf{M}^S \hat{\mathbf{\Phi}}^S \neq \mathbf{I}$ and $\hat{\mathbf{\Phi}}^{S^{\mathrm{T}}} \mathbf{K}^S \hat{\mathbf{\Phi}}^S \neq \mathbf{\Lambda}^S$ due to the presence of the projection matrix modeling the crack surfaces $\mathbf{\Phi}_c^S$ into the projection matrix modeling the motion of the DOFs on the interior of the cracked blade $\hat{\mathbf{\Phi}}_i^S$.

The synthesis of the tuned system and mistuning components is achieved by satisfying displacement compatibility at the component interface, i.e., $\mathbf{u}_b^S = \mathbf{u}^\delta$, where δ denotes mistuning. One obtains

$$\mathbf{\Phi}_b^S \mathbf{p}_\phi^S + \mathbf{\Psi}_b^S \mathbf{p}_\psi^S = \mathbf{p}_\psi^\delta, \tag{3.7}$$

$$\mathbf{p}_{\psi}^{\delta} = \begin{bmatrix} \boldsymbol{\Phi}_b^S & \boldsymbol{\Psi}_b^S \end{bmatrix} \begin{bmatrix} \mathbf{p}_{\phi}^S \\ \mathbf{p}_{\psi}^S \end{bmatrix}. \tag{3.8}$$

Therefore, the reduced mass and stiffness matrices for the mistuning component can be written as

$$\begin{aligned} \boldsymbol{\mu}^{\delta} &= \begin{bmatrix} \boldsymbol{\Phi}_b^S & \boldsymbol{\Psi}_b^S \end{bmatrix}^{\mathrm{T}} \mathbf{M}^{\delta} \begin{bmatrix} \boldsymbol{\Phi}_b^S & \boldsymbol{\Psi}_b^S \end{bmatrix} \\ &= \begin{bmatrix} \boldsymbol{\Phi}_b^{S^{\mathrm{T}}} \mathbf{M}^{\delta} \boldsymbol{\Phi}_b^S & \boldsymbol{\Phi}_b^{S^{\mathrm{T}}} \mathbf{M}^{\delta} \boldsymbol{\Psi}_b^S \\ \boldsymbol{\Psi}_b^{S^{\mathrm{T}}} \mathbf{M}^{\delta} \boldsymbol{\Phi}_b^S & \boldsymbol{\Psi}_b^{S^{\mathrm{T}}} \mathbf{M}^{\delta} \boldsymbol{\Psi}_b^S \end{bmatrix}, \end{aligned} \tag{3.9}$$

$$\begin{aligned} \boldsymbol{\kappa}^{\delta} &= \begin{bmatrix} \boldsymbol{\Phi}_b^S & \boldsymbol{\Psi}_b^S \end{bmatrix}^{\mathrm{T}} \mathbf{K}^{\delta} \begin{bmatrix} \boldsymbol{\Phi}_b^S & \boldsymbol{\Psi}_b^S \end{bmatrix} \\ &= \begin{bmatrix} \boldsymbol{\Phi}_b^{S^{\mathrm{T}}} \mathbf{K}^{\delta} \boldsymbol{\Phi}_b^S & \boldsymbol{\Phi}_b^{S^{\mathrm{T}}} \mathbf{K}^{\delta} \boldsymbol{\Psi}_b^S \\ \boldsymbol{\Psi}_b^{S^{\mathrm{T}}} \mathbf{K}^{\delta} \boldsymbol{\Phi}_b^S & \boldsymbol{\Psi}_b^{S^{\mathrm{T}}} \mathbf{K}^{\delta} \boldsymbol{\Psi}_b^S \end{bmatrix}. \end{aligned} \tag{3.10}$$

Now, if small blade mistuning is considered, the attachment mode $\hat{\boldsymbol{\Psi}}^S$ can be ignored because, when a tuned bladed disk has normal modes closely spaced in a frequency range, a slightly mistuned bladed disk also features closely spaced modes in the same range. Moreover, the mistuned normal modes can be expressed using a subset of the tuned normal modes. This means that the tuned normal modes outside of the frequency range of interest (or any static modes) can be ignored in modeling a mistuned system with small mistuning [12]. Thus, the reduced mass and stiffness matrices of the tuned system and the mistuned components can be written as

$$\boldsymbol{\mu}^S = \begin{bmatrix} \hat{\boldsymbol{\Phi}}^{S^{\mathrm{T}}} \mathbf{M}^S \hat{\boldsymbol{\Phi}}^S & \hat{\boldsymbol{\Phi}}^{S^{\mathrm{T}}} \mathbf{M}^S \boldsymbol{\Psi}^C \\ \boldsymbol{\Psi}^{C^{\mathrm{T}}} \mathbf{M}^S \hat{\boldsymbol{\Phi}}^S & \boldsymbol{\Psi}^{C^{\mathrm{T}}} \mathbf{M}^S \boldsymbol{\Psi}^C \end{bmatrix}, \tag{3.11}$$

$$\boldsymbol{\kappa}^S = \begin{bmatrix} \hat{\boldsymbol{\Phi}}^{S^{\mathrm{T}}} \mathbf{K}^S \hat{\boldsymbol{\Phi}}^S & \hat{\boldsymbol{\Phi}}^{S^{\mathrm{T}}} \mathbf{K}^S \boldsymbol{\Psi}^C \\ \boldsymbol{\Psi}^{C^{\mathrm{T}}} \mathbf{K}^S \hat{\boldsymbol{\Phi}}^S & \boldsymbol{\Psi}^{C^{\mathrm{T}}} \mathbf{K}^S \boldsymbol{\Psi}^C \end{bmatrix}, \tag{3.12}$$

$$\boldsymbol{\mu}^{\delta} = \begin{bmatrix} \boldsymbol{\Phi}_b^{S^{\mathrm{T}}} \mathbf{M}^{\delta} \boldsymbol{\Phi}_b^{S} & \mathbf{0} \\ \mathbf{0} & \mathbf{0} \end{bmatrix}, \tag{3.13}$$

$$\boldsymbol{\kappa}^{\delta} = \begin{bmatrix} \boldsymbol{\Phi}_b^{S^{\mathrm{T}}} \mathbf{K}^{\delta} \boldsymbol{\Phi}_b^{S} & \mathbf{0} \\ \mathbf{0} & \mathbf{0} \end{bmatrix}. \tag{3.14}$$

Hence, the synthesized mass and stiffness matrices are given by

$$\boldsymbol{\mu}^{syn} = \begin{bmatrix} \hat{\boldsymbol{\Phi}}^{S^{\mathrm{T}}} \mathbf{M}^{S} \hat{\boldsymbol{\Phi}}^{S} + \boldsymbol{\Phi}_b^{S^{\mathrm{T}}} \mathbf{M}^{\delta} \boldsymbol{\Phi}_b^{S} & \hat{\boldsymbol{\Phi}}^{S^{\mathrm{T}}} \mathbf{M}^{S} \boldsymbol{\Psi}^{C} \\ \boldsymbol{\Psi}^{C^{\mathrm{T}}} \mathbf{M}^{S} \hat{\boldsymbol{\Phi}}^{S} & \boldsymbol{\Psi}^{C^{\mathrm{T}}} \mathbf{M}^{S} \boldsymbol{\Psi}^{C} \end{bmatrix}, \tag{3.15}$$

$$\boldsymbol{\kappa}^{syn} = \begin{bmatrix} \hat{\boldsymbol{\Phi}}^{S^{\mathrm{T}}} \mathbf{K}^{S} \hat{\boldsymbol{\Phi}}^{S} + \boldsymbol{\Phi}_b^{S^{\mathrm{T}}} \mathbf{K}^{\delta} \boldsymbol{\Phi}_b^{S} & \hat{\boldsymbol{\Phi}}^{S^{\mathrm{T}}} \mathbf{K}^{S} \boldsymbol{\Psi}^{C} \\ \boldsymbol{\Psi}^{C^{\mathrm{T}}} \mathbf{K}^{S} \hat{\boldsymbol{\Phi}}^{S} & \boldsymbol{\Psi}^{C^{\mathrm{T}}} \mathbf{K}^{S} \boldsymbol{\Psi}^{C} \end{bmatrix}. \tag{3.16}$$

By using CMM [12], the synthesized mass and stiffness matrices are written as follows

$$\mathbf{p}^{syn} = \begin{bmatrix} \mathbf{p}_{\phi}^{S} \\ \mathbf{u}_{c}^{S} \end{bmatrix}, \tag{3.17}$$

$$\boldsymbol{\mu}^{syn} = \begin{bmatrix} \hat{\boldsymbol{\Phi}}^{S^{\mathrm{T}}} \mathbf{M}^{S} \hat{\boldsymbol{\Phi}}^{S} & \hat{\boldsymbol{\Phi}}^{S^{\mathrm{T}}} \mathbf{M}^{S} \boldsymbol{\Psi}^{C} \\ \boldsymbol{\Psi}^{C^{\mathrm{T}}} \mathbf{M}^{S} \hat{\boldsymbol{\Phi}}^{S} & \boldsymbol{\Psi}^{C^{\mathrm{T}}} \mathbf{M}^{S} \boldsymbol{\Psi}^{C} \end{bmatrix}, \tag{3.18}$$

$$\boldsymbol{\kappa}^{syn} = \begin{bmatrix} \hat{\boldsymbol{\Phi}}^{S^{\mathrm{T}}} \mathbf{K}^{S} \hat{\boldsymbol{\Phi}}^{S} + \boldsymbol{\kappa}_{\mathrm{CMM}} & \hat{\boldsymbol{\Phi}}^{S^{\mathrm{T}}} \mathbf{K}^{S} \boldsymbol{\Psi}^{C} \\ \boldsymbol{\Psi}^{C^{\mathrm{T}}} \mathbf{K}^{S} \hat{\boldsymbol{\Phi}}^{S} & \boldsymbol{\Psi}^{C^{\mathrm{T}}} \mathbf{K}^{S} \boldsymbol{\Psi}^{C} \end{bmatrix}, \tag{3.19}$$

where $\boldsymbol{\kappa}_{\mathrm{CMM}} = \sum_{n=2}^{N} \mathbf{q}_{\phi,n}^{\mathrm{T}} diag_{r\in R}(\lambda_{r,n}^{CB} - \lambda_{r,o}^{CB}) \mathbf{q}_{\phi,n}$, $\mathbf{q}_{\phi,n}$ is a matrix containing the modal participation factors of the cantilevered blade modes into the n^{th} blade portions of modes $\boldsymbol{\Phi}^{S}$, $\lambda_{r,n}^{CB}$ is the r^{th} eigenvalue of the mistuned cantilevered blade (CB) normal mode for the n^{th} blade, $\lambda_{r,o}^{\mathrm{CB}}$ is the r^{th} eigenvalue of a tuned CB normal mode, n is the blade number, and R is the number of CB normal modes used.

One of the important advantages of the proposed modeling approach is revealed by Eq. (3.19). When many mistuning patterns have to be considered, only $\boldsymbol{\kappa}_{\mathrm{CMM}}$ needs to

be re-computed (because only $\lambda_{r,n}^{CB}$ depends on the mistuning pattern). Therefore, the proposed methodology can significantly reduce the computational cost needed to obtain ROMs of mistuned bladed disks (compared to previous methodologies [45]).

3.2.3 Mode Localization Parameter

To investigate the differences between mode localizations due to mistuning and those due to cracks, a mode localization parameter $\mathbf{L}$ can be defined as

$$L_{n,i}^{k} = \frac{\| \mathbf{\Phi}_{n,i}^{k} \|_2}{\| \mathbf{\Phi}_{i}^{k} \|_2}, \tag{3.20}$$

where n is the blade number, i is the mode number, k is the mode family, $\mathbf{\Phi}_i^k$ is the i^{th} system mode in the k^{th} mode family. Thus, $\mathbf{\Phi}_{n,i}^k$ is the n^{th} blade partition of $\mathbf{\Phi}_i^k$.

3.2.4 System Mode Residuals for Mistuned Bladed Disks with a Cracked Blade

Saito *et al.* [45] showed that cracks may lead to nonlinear behavior which can be studied using nonlinear forced response calculations. They investigated the forced responses of a mistuned bladed disk with a cracked blade using a nonlinear cracked blade model [54], and showed that the resonant peaks associated with the cracked blade are essentially nonlinear for the 10^{th} mode family (in terms of both the amplitude of vibration and the peak frequency). They suggested that localization due to cracks may be distinguishable from localization due to mistuning because localization at the cracked blade was observed to occur for various mode families. However, that observation alone is not sufficient to establish a metric for differentiating localization due to mistuning from localization due to a crack.

The key idea proposed here is to show that mode shapes of the mistuned bladed disk with a crack cannot be represented as a linear combination of mode shapes of the mistuned bladed disk without a crack. A metric is proposed to quantify this lack of linear

dependence. This metric is in essence the relative residual obtained when assuming that a set of coefficients can be used to form a linear combination of modes of the uncracked bladed disk to represent modes of the system with a crack. Since the mistuned modes of a bladed disk without a crack are a linear combination of the tuned modes of the same bladed disk, we investigate two types of residuals: residuals obtained based on normal modes of a mistuned bladed disk with no cracks, and residuals obtained based on normal modes of a tuned bladed disk. The practical reason for these two types of analysis is that we consider that one does not know the exact mistuning when one attempts to detect a crack. However, the tuned mode shapes are known, and can be used for crack detection.

Residuals for Mistuned Bladed Disks with a Cracked Blade Relative to Normal Modes of Mistuned Bladed Disks with No Cracks

To show that cracks are distinguishable from mistuning, residuals for the normal modes of the mistuned bladed disk with a cracked blade are calculated relative to the normal modes of the corresponding mistuned bladed disk with no cracks. The goal is to use quantities which can be obtained by tip timing [55] in an engine during operation. Tip timing is a non-contacting measurement method which uses optical probes. It can be used to measure the vibration displacements and frequencies of every blade on a rotating bladed disk. For tip timing, few DOFs are selected on each blade tip. Each of these DOFs corresponds to one optical probe (mounted in the early). Note that as few as just one DOF per blade can be used in the tip DOF partition. Next, one constructs two key vectors: $\mathbf{\Phi}^k_{\mathrm{CM},i}$ and $\mathbf{\Phi}^k_{\mathrm{M},i}$, where $\mathbf{\Phi}^k_{\mathrm{CM},i}$ is the tip DOF partition of the i^{th} normal mode in the k^{th} mode family of the mistuned bladed disk with a cracked blade, and $\mathbf{\Phi}^k_{\mathrm{M},i}$ is the tip DOF partition of the i^{th} normal mode in the k^{th} mode family of the mistuned bladed disk with no cracks. These components of the normal modes are used to construct $\overline{\mathbf{\Phi}}^k_{\mathrm{CM}}$ and $\overline{\mathbf{\Phi}}^k_{\mathrm{M}}$ as

follows:

$$\mathbf{\Phi}^k_{\mathrm{CM}} = \begin{bmatrix} \mathbf{\Phi}^k_{\mathrm{CM},1} \\ \vdots \\ \mathbf{\Phi}^k_{\mathrm{CM},i} \\ \vdots \\ \mathbf{\Phi}^k_{\mathrm{CM},N} \end{bmatrix}, \ \overline{\mathbf{\Phi}}^k_{\mathrm{CM}} = \frac{\mathbf{\Phi}^k_{\mathrm{CM}}}{\parallel \mathbf{\Phi}^k_{\mathrm{CM}} \parallel_2}, \tag{3.21}$$

$$\mathbf{\Phi}^k_{\mathrm{M}} = \begin{bmatrix} \mathbf{\Phi}^k_{\mathrm{M},1} \\ \vdots \\ \mathbf{\Phi}^k_{\mathrm{M},i} \\ \vdots \\ \mathbf{\Phi}^k_{\mathrm{M},N} \end{bmatrix}, \ \overline{\mathbf{\Phi}}^k_{\mathrm{M}} = \frac{\mathbf{\Phi}^k_{\mathrm{M}}}{\parallel \mathbf{\Phi}^k_{\mathrm{M}} \parallel_2}, \tag{3.22}$$

where N is the number of blades (which is equal to the number of modes in the k^{th} mode family).

The residual is defined as $\parallel \overline{\mathbf{\Phi}}^k_{\mathrm{CM}} - \overline{\mathbf{\Phi}}^k_{\mathrm{M}} \parallel_2$. Note that this residual is a scalar number between zero and 2 because $\overline{\mathbf{\Phi}}^k_{\mathrm{CM}}$ and $\overline{\mathbf{\Phi}}^k_{\mathrm{M}}$ are unit vectors. Next, we focus on differentiating cracks from mistuning using this residual. First, one may ask the question: is the crack just as mistuning? That is, can a crack on a mistuned bladed disk with a given mistuning pattern lead to a vector $\overline{\mathbf{\Phi}}^k_{\mathrm{CM}}$ which has the same shape as the vector $\overline{\mathbf{\Phi}}^k_{\mathrm{M}}$ obtained for a bladed disk with no cracks, but with some other level of mistuning in the cracked blade? To answer this question, the mistuning in the bladed disk with a cracked blade is fixed. Also, for clarity blade 1 is considered to be the cracked blade. Then, the mistuning pattern of the mistuned bladed disk with no cracks is fixed for all blades except for blade 1. The mistuning level of blade 1 is varied. Surely, the residual $\parallel \overline{\mathbf{\Phi}}^k_{\mathrm{CM}} - \overline{\mathbf{\Phi}}^k_{\mathrm{M}} \parallel_2$ will change depending on the mistuning level in blade 1. If there does not exist any mistuning level in blade 1 at which $\parallel \overline{\mathbf{\Phi}}^k_{\mathrm{CM}} - \overline{\mathbf{\Phi}}^k_{\mathrm{M}} \parallel_2$ becomes zero or very small (much smaller than 2), then

one can conclude that a crack is not similar to a change in mistuning level in the cracked blade.

Residuals for Mistuned Bladed Disks with a Cracked Blade Relative to Normal Modes of Tuned Bladed Disks

In general, mistuning levels vary randomly from blade to blade, and are not known in an operating engine. Thus, one may ask the question: can a crack in a bladed disk with a given mistuning pattern lead to vibrations which are very similar to those caused by some other mistuning pattern in the bladed disk with no cracks? To show that the normal modes of a mistuned bladed disk with a cracked blade cannot be represented by normal modes of a mistuned bladed disk with no cracks, all mistuning levels should be considered. It is already known that the normal modes of a mistuned bladed disk (with no cracks) can be represented by normal modes of a tuned bladed disk. Therefore, if the normal modes of a mistuned bladed disk with a cracked blade cannot be represented by normal modes of a tuned bladed disk, it follows that the normal modes of a mistuned bladed disk with a cracked blade cannot be represented by normal modes of a mistuned bladed disk *for any mistuning pattern*. To show that this is the case, two residuals $\mathbf{R}_{\text{full,CM}}$ and $\mathbf{R}_{\text{full,M}}$ are introduced as follows:

$$R_{\text{full,CM},i} = \frac{\| \, \mathbf{\Phi}^k_{\text{CM},i} - \mathbf{\Phi}^k_{\text{T}} \mathbf{q}^k_{\text{CM},i} \, \|_2}{\| \, \mathbf{\Phi}^k_{\text{CM},i} \, \|_2}, \tag{3.23}$$

$$R_{\text{full,M},i} = \frac{\| \, \mathbf{\Phi}^k_{\text{M},i} - \mathbf{\Phi}^k_{\text{T}} \mathbf{q}^k_{\text{M},i} \, \|_2}{\| \, \mathbf{\Phi}^k_{\text{M},i} \, \|_2}, \tag{3.24}$$

where i is the mode number, $\mathbf{\Phi}^k_{\text{CM},i}$ is the tip DOF partition of the i^{th} normal mode in the k^{th} mode family of the mistuned bladed disk with a cracked blade, $\mathbf{\Phi}^k_{\text{M},i}$ is the tip DOF partition of the i^{th} normal mode in the k^{th} mode family of the mistuned bladed disk with no cracks, and $\mathbf{\Phi}^k_{\text{T}}$ is the tip DOF partition of a set of normal modes in the k^{th} mode family of the tuned bladed disk. Coefficients $\mathbf{q}^k_{\text{CM},i}$ and $\mathbf{q}^k_{\text{M},i}$ are calculated as the solutions to two

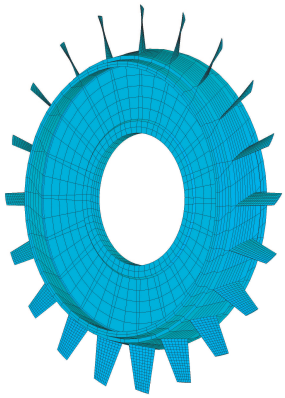

Figure 3.1: Finite element model of the bladed disk

minimization problems. Specifically, $\mathbf{q}^k_{\mathrm{CM},i}$ is the solution $\mathbf{x}$ of $\min_{\mathbf{x}} \| \boldsymbol{\Phi}^k_{\mathrm{CM},i} - \boldsymbol{\Phi}^k_{\mathrm{T}} \mathbf{x} \|_2$, and $\mathbf{q}^k_{\mathrm{M},i}$ is the solution $\mathbf{y}$ of $\min_{\mathbf{y}} \| \boldsymbol{\Phi}^k_{\mathrm{M},i} - \boldsymbol{\Phi}^k_{\mathrm{T}} \mathbf{y} \|_2$. Finally, one may note that cracks are distinguishable from mistuning for cases where the residual $\mathbf{R}_{\mathrm{full,CM}}$ is (statistically) larger than $\mathbf{R}_{\mathrm{full,M}}$.

3.3 Analysis of a Mistuned Bladed Disk with a Cracked Blade

In this section, the forced response of a mistuned bladed disk with a cracked blade is investigated using the proposed methodology. It is observed that the mode localizations due to the crack and due to mistuning are distinct across mode families. Also, it is shown that the crack is distinguishable from mistuning by the residuals of the normal modes of the bladed disk with a cracked blade relative to the normal modes of the tuned bladed disk. Furthermore, it is shown that the cracked blade is detectable (statistically). The model used in this study is that of a bladed disk with 20 blades as shown in Fig. 3.1. The key geometric characteristics are provided in Tab. 3.1. This blisk model has been used in

Table 3.1: Key geometric characteristics of the bladed disk

Outer diameter	914.99 mm
Blade span	108.43 mm
Blade chord at tip	33.67 mm
Blade chord at root	64.82 mm
Blade twist at tip	60°
Blade twist at root	30°

the past for mistuning and crack calculations [45]. It is a model that is academic, but it is also representative of actual blisk dynamics. A crack of 37.5% chord was considered on the leading edge of blade 1 at 50% span from the root of the blade. The material of the bladed disk is Titanium alloy with Young's modulus $E = 114\,\mathrm{GPa}$, density $\rho = 4,420\,\mathrm{kg/m^3}$, and Poisson's ratio $\nu = 0.31$. The full order model has $31,878$ DOFs. The damping is modeled as Rayleigh damping (without mass matrix contribution), $\mathbf{C} = \beta\mathbf{K}$, where β is a scalar (with a constant value in each frequency range of interest: $\beta = 8.376576 \times 10^{-7}$ for the 1^{st} mode family, $\beta = 2.094144 \times 10^{-7}$ for the 2^{nd} mode family, and $\beta = 2.783646 \times 10^{-8}$ for the 10^{th} mode family). For the generation of the ROMs, 12 nodes for both sides of the crack surfaces were kept as active DOFs, and 20 normal modes were used to model the remainder of the bladed disk. The resulting ROMs have 56 DOFs. The commercial software ANSYS was used to obtain mass and stiffness matrices, and mode shapes. These were then imported in Matlab and used to implement the proposed CMS-based method. The nonlinear forced response was calculated using an in-house code based on the HFT method. That code was used in the past, and its performance has been validated [45, 54].

Engine order excitation 2 was applied to obtain forced responses. This choice of engine order challenges the ROMs more than other engine orders because it is likely exciting modes in veering regions.

Blade mistuning is applied by altering the Young's modulus of the n^{th} blade by the following relationship

$$E_n = (1 + \sigma\delta_n)E_0, \tag{3.25}$$

where E_0 is the nominal Young's modulus, σ is the standard deviation of the mistuning pattern, and δ_n is the mistuning in n^{th} blade. The mistuning pattern δ has zero mean and standard deviation of 1.

The nonlinear analysis framework is as follows. A ROM is constructed using the hybrid CMS method and the CMM method for a bladed disk with a mistuning pattern given by Eq. (3.25). The HFT method is then used to obtain the nonlinear forced response. Finally, the nonlinear forced response is used to detect the presence of a crack and the blade where the crack is located.

3.3.1 Validation of Forced Responses

The nonlinear forced response was calculated using the HFT method [45, 54]. The HFT method has been numerically validated already by comparisons with direct time integration. That has been done for both simple and more complex systems. For example, the HFT method has been validated numerically for ROMs of a cantilevered cracked beam by comparisons with direct time integration [54]. The validation of the proposed method to construct ROMs is performed by comparing the predictions of the proposed ROMs with other validated numerical results. Those validated results are presented in a previous study [54] and they come from 2 sources: full-order calculations; and calculations based on another type of ROMs. Thus, for the purpose of validation, the nonlinear forced re-

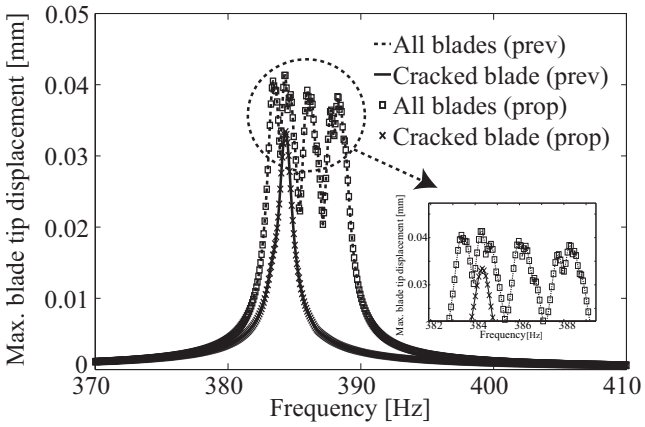

Figure 3.2: Comparison of nonlinear forced responses obtained in a previous study (prev) and those obtained using the proposed method (prop)

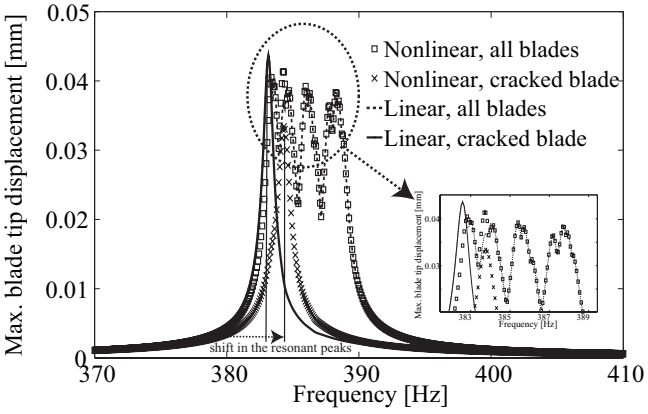

Figure 3.3: Linear and nonlinear forced responses calculated using the proposed method

sponse obtained based on the proposed method is compared to that of a previous study [45] in Fig. 3.2. The nonlinear forced response obtained from the proposed ROM matches the results of previous calculations with a 0.034% average error in the frequency range of interest. In addition, several values for the penalty coefficient and the number of harmonics have been considered for the HFT method applied to the current study. The converged values obtained were the same as in a previous study [45]: $k^* = 1.0 \times 10^6\ \mathrm{N/mm}$ and harmonics 0-9. Increasing the number of harmonics or the penalty coefficient further did not noticeably change the results.

In Fig. 3.3, linear and nonlinear responses based on the proposed method are presented. It is observed that nonlinearities have an important effect, in that the resonant peaks predicted by the nonlinear forced response are different from the ones predicted by the linear forced response, and the presence of a crack causes a shift in the resonant peaks associated with the cracked blade. This indicates that nonlinearities caused by the crack are important and are mostly localized to the cracked blade. Furthermore, the results in Figs. 3.2 and 3.3 show that the amplitude at the resonant peaks of the tip of the cracked blade in the nonlinear forced response is reduced compared to that in the linear forced response.

3.3.2 Mode Localization due to Mistuning and Cracks Across Mode Families

The mode localization parameter **L** was calculated by using Eq. (3.20) for the following cases: 1) a mistuned bladed disk with a cracked blade, 2) a mistuned bladed disk with no cracks, and 3) a bladed disk with a cracked blade and no mistuning (which we will refer to as a tuned bladed disk with a cracked blade). Two different blade mistuning patterns were employed for case 1 and case 2. The mode localization parameter $L^k_{1,i}$ was investigated (for blade 1) across mode families. As can be seen in Fig. 3.4(a), $L^k_{1,i}$ for the 1^{st} mode family in case 1 and case 3 are localized at mode number 1, which is the cracked

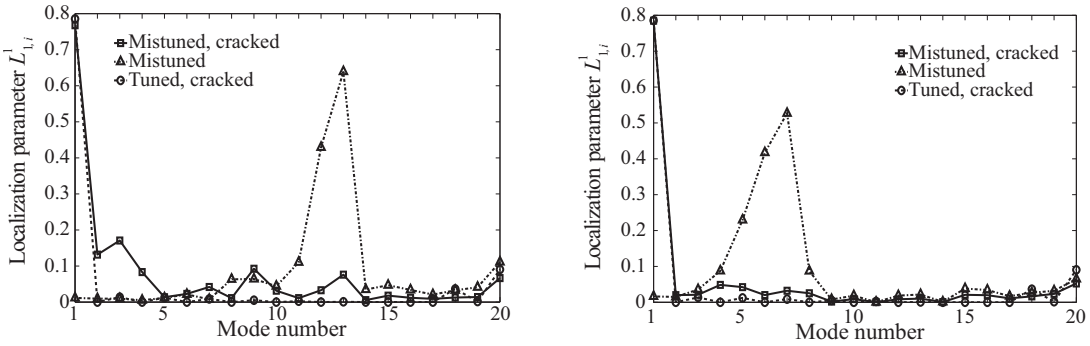

Figure 3.4: Mode localization in the 1^{st} mode family for two different mistuning patterns: (a) 1^{st} mistuning pattern, (b) 2^{nd} mistuning pattern

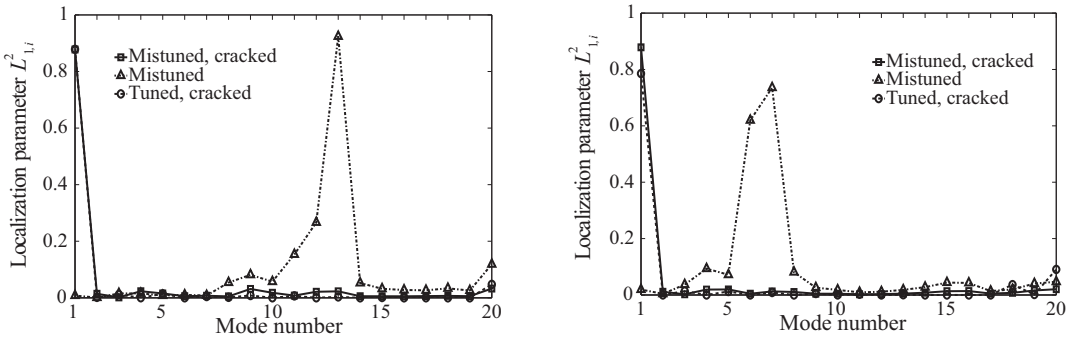

Figure 3.5: Mode localization in the 2^{nd} mode family for two different mistuning patterns: (a) 1^{st} mistuning pattern, (b) 2^{nd} mistuning pattern

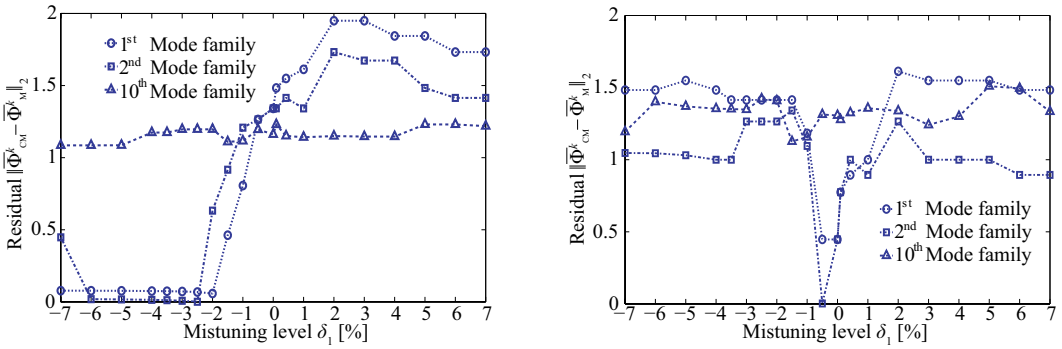

Figure 3.6: Residual $\| \overline{\mathbf{\Phi}}^k_{\mathrm{CM}} - \overline{\mathbf{\Phi}}^k_{\mathrm{M}} \|_2$ for k=1, 2, 10 for various mistuning levels in blade 1: (a) σ = 1% , (b) σ = 4%

blade dominant mode, regardless of the mistuning pattern. This mode localization (due to a crack) also appears in the 2^{nd} mode family, as can be seen in Fig. 3.5. These results indicate that cracks lead to mode localization across mode families at the cracked blade for all modes dominated by the cracked blade. In contrast, localizations due to mistuning appear on different blades depending on the mistuning pattern, as can be seen in Figs. 3.4 and 3.5

3.3.3 Distinction between Cracks and Mistuning

To be able to detect the presence of cracks in mistuned bladed disks, and to distinguish cracks from mistuning, one may use the normal modes of the mistuned bladed disk with a cracked blade, and the residuals defined in the previous section. This approach is based on linear analyses, so it is valid only when the nonlinear effects of the crack opening and closing are negligible.

The residual $\| \overline{\mathbf{\Phi}}^k_{\mathrm{CM}} - \overline{\mathbf{\Phi}}^k_{\mathrm{M}} \|_2$ was calculated by using a single DOF on each blade tip for the 1^{st}, 2^{nd}, and 10^{th} mode families while altering the mistuning level δ_1 of blade 1 in the mistuned bladed disk with no cracks. In Fig. 3.6, the horizontal axis is δ_1 and the

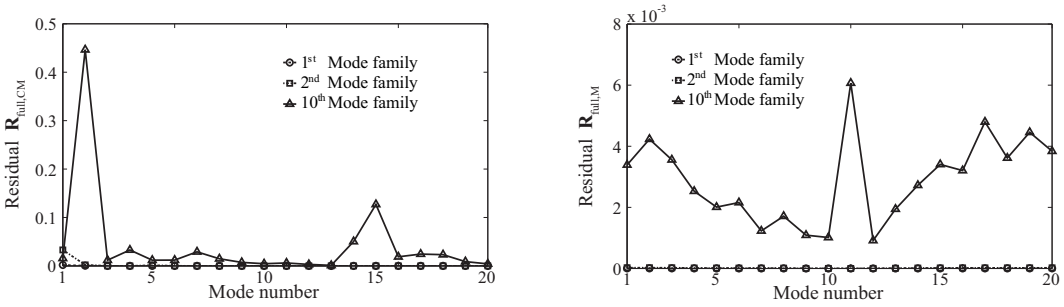

(a) (b)

Figure 3.7: Residuals $\mathbf{R}_{\text{full,CM}}$ and $\mathbf{R}_{\text{full,M}}$ when σ = 1% : (a) Residual $\mathbf{R}_{\text{full,CM}}$ for a mistuned bladed disk with a cracked blade, (b) Residual $\mathbf{R}_{\text{full,M}}$ for a mistuned bladed disk

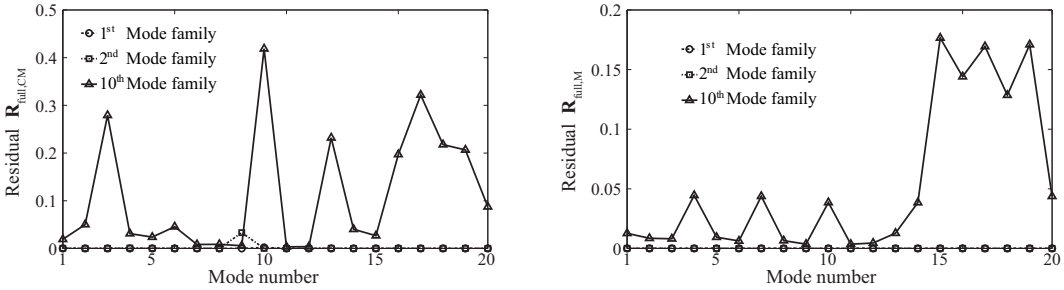

(a) (b)

Figure 3.8: Residuals $\mathbf{R}_{\text{full,CM}}$ and $\mathbf{R}_{\text{full,M}}$ when σ = 4% : (a) Residual $\mathbf{R}_{\text{full,CM}}$ for a mistuned bladed disk with a cracked blade, (b) Residual $\mathbf{R}_{\text{full,M}}$ for a mistuned bladed disk

vertical axis is the residual $\| \overline{\mathbf{\Phi}}^k_{\mathrm{CM}} - \overline{\mathbf{\Phi}}^k_{\mathrm{M}} \|_2$. As seen in Fig. 3.6(a), when σ is 1% and δ_1 is -2.5%, the residuals for the 1^{st} and 2^{nd} mode families are close to zero. This result is also obtained when σ is 4%. In Fig. 3.6(b), when δ_1 is -0.5%, the residual for the 2^{nd} mode family is almost zero. These results show that cracks are not distinguishable from mistuning if one only uses the 1^{st} and 2^{nd} mode families. That is because the residual $\| \overline{\mathbf{\Phi}}^k_{\mathrm{CM}} - \overline{\mathbf{\Phi}}^k_{\mathrm{M}} \|_2$ can be small for these families. In contrast, the residuals for the 10^{th} mode family are not zero for any mistuning level δ_1 in blade 1. Therefore, it can be concluded that cracks may be detectable using the residual $\| \overline{\mathbf{\Phi}}^k_{\mathrm{CM}} - \overline{\mathbf{\Phi}}^k_{\mathrm{M}} \|_2$ when using the 10^{th} mode family.

However, these results are valid only when the mistuning levels of other blades (2...20) are known. Thus, these results are just the starting point, and must be complemented by an analysis which considers various mistuning patterns. That analysis can be done by using the residuals $\mathbf{R}_{\mathrm{full,CM}}$ and $\mathbf{R}_{\mathrm{full,M}}$ in Eq. (3.23) and Eq. (3.24). Matrices $\mathbf{\Phi}^k_{\mathrm{CM},i}$, $\mathbf{\Phi}^k_{\mathrm{M},i}$, and $\mathbf{\Phi}^k_{\mathrm{T}}$ were constructed for k=1, 2, 10. Distinct from the calculation of $\| \overline{\mathbf{\Phi}}^k_{\mathrm{CM}} - \overline{\mathbf{\Phi}}^k_{\mathrm{M}} \|_2$, two DOFs were used on each blade tip. The resulting vectors $\mathbf{R}_{\mathrm{full,CM}}$ and $\mathbf{R}_{\mathrm{full,M}}$ were calculated for the 1^{st}, 2^{nd}, and 10^{th} mode families. The matrix $\mathbf{\Phi}^k_{\mathrm{T}}$ was obtained for each mode family. The matrices $\mathbf{\Phi}^1_{\mathrm{T}}$ and $\mathbf{\Phi}^2_{\mathrm{T}}$ contained 20 normal modes of the tuned bladed disk, while $\mathbf{\Phi}^{10}_{\mathrm{T}}$ contained 30 modes. As can be seen in Fig. 3.7, the residuals of the mistuned bladed disk with a crack $\mathbf{R}_{\mathrm{full,CM}}$ are larger than those of the mistuned bladed disk with no cracks $\mathbf{R}_{\mathrm{full,M}}$ (note the scale of 10^{-3} in the vertical axis) even for the 10^{th} mode family when σ = 1%. This result indicates that cracks are distinguishable from mistuning by comparing $\mathbf{R}_{\mathrm{full,CM}}$ and $\mathbf{R}_{\mathrm{full,M}}$ when the mistuning is small. In contrast, when σ = 4%, it appears that $\mathbf{R}_{\mathrm{full,CM}}$ and $\mathbf{R}_{\mathrm{full,M}}$ are of the same order (10^{-1}) at certain modes, as seen in Fig. 3.8. This is because $\mathbf{\Phi}^k_{\mathrm{T}}$ does not represent well neither $\mathbf{\Phi}^k_{\mathrm{CM},i}$ nor $\mathbf{\Phi}^k_{\mathrm{M},i}$.

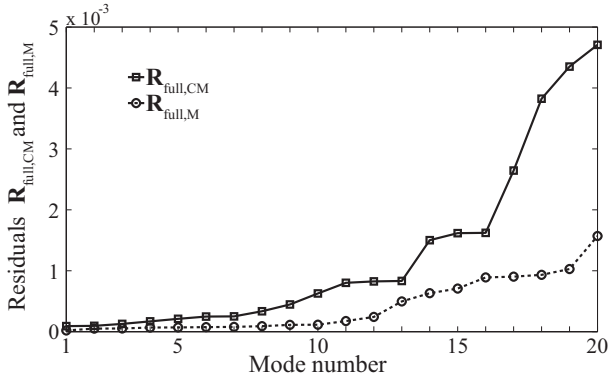

Figure 3.9: Residuals $\mathbf{R}_{\text{full,CM}}$ and $\mathbf{R}_{\text{full,M}}$ for the 10^{th} mode family; the residuals are sorted in increasing order

Hence, to distinguish cracks from mistuning for larger mistuning, $\mathbf{\Phi}^{10}_{\text{CM},i}$ and $\mathbf{\Phi}^{10}_{\text{M},i}$ were recalculated for the 10^{th} mode family by using 9 DOFs on each blade tip. Also, 78 normal modes of the tuned bladed disk were included in $\mathbf{\Phi}^{10}_{\text{T}}$ instead of just 30. These 78 modes were selected by frequency. The residuals $\mathbf{R}_{\text{full,CM}}$ and $\mathbf{R}_{\text{full,M}}$ were recalculated using Eq. (3.23) and Eq. (3.24). The results obtained are presented in Fig. 3.9, where the residuals were sorted in increasing order. These results show that $\mathbf{R}_{\text{full,CM}}$ is greater than $\mathbf{R}_{\text{full,M}}$ for the selected modes. Especially, it can be noted that $\mathbf{R}_{\text{full,CM}}$ is clearly distinct from $\mathbf{R}_{\text{full,M}}$ for modes 17-20. Therefore, one can conclude that cracks are distinguishable from mistuning even for larger mistuning.

3.3.4 Cracked Blade Location

To detect which of the blades is cracked, a third (and last) residual $\mathbf{R}_{\text{red,CM}}$ is introduced as follows

$$R_{\text{red,CM},i,n} = \frac{\| \mathbf{\Phi}^{k}_{\text{CM},i,n} - \mathbf{\Phi}^{k}_{\text{T}} \mathbf{q}^{k}_{\text{CM},i,n} \|_2}{\| \mathbf{\Phi}^{k}_{\text{CM},i,n} \|_2}, \tag{3.26}$$

where i is the mode number, n is the blade number, k is the mode family, and $\mathbf{\Phi}^{k}_{\text{CM},i,n}$ is obtained by excluding the partition of the n^{th} blade from $\mathbf{\Phi}^{k}_{\text{CM},i}$. The matrix $\mathbf{\Phi}^{k}_{\text{T}}$ is the tip

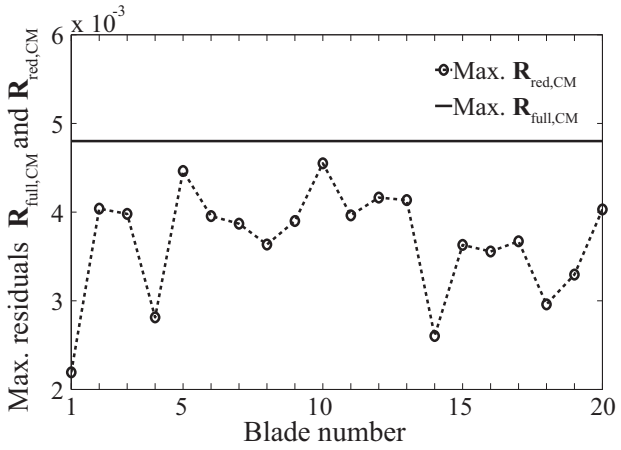

Figure 3.10: Maximum residuals $\mathbf{R}_{\text{full,CM}}$ (over all modes in the 10^{th} mode family) and $\mathbf{R}_{\text{red,CM}}$ (for all blades) for the 10^{th} mode family

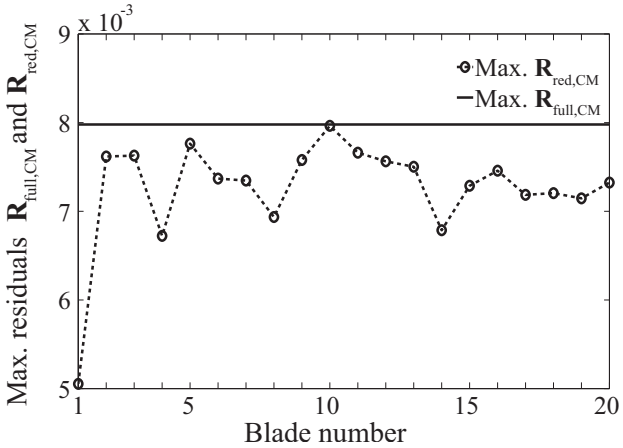

Figure 3.11: Maximum residuals $\mathbf{R}_{\text{full,CM}}$ (over all modes in the 10^{th} mode family) and $\mathbf{R}_{\text{red,CM}}$ (for all blades) for the 10^{th} mode family with 1% measurement noise

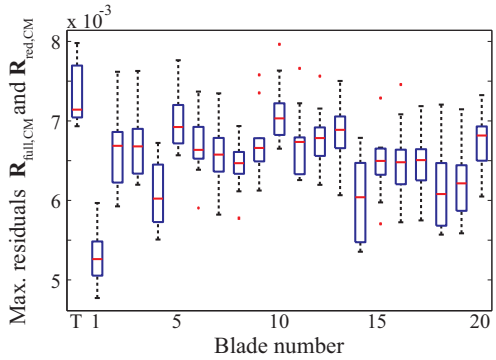

Figure 3.12: Maximum residuals $\mathbf{R}_{\text{red,CM}}$ (over all modes in the 10^{th} mode family) for all blades; 10 realizations of 1% measurement noise were used; the maximum value obtained for $\mathbf{R}_{\text{full,CM}}$ over all modes in the 10^{th} mode family is showed on the left of blade 1 (and is marked as T on the horizontal axis)

DOF partition of a set of the normal modes in the k^{th} mode family of the tuned bladed disk (as in the previous sections). The coefficient vector $\mathbf{q}^{k}_{\text{CM},i,n}$ is the solution $\mathbf{z}$ of the minimization problem $\min_{\mathbf{z}} \| \mathbf{\Phi}^{k}_{\text{CM},i,n} - \mathbf{\Phi}^{k}_{\text{T}} \mathbf{z} \|_2$.

The residual $\mathbf{R}_{\text{full,CM}}$ and $\mathbf{R}_{\text{red,CM}}$ were calculated using Eq. (3.23) and Eq. (3.26). Next, the maximum value of $\mathbf{R}_{\text{full,CM}}$ over all modes in the 10^{th} mode family was plotted in Fig. 3.10 together with the maximum values of $\mathbf{R}_{\text{red,CM}}$ obtained separately for each blade (over all the modes in the 10^{th} mode family). One may note that the maximum value of the residual $\mathbf{R}_{\text{red,CM}}$ obtained for blade 1 is smallest, which indicates that blade 1 affects $\mathbf{R}_{\text{full,CM}}$ more significantly than any other blade. Namely, the difference between $\mathbf{R}_{\text{full,CM}}$ and $\mathbf{R}_{\text{red,CM}}$ is mainly induced by blade 1. Therefore, it can be inferred that blade 1 is the cracked blade.

To apply the proposed method for detection of a cracked blade in real bladed disks, it is required to measure the motion of points on the tip of the blades using tip timing. These measurements are likely corrupted by measurement noise. To investigate the effects of the measurement noise, 1% measurement noise (random noise with a uniform distribution)

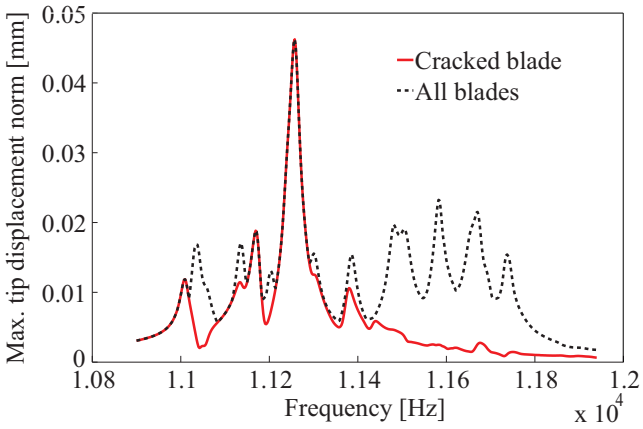

Figure 3.13: Nonlinear forced response of the mistuned bladed disk with a cracked blade

was applied to $\mathbf{\Phi}^{10}_{\mathrm{CM},i}$. Then, $\mathbf{R}_{\mathrm{full,CM}}$ and $\mathbf{R}_{\mathrm{red,CM}}$ were recalculated using Eq. (3.23) and Eq. (3.26). As seen in Fig. 3.11, even in the presence of measurement noise, the maximum value of the residual $\mathbf{R}_{\mathrm{red,CM}}$ obtained for blade 1 is the lowest.

To conduct a statistical study with respect to the measurement noise, 10 different realizations of 1% measurement noise were employed. In Fig. 3.12, box plots for the maximum residuals of $\mathbf{R}_{\mathrm{full,CM}}$ and $\mathbf{R}_{\mathrm{red,CM}}$ across blades are presented. The box plotted on the left of blade 1 and marked as T on the horizontal axis is for $\mathbf{R}_{\mathrm{full,CM}}$. For both $\mathbf{R}_{\mathrm{full,CM}}$ and $\mathbf{R}_{\mathrm{red,CM}}$, the maximum values over all modes in the 10^{th} mode family are used in the statistical calculation. Note that the box in the plot spans between values of $\pm$ one standard deviation from the mean. The dashes inside each box indicates median value. The dashed lines mark the range from the minimum to the maximum values. As shown in Fig. 3.12, blade 1 is notably distinct from all other (uncracked) blades. Therefore, it can be concluded statistically that blade 1 has a crack.

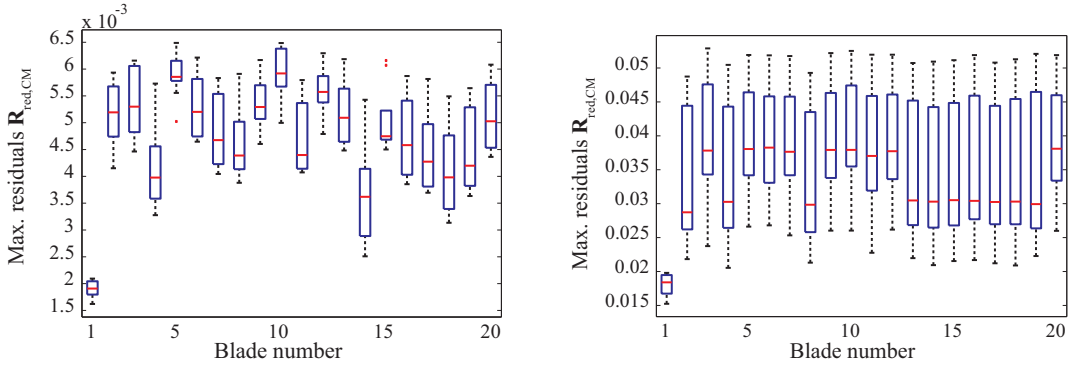

(a) (b)

Figure 3.14: Maximum residuals $\mathbf{R}_{\mathrm{red,CM}}$ with 1% and 10% measurement noise using nonlinear forced response data for 10 realizations of measurement noise: (a) 1% measurement noise, (b) 10% measurement noise

3.3.5 Nonlinearity due to Cracks

In the previous sections, normal modes of mistuned bladed disks with a cracked blade were obtained without considering the nonlinearity due to the crack opening and closing. However, the nonlinearity can change the forced responses of bladed disks in terms of both the amplitude of vibration and the peak frequency. Therefore, the nonlinearity due to the crack has to be considered. In Fig. 3.13, the nonlinear forced response of a mistuned bladed disk with a cracked blade was calculated using engine order excitation 2 for a mistuning pattern with a standard deviation σ of 4%. One resonant frequency (denoted by superscript g) associated with the maximum amplitude of vibration of the cracked blade was selected. Next, a vector $\mathbf{\Phi}^{g}_{\mathrm{CM},i}$ was computed for the dynamic response at this frequency. Distinct from the linear analysis in the previous sections, $\mathbf{\Phi}^{g}_{\mathrm{CM},i}$ was obtained from the computed time history of the nonlinear vibration. Distinct from Eq. (3.26), here the mode shape information was replaced by displacement information gathered from the nonlinear (harmonic balance) HFT solution. The displacement information for each se-

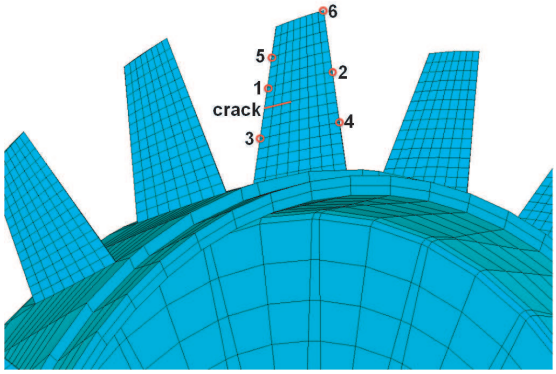

Figure 3.15: Forcing points used for traveling wave excitation

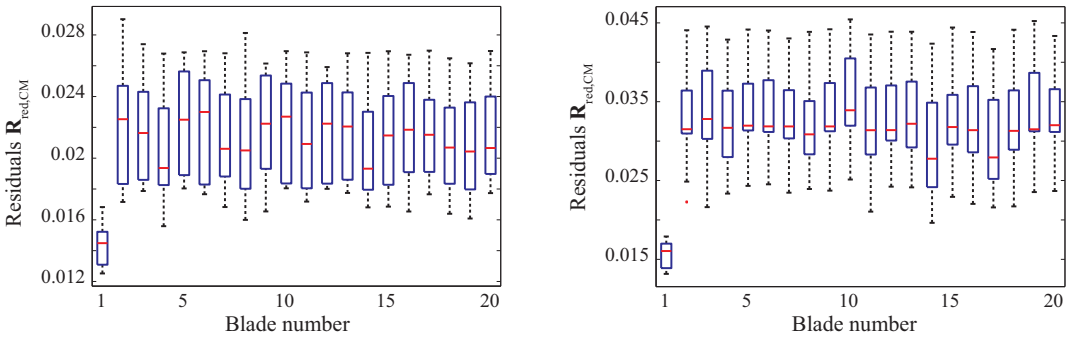

(a) (b)

Figure 3.16: Residuals $\mathbf{R}_{\text{red,CM}}$ for mode g for 10 realizations of measurement noise using nonlinear forced responses computed using different forcing points: (a) Forcing applied at point 4, (b) Forcing applied at point 6

lected DOF on the tip of the blade was collected at steady state (nonlinear resonance) conditions. One DOF on the tip of one blade is chosen as a reference (e.g., blade 1). Next, the displacements of a few other selected DOFs on the tip of each blade are collected at the instances (in time) when the displacement at the reference DOF is at its maximum value. These time instances are selected because the crack is most likely open when the displacement of the reference DOF on the tip of the cracked blade is the largest.

To reduce the measurement cost, only 6 DOFs were selected on each blade tip. One of the 6 DOFs on blade 1 was chosen as reference. Residuals $\mathbf{R}_{\mathrm{red,CM}}$ were calculated for 1% and 10% measurement noise using Eq. (3.26) for 10 noise realizations. As can be seen in Fig. 3.14, even for 10% measurement noise, $\mathbf{R}_{\mathrm{red,CM}}$ for the cracked blade is statistically distinct from other blades.

To investigate the influence of the forcing point, several excitation points were selected (on each blade) as shown in Fig. 3.15. The forcing considered is still an engine order excitation. In Fig. 3.16, the results for forcing points 4 and 6 with an engine order excitation 2 are presented. These results show that $\mathbf{R}_{\mathrm{red,CM}}$ for the cracked blade is distinct from all other blades regardless of the forcing point even for 10% measurement noise. Thus, the cracked blade can be detected successfully using the proposed methodology even when the nonlinearity due to the crack is considerable.

3.4 Conclusions

An efficient and novel methodology to investigate the nonlinear forced response of mistuned bladed disks with a cracked blade was developed. Efficient ROMs were constructed from hybrid CMS and CMM. The forced response of mistuned bladed disks with a cracked blade was obtained by using the proposed models and nonlinear time integration. The results were compared to those of a previous method [45]. It was shown that

blade mistuning can be projected efficiently to reduce the computational cost. This is an advantage which plays an important role when the calculation of system normal modes of a mistuned bladed disk is needed for many mistuning patterns.

Furthermore, a novel methodology to detect the presence of a crack in mistuned bladed disks was presented. By investigating mode localizations due to cracks and mistuning, it was first shown that cracks lead to a mode localization which is different from localizations due to mistuning. Then, it was observed that mode shapes of the cracked structure are not a linear combination of tuned system modes. This observation was used for damage detection. Since mode shapes of the healthy mistuned bladed disk are a linear combination of tuned mode shapes, the observation allows for the first time to differentiate the effects of cracks from the effects of mistuning. Based on this result, the proposed method is then able to detect the presence of damage by using tip timing data only (even in the presence of nonlinearities caused by the crack opening and closing). This is accomplished by using the residuals defined in Eqs. (23) and (24). These residuals can be gathered through experimental measurements and are novel means for damage detection. They prove to be the key for identifying the presence of damage and even more importantly, statistically detecting the blade where the damage is present even in the presence of measurement noise.

CHAPTER IV

Bilinear Amplitude Approximation for Piecewise-Linear Oscillators

4.1 Introduction

Recently, the interest in monitoring the vibration of dynamical systems has been increasing. For example, large and complex air and space structures include vibration monitoring systems to forecast sudden failures. Such vibration monitoring is used to diagnose structural health by analyzing vibration characteristics (such as frequency and amplitude). Among the vibration characteristics used, the vibration amplitude is especially important because it can directly affect stresses and thus the life of the system.

Finite element (FE) models are often used to analyze vibration characteristics. For low dimensional systems, full FE models can be used. For high dimensional systems, the computational cost of analyzing full FE models can often be prohibitive. To circumvent this difficulty, many methods for creating reduced-order models (ROMs) have been developed for various systems [1, 13, 14, 17, 30, 32, 84–91], with the majority being focused on linear systems. ROMs for linear systems can be efficiently constructed by using approaches based on linear transformations [92, 93] such as component mode synthesis (CMS) [51]. However, constructing ROMs for systems with piecewise-linear nonlinearity (caused for example by intermittent contact) require careful treatment. Accurate ROMs can be con-

structed for such systems using linear transformations [94–97], or using nonlinear normal modes [98–100]. Recently, Saito et al. [41] developed a reduced-order modeling method based on bilinear modes (BLMs) for dynamical systems with piecewise-linear nonlinearity. They observed that the space spanned by the most dominant proper orthogonal modes (POMs) of a system is also spanned by a set of linear normal modes for the system with special boundary conditions at the surface where the intermittent contact takes place. These special modes were referred to as BLMs. Hence, the most dominant POMs are well approximated by linear combinations of BLMs. The ROMs based on BLMs were shown to be accurate and have a low dimension. Nonetheless, predicting the vibration amplitude requires the calculation of the nonlinear forced response of the ROMs. One way to obtain the nonlinear forced responses is direct numerical calculation (e.g., by using a variable step Runge-Kutta method), which incurs a large computational cost despite the fact that the ROMs are low dimensional. Therefore, to obtain the amplitude of vibration at resonant frequencies, nonlinear forced responses need to be calculated using more efficient numerical methods (e.g., hybrid frequency/time domain methods) [39, 45, 46, 54, 101].

In this paper, a novel technique to approximate the vibration amplitude at the resonant frequencies of dynamical systems with piecewise-linear nonlinearity is proposed. Here, it is assumed that the forcing applied to the system is harmonic and the response of the system is periodic. Thus, quasi-periodic or chaotic dynamics are not considered. The proposed technique is referred to as bilinear amplitude approximation (BAA). BAA constructs approximations for the periodic steady-state response of the system at resonant frequencies. For example, consider that a structure has a crack which opens and closes during each vibration cycle. BAA uses linear modes (similar to BLMs) from two different systems: one with an open crack and the other where there is sliding at the crack surfaces. By doing so, BAA does not require the numerical integration of nonlinear ROMs to

calculate the vibration amplitude at resonant frequencies. Consequently, large savings in computational costs are obtained.

In the following, BAA is introduced. Next, the application of BAA to a single-degree-of-freedom system is demonstrated. After that, a more general application of BAA is demonstrated for a three-degree-of-freedom example. Then, results comparing numerical solutions from a nonlinear analysis and results obtained using BAA for a full blisk with a crack are presented. Finally, conclusions are presented.

4.2 Methodology

In this section, BAA is introduced. Consider an elastic structure which undergoes intermittent contact (leading to piecewise-linear nonlinearity). During each vibration cycle, the structure has three different states: (1) fully open (i.e., no contact), (2) fully sliding (i.e., complete contact), and (3) partially open (i.e., partial contact between the contacting surfaces). The goal of BAA is to find the steady-state amplitude of vibration of the system when excited by harmonic forcing under the following assumptions:

(a) state (3) (partially open) lasts a much shorter time interval than states (1) and (2),

(b) the motion of the structure is periodic,

(c) during each vibration cycle there is only one time interval when the system is in state (1) and only one time interval when the system is in state (2); thus, one entire vibration cycle is approximated by states (1) and (2),

(d) the motion in states (1) and (2) lies in the space spanned by a few dominant modes of the structure open at the contact surfaces and a few dominant modes of the structure with sliding at the contact surfaces.

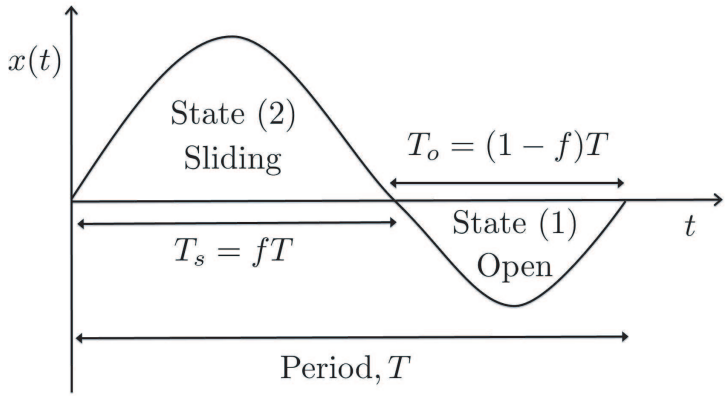

Figure 4.1: One steady-state vibration cycle

Assumption (a) is in fact exactly satisfied when the gap at the contacting surfaces is zero for the structure with zero internal stresses [41, 46]. The motion of one steady-state vibration cycle for one of the degrees-of-freedom (DOFs) of the system is schematically shown in Fig. 4.1. The total period T of the periodic response is broken into the time T_o that the system spends in state (1), and the time T_s that the system spends in state (2). The fraction of the entire period T that the system is in state (2) is $f = T_s/T$.

Consider a multi-DOF system. The exact equations which govern the motion in state (1) and in state (2) can be expressed as

$$\begin{aligned} \mathbf{M}_o\ddot{\mathbf{x}}_o(t) + \mathbf{C}_o\dot{\mathbf{x}}_o(t) + \mathbf{K}_o\mathbf{x}_o(t) &= \mathbf{F}(t), \\ \mathbf{M}_s\ddot{\mathbf{x}}_s(t) + \mathbf{C}_s\dot{\mathbf{x}}_s(t) + \mathbf{K}_s\mathbf{x}_s(t) &= \mathbf{F}(t), \end{aligned} \tag{4.1}$$

where the subscript o refers to state (1), the subscript s refers to state (2), $\mathbf{M}_o$ and $\mathbf{M}_s$ are the mass matrices, $\mathbf{C}_o$ and $\mathbf{C}_s$ are the damping matrices, $\mathbf{K}_o$ and $\mathbf{K}_s$ are the stiffness matrices, and $\mathbf{F}$ is a periodic external force with frequency ω. The mode shapes which dominate the motion of the structure in states (1) and (2) are grouped in matrices $\mathbf{\Phi}_o$ and $\mathbf{\Phi}_s$. These matrices can be computed using the open and sliding mass and stiffness

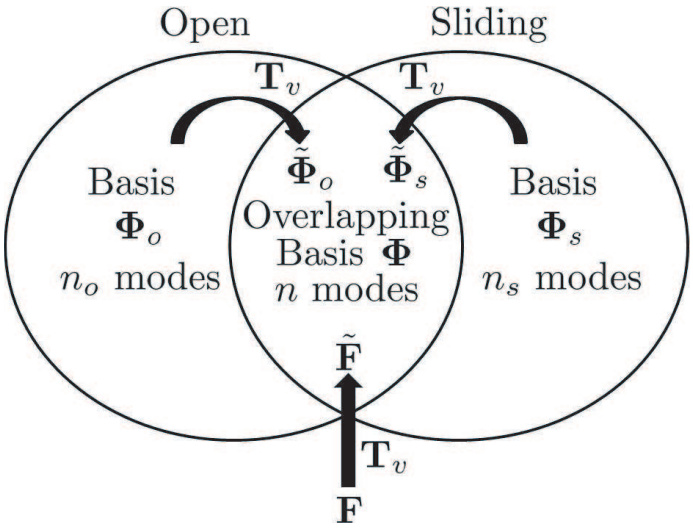

Figure 4.2: Transformation from physical space to overlapping space using $\mathbf{T}_v$

matrices.

During the vibration cycle, the system transitions from state (1) to state (2) and vice versa. At the moment of transition, compatibility conditions in terms of displacement and velocity should be satisfied. However, the space spanned by the open modes and the space spanned by the sliding modes are not perfectly aligned due to the difference in boundary conditions at the contact surfaces. Thus, to apply compatibility conditions, one needs to consider the overlapping space between the open space and the sliding space. This overlapping space is characterized by a set of basis vectors grouped in a matrix $\mathbf{\Phi}$. To obtain $\mathbf{\Phi}$, one can construct a matrix composed of $\mathbf{\Phi}_o$ and $\mathbf{\Phi}_s$ first. Then, using a singular value decomposition (SVD), the left singular vectors corresponding to large (one or two) singular values are selected. These singular vectors are used as basis vectors for the overlapping space.

As shown in Fig. 4.2, physical motions (spanned by open and sliding modes respectively) and forces can be transformed to the overlapping space $\mathbf{\Phi}$ using an operator $\mathbf{T}_v$,

which is defined as $\mathbf{T}_v = \mathbf{\Phi}(\mathbf{\Phi}^{\mathrm{T}}\mathbf{\Phi})^{-1}\mathbf{\Phi}^{\mathrm{T}}$. These transformations are needed because the motion along the overlapping space is allowed to grow (especially at resonance), while the rest of the motion is lost at the impact which takes place each time the system transitions from open to sliding and vice versa. This impact can be viewed as an elastic impact in the space spanned by $\mathbf{\Phi}$ and as a plastic impact in the remaining space. The energy before and after the impact are distinct because the plastic component of the impact leads to energy loss. The linear and angular momentum of the system are also distinct before and after the impact because of the impulse forces which act at the other (fixed) boundaries of the system. The linear and angular momentum are thus conserved only in the overlapping space $\mathbf{\Phi}$.

Using modal transformations $\mathbf{x}_o = \mathbf{\Phi}_o\mathbf{q}_o$ and $\mathbf{x}_s = \mathbf{\Phi}_s\mathbf{q}_s$, where $\mathbf{q}_o$ and $\mathbf{q}_s$ are modal coordinates, Eq. (4.1) can be projected along $\mathbf{\Phi}_o$ and $\mathbf{\Phi}_s$ to obtain

$$\begin{aligned} \mathbf{\Phi}_o^{\mathrm{T}}\mathbf{M}_o\mathbf{\Phi}_o\ddot{\mathbf{q}}_o + \mathbf{\Phi}_o^{\mathrm{T}}\mathbf{C}_o\mathbf{\Phi}_o\dot{\mathbf{q}}_o + \mathbf{\Phi}_o^{\mathrm{T}}\mathbf{K}_o\mathbf{\Phi}_o\mathbf{q}_o &= \mathbf{\Phi}_o^{\mathrm{T}}\mathbf{F}(t), \\ \mathbf{\Phi}_s^{\mathrm{T}}\mathbf{M}_s\mathbf{\Phi}_s\ddot{\mathbf{q}}_s + \mathbf{\Phi}_s^{\mathrm{T}}\mathbf{C}_s\mathbf{\Phi}_s\dot{\mathbf{q}}_s + \mathbf{\Phi}_s^{\mathrm{T}}\mathbf{K}_s\mathbf{\Phi}_s\mathbf{q}_s &= \mathbf{\Phi}_s^{\mathrm{T}}\mathbf{F}(t). \end{aligned} \tag{4.2}$$

If the damping is proportional, then Eq. (4.2) can be rewritten as

$$\begin{aligned} \ddot{q}_{o,i} + 2\zeta_{o,i}\omega_{o,i}\dot{q}_{o,i} + \omega_{o,i}^2 q_{o,i} &= f_{o,i}, \quad i = 1, ..., n_o, \\ \ddot{q}_{s,j} + 2\zeta_{s,j}\omega_{s,j}\dot{q}_{s,j} + \omega_{s,j}^2 q_{s,j} &= f_{s,j}, \quad j = 1, ..., n_s, \end{aligned} \tag{4.3}$$

where n_o and n_s are the number of modes used to expand the motion in state (1) and (2) respectively, $\zeta_{o,i}$ and $\zeta_{s,j}$ are the viscous damping ratios, $\omega_{o,i}$ and $\omega_{s,j}$ are the undamped natural frequencies associated with $\mathbf{\Phi}_{o,i}$ and $\mathbf{\Phi}_{s,j}$, and $f_{o,i}$ and $f_{s,j}$ are modal forces corresponding to $\mathbf{F}$. Using Eq. (4.3), the modal coordinates corresponding to the linear modes

$\mathbf{\Phi}_{o,i}$ and $\mathbf{\Phi}_{s,j}$ can be expressed as

$$\begin{aligned} q_{o,i}(t) &= e^{-\zeta_{o,i}\omega_{o,i}t}(o_{1,i}\cos(\omega_{od,i}t) + o_{2,i}\sin(\omega_{od,i}t)) \\ &\quad + \frac{(f_{o,i}/\omega_{o,i}^2)\cos(\omega t - \theta_{o,i} + \alpha)}{\sqrt{(1-(\omega/\omega_{o,i})^2)^2 + (2\zeta_{o,i}\omega/\omega_{o,i})^2}}, \\ q_{s,j}(t) &= e^{-\zeta_{s,j}\omega_{s,j}t}(s_{1,j}\cos(\omega_{sd,j}t) + s_{2,j}\sin(\omega_{sd,j}t)) \\ &\quad + \frac{(f_{s,j}/\omega_{s,j}^2)\cos(\omega t - \theta_{s,j} + \alpha)}{\sqrt{(1-(\omega/\omega_{s,j})^2)^2 + (2\zeta_{s,j}\omega/\omega_{s,j})^2}}, \end{aligned} \tag{4.4}$$

where $o_{1,i}$, $o_{2,i}$, $s_{1,j}$, and $s_{2,j}$ are scalar coefficients, $\omega_{od,i}$ and $\omega_{sd,j}$ are the damped frequencies corresponding to the natural frequencies $\omega_{o,i}$ and $\omega_{s,j}$, $\theta_{o,i} = \arctan(\frac{2\zeta_{o,i}\omega_{o,i}\omega}{\omega_{o,i}^2-\omega^2})$, $\theta_{s,j} = \arctan(\frac{2\zeta_{s,j}\omega_{s,j}\omega}{\omega_{s,j}^2-\omega^2})$. The angle α is the phase difference between the excitation and the piece-wise linear response. This angle is key to accurately capture the energy loss in the presence of bilinearity. There are $2n_o+2n_s+2$ unknowns in Eq. (4.4): the phase angle α, the time fraction variable f, and the $2n_o + 2n_s$ coefficients of $o_{1,i}$, $o_{2,i}$ for $i = 1, ..., n_o$, and $s_{1,j}$, $s_{2,j}$ for $j = 1, ..., n_s$. Similar to the arguments used in bilinear frequency approximation (BFA) [102], T_o and T_s can be approximated by $T_o \cong \frac{2\pi}{\omega_o}$ and $T_s \cong \frac{2\pi}{\omega_s}$. Thus, the fraction f can be approximated by

$$f_a = \frac{T_s}{T_o + T_s} \cong \frac{\omega_o}{\omega_o + \omega_s}. \tag{4.5}$$

To calculate the remaining unknowns, one can enforce transition conditions related to the continuity of the physical displacement and velocity at the instances when the system transitions from state (1) to state (2) and vice versa. The displacement continuity gives

$$\begin{aligned} \mathbf{x}_s(T_s + \alpha) &= \mathbf{x}_o(T_s + \alpha), \\ \mathbf{x}_s(\alpha) &= \mathbf{x}_o(T_o + T_s + \alpha), \end{aligned} \tag{4.6}$$

where $\mathbf{x}_o$ and $\mathbf{x}_s$ represent the physical displacement of the system in state (1) and (2). The first relation in Eq. (4.6) corresponds to the case where the system moves from the

sliding state to the open state. Note that $\mathbf{x}_o = \mathbf{\Phi}_o \mathbf{q}_o$, $\mathbf{x}_s = \mathbf{\Phi}_s \mathbf{q}_s$ and $\mathbf{\Phi}_o$ and $\mathbf{\Phi}_s$ are not completely overlapping. For most systems the dimensionality of the spaces which do not overlap are larger than the n_o and n_s. Hence, the top relation in Eq. (4.6) admits only the trivial solution, namely $\mathbf{x}_s(T_s + \alpha) = \mathbf{0}$ and $\mathbf{x}_o(T_s + \alpha) = \mathbf{0}$. Thus, the first relation in Eq. (4.6) can be replaced with $\mathbf{q}_s(T_s + \alpha) = \mathbf{0}$ and $\mathbf{q}_o(T_s + \alpha) = \mathbf{0}$. By using similar arguments, the second relation in Eq. (4.6) can be replaced with $\mathbf{q}_s(\alpha) = \mathbf{0}$ and $\mathbf{q}_o(T_o + T_s + \alpha) = \mathbf{0}$.

Next, transition conditions related to velocity are enforced. Specifically, the velocity in the overlapping space remains the same before and after a transition. Note that the linear and angular momentum are not the same before and after a transition. That is because of the impulsive forces which act at the other (fixed) boundaries of the system. The velocity in state (1) and (2) can be written as $\dot{\mathbf{x}}_o = \mathbf{\Phi}_o \dot{\mathbf{q}}_o$ and $\dot{\mathbf{x}}_s = \mathbf{\Phi}_s \dot{\mathbf{q}}_s$. Thus, the components of velocity in the overlapping space can be written as $\dot{\tilde{\mathbf{x}}}_o = \mathbf{T}_v \dot{\mathbf{x}}_o$ and $\dot{\tilde{\mathbf{x}}}_s = \mathbf{T}_v \dot{\mathbf{x}}_s$. Thus, $\dot{\tilde{\mathbf{x}}}_o = \mathbf{T}_v \mathbf{\Phi}_o \dot{\mathbf{q}}_o$ and $\dot{\tilde{\mathbf{x}}}_s = \mathbf{T}_v \mathbf{\Phi}_s \dot{\mathbf{q}}_s$. The velocity transition conditions become

$$\begin{aligned} \tilde{\mathbf{\Phi}}_s \dot{\mathbf{q}}_s(T_s + \alpha) &= \tilde{\mathbf{\Phi}}_o \dot{\mathbf{q}}_o(T_s + \alpha), \\ \tilde{\mathbf{\Phi}}_s \dot{\mathbf{q}}_s(\alpha) &= \tilde{\mathbf{\Phi}}_o \dot{\mathbf{q}}_o(T_o + T_s + \alpha), \end{aligned} \tag{4.7}$$

where $\tilde{\mathbf{\Phi}}_o = \mathbf{T}_v \mathbf{\Phi}_o$, $\tilde{\mathbf{\Phi}}_s = \mathbf{T}_v \mathbf{\Phi}_s$ are open modes projected onto the overlapping space, and sliding modes projected onto the overlapping space respectively.

By combining the displacement and velocity transition conditions, one obtains

$$\begin{aligned}
\mathbf{q}_s(T_s+\alpha) &= \mathbf{0},\\
\mathbf{q}_o(T_s+\alpha) &= \mathbf{0},\\
\mathbf{q}_s(\alpha) &= \mathbf{0},\\
\mathbf{q}_o(T_o+T_s+\alpha) &= \mathbf{0},\\
\tilde{\mathbf{\Phi}}_s\dot{\mathbf{q}}_s(T_s+\alpha) &= \tilde{\mathbf{\Phi}}_o\dot{\mathbf{q}}_o(T_s+\alpha),\\
\tilde{\mathbf{\Phi}}_s\dot{\mathbf{q}}_s(\alpha) &= \tilde{\mathbf{\Phi}}_o\dot{\mathbf{q}}_o(T_o+T_s+\alpha).
\end{aligned} \tag{4.8}$$

These transition conditions have a nonlinear dependence on the unknowns, therefore a nonlinear solver can be employed to find the solution. In this work, the function "lsqnonlin" from Matlab was used to solve for the unknowns by minimizing the residual in the 6 relations in Eq. (4.8). Using Eq. (4.4), one can construct $q_{o,i}$ and $q_{s,j}$ with the obtained $o_{1,i}, o_{2,i}, s_{1,j}, s_{2,j}$ and α. Then, physical displacements $\mathbf{x}_o$ and $\mathbf{x}_s$ are calculated using $\mathbf{x}_o = \mathbf{\Phi}_o\mathbf{q}_o$ and $\mathbf{x}_s = \mathbf{\Phi}_s\mathbf{q}_s$. One steady-state vibration cycle can be constructed using the obtained $\mathbf{x}_o$ and $\mathbf{x}_s$ with time fraction f as shown in Fig. 4.1. Finally, one can calculate the amplitude of the constructed steady-state vibration cycle, which is the approximate amplitude of the steady-state vibration of a system with piecewise-linear nonlinearity.

The motion which is not along the overlapping space has zero displacement and velocity after each transition (at the beginning of each of the two states 1 and 2). In addition, the motion which is not along the overlapping space does not have time to grow. Thus, it has negligible influence on the vibration of the system compared to the motion in the overlapping space. Hence, the forcing which is not along the overlapping space has a negligible effect. Therefore, the force $\mathbf{F}$ in the physical space can be approximated by the force $\tilde{\mathbf{F}} = \mathbf{T}_v\mathbf{F}$ in the overlapping space as shown in Fig. 4.2. Hence, the forcing in the overlapping space $\tilde{\mathbf{F}}$ can be used instead of $\mathbf{F}$ when calculating the modal forces $f_{o,i}$ and

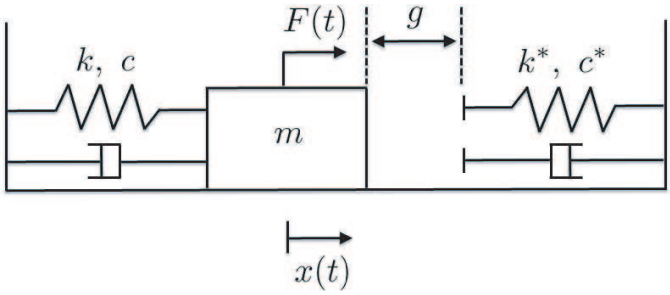

Figure 4.3: Single-DOF system

$f_{s,j}$ in Eq. (4.3), namely $\mathbf{f}_o = \mathbf{\Phi}_o^{\mathrm{T}}\tilde{\mathbf{F}}$ and $\mathbf{f}_s = \mathbf{\Phi}_s^{\mathrm{T}}\tilde{\mathbf{F}}$.

4.3 Results

In this section, the amplitude of a single-DOF system with a piecewise-linear nonlinearity is obtained first by solving the exact equations of motion using direct numerical integration. Then, BAA is employed to calculate an approximated amplitude, and the results are compared. Next, the response of a three-DOF system is calculated using direct numerical simulation. BAA is employed, and the results are compared to direct numerical simulation. Finally, nonlinear forced responses of a bladed disk with a crack are calculated. BAA is employed and the results are compared.

4.3.1 Single-Degree-of-Freedom System

The damped single-DOF system used is shown in Fig. 4.3, where $m = 2.0$ kg, $k = 2.0$ N/m, $c = 0.04$ kg/s, $k^* = 0.4$ N/m, $c^* = 0.008$ kg/s and the initial gap g is zero. The mass is excited by a harmonic force $F(t)$ of amplitude 0.01 N. It is assumed that there is no friction between the mass and ground.

The exact amplitude of the nonlinear periodic response of the system shown in Fig. 4.3 at the resonant frequency ($\omega = 0.1663$ Hz) was computed to be 0.2163 m by direct nu-

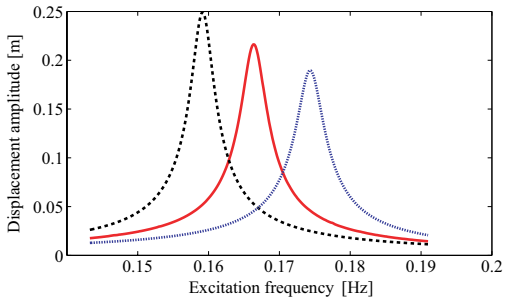

Figure 4.4: Amplitude of the nonlinear motion (—), the linear motion if the system was in state (1) only (– – –), and the linear motion if the system was in state (2) only ($\cdot\cdot\cdot$)

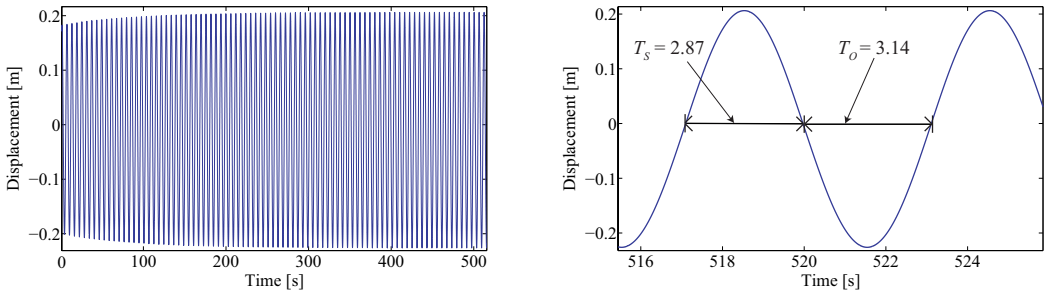

Figure 4.5: Displacement vs. time for a forcing at the resonant frequency of $\omega = 0.1663$ Hz

merical integration. A plot of the amplitude of the response versus excitation frequency for three different cases is plotted in Fig. 4.4. The three cases are: the nonlinear system, the system permanently in state (1), and the system permanently in state (2). Note that state (3) (partially open) does not exist in this system.

The steady-state nonlinear response at the resonant frequency ($\omega = 0.1663$ Hz) is shown in Fig. 4.5. In this figure, it is shown that $T_o = 3.14$ s and $T_s = 2.87$ s. The total period T was calculated using the excitation frequency ω, where $T = \frac{2\pi}{\omega}$. The exact fraction ratio f_e was calculated using $f_e = \frac{T_s}{T} = 0.4773$. The motion in states (1) and (2)

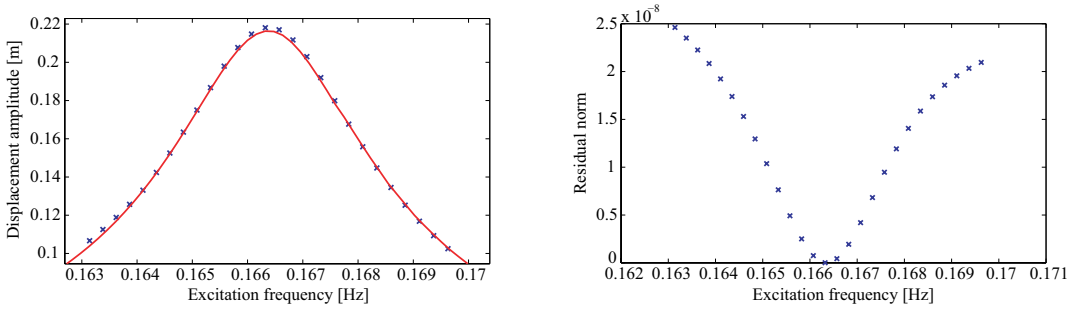

(a) (b)

Figure 4.6: (a) Comparison of amplitudes computed using BAA ($\times$) versus time integration (—) and (b) the residual obtained when solving for the unknown coefficients in BAA for the single-DOF system

of the system can be distinguished based on the following displacement conditions

$$\begin{aligned} x(t) &< 0, \quad \text{state } (1), \\ x(t) &\geq 0, \quad \text{state } (2). \end{aligned} \tag{4.9}$$

Since there exists only one DOF in the system, the exact equations of motion in state (1) and state (2) can be directly obtained using Eq. (4.4) because, in this simple case, the modal coordinate q is the same as the physical coordinate x. As explained in the methodology section, six unknowns need to be obtained to approximate the nonlinear response, namely the phase angle α, the time fraction f, and the four coefficients o_1, o_2, s_1, and s_2.

The time fraction f can be approximated by using Eq. (4.5). To calculate the other unknowns, one can enforce the transition conditions in Eq. (4.8). For this system, however, the mode shapes $\mathbf{\Phi}_o$ and $\mathbf{\Phi}_s$ are not necessary because this is a single-DOF system.

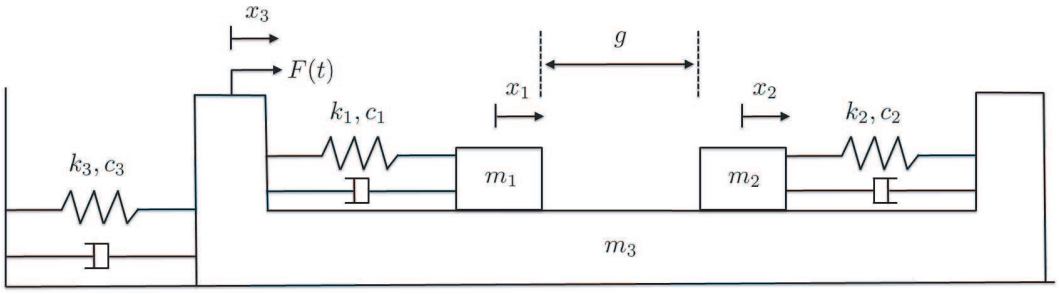

Figure 4.7: Three-DOF system

Therefore, the transition conditions are expressed as

$$\begin{aligned} x_s(T_s+\alpha) &= 0, \\ x_o(T_s+\alpha) &= 0, \\ x_s(\alpha) &= 0, \\ x_o(T_o+T_s+\alpha) &= 0, \\ \dot{x}_s(T_s+\alpha) &= \dot{x}_o(T_s+\alpha), \\ \dot{x}_s(\alpha) &= \dot{x}_o(T_o+T_s+\alpha). \end{aligned} \tag{4.10}$$

Using Eq. (4.5), f can be approximated as 0.4772. Eq. (4.10) is solved using a methodology similar to that described for solving Eq. (4.8). One obtains α and the corresponding four coefficients to minimize the residual. Then, the amplitude of the steady-state vibration can be calculated as 0.218 m (Fig. 4.6). This value has an excellent relative error of 0.79% compared to the exact amplitude of 0.2163 m.

4.3.2 Three-Degree-of-Freedom System

The damped three-DOF system used is shown in Fig. 4.7, where $m_1 = 2.0$ kg, $m_2 = 2.0$ kg, and $m_3 = 10.0$ kg; $k_1 = 1.6$ N/m, $k_2 = 1.68$ N/m, and $k_3 = 8.0$ N/m; $c_1 = 0.08$ kg/s, $c_2 = 0.084$ kg/s, and $c_3 = 0.4$ kg/s. The initial gap g is zero. The mass m_3

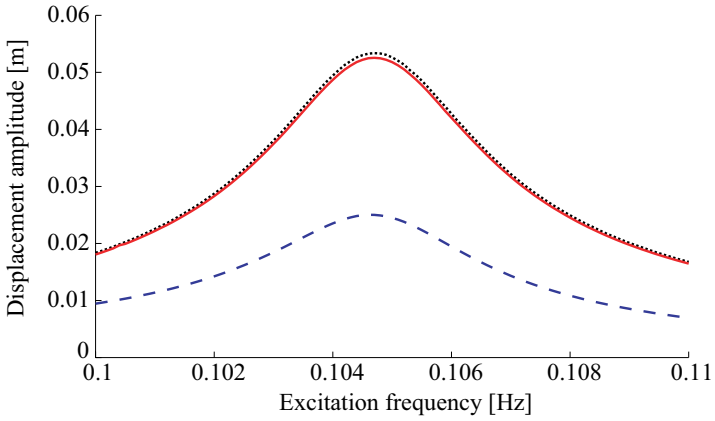

Figure 4.8: Amplitudes of the nonlinear motions: m_1 ($\cdots$), m_2 (—), and m_3 (– – –)

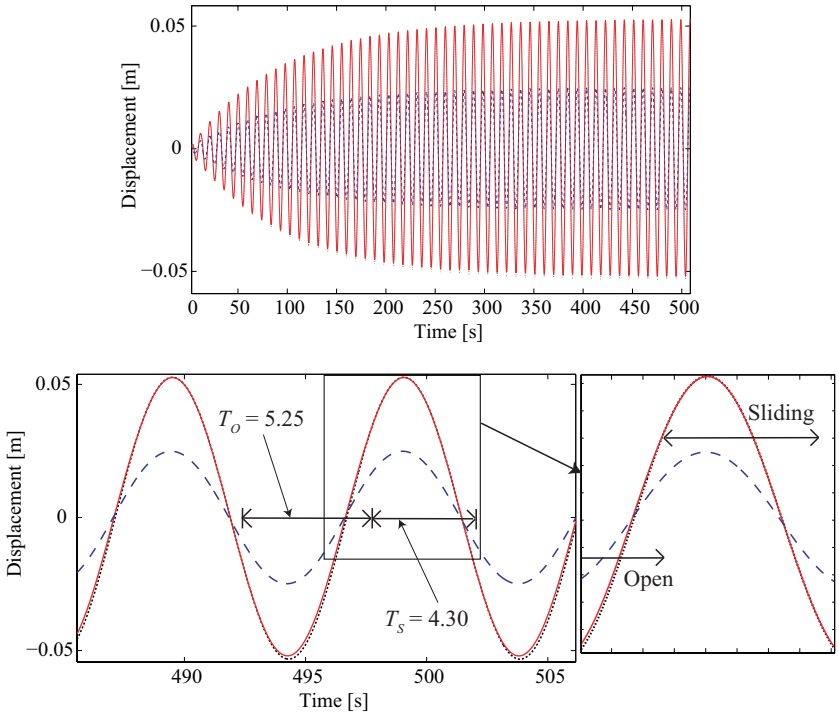

Figure 4.9: Displacement vs. time for a forcing at the resonant frequency of $\omega = 0.1047$ Hz: m_1 ($\cdots$), m_2 (—), and m_3 (– – –)

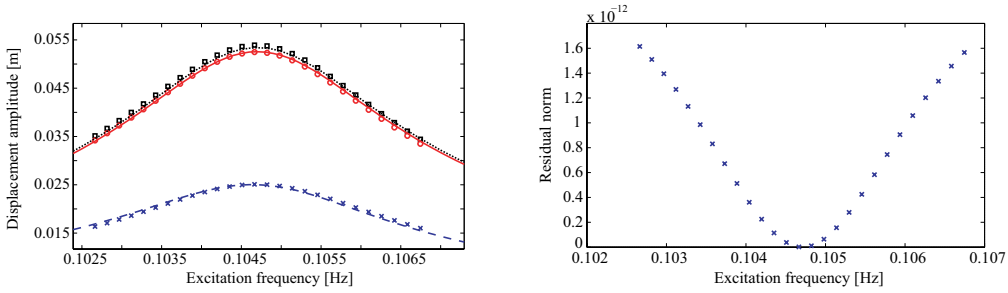

(a) (b)

Figure 4.10: (a) Amplitudes predicted by BAA for m_1 (□), m_2 (○), and m_3 (×) versus the amplitudes calculated by direct numerical integration for m_1 ($\cdots$), m_2 (—), and m_3 (– – –), and (b) the residual obtained when solving for the unknown coefficients in BAA for the three-DOF system

is excited by a harmonic force $F(t)$ of magnitude 0.01 N. It is assumed that there is no friction between the masses and ground.

The resonant frequencies of the system were found by integrating in time the exact nonlinear equations of motion. A plot of the amplitude of the response versus excitation frequency for the three masses is plotted in Fig. 4.8. The steady-state response at the resonant frequency of $\omega = 0.1047$ Hz is shown in Fig. 4.9. Also, Fig. 4.9 shows $T_o = 5.25$ s and $T_s = 4.30$ s. The total period T is given by $T = \frac{2\pi}{\omega}$. The exact time fraction f_e obtained is $f_e = \frac{T_s}{T} = 0.450$. The amplitude of motion of the masses are 0.05337 m for m_1, 0.05255 m for m_2, and 0.02501 m for m_3, as shown in Fig. 4.9.

The exact equations of motion for state (1) and state (2) can be described using Eq. (4.1). Furthermore, it is assumed that the motion in state (1) and state (2) can be approximated well by a single overlapping mode $\mathbf{\Phi}$. The modal coordinates q_o and q_s are expressed using Eq. (4.4).

The time fraction f can be approximated by using Eq. (4.5). To calculate the other unknowns, one can enforce the transition conditions stated in Eq. (4.8) with $i = 1$ and

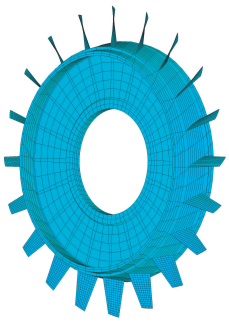

Figure 4.11: Bladed disk model

$j = 1$.

Using Eq. (4.5), f was approximated as 0.4999. By enforcing the transition conditions and calculating the residual, one can find α and the corresponding four coefficients o_1, o_2, s_1, and s_2. Next, the amplitudes of the steady-state vibration were calculated as 0.05393 m for m_1, 0.05247 m for m_2, and 0.02509 m for m_3 as shown in Fig. 4.10. The relative errors of these results compared to the exact amplitudes are excellent, namely 1.05% (m_1), 0.15% (m_2), and 0.32% (m_3).

4.3.3 Full Bladed Disk

The blisk model [101] used in this work is the tuned bladed disk shown in Fig. 4.11. The blisk has 20 blades, one of which has a crack. The crack length is 37.5% of the chord on the leading edge at 50% span from the root of the blade. The material of the bladed disk is a Titanium alloy with Young's modulus $E = 114\,\mathrm{GPa}$, density $\rho = 4,420\,\mathrm{kg/m^3}$, and Poisson's ratio $\nu = 0.31$. The full order model has $31,878$ DOFs. The damping is modeled as Rayleigh damping (without mass matrix contribution), $\mathbf{C} = \beta\mathbf{K}$, where β is a scalar (with a constant value in each frequency range of interest) corresponding to a

Mode family	Nonlinear amplitdue (mm)	BAA amplitude (mm)	Error (%)	# of open modes for BAA	# of sliding modes for BAA
1^{st}	8.032	7.955	0.959	1	8
2^{nd}	1.257	1.323	5.25	1	1
7^{th}	0.1869	0.1931	3.32	1	1
10^{th}	4.834×10^{-3}	4.702×10^{-3}	2.73	2	1

Table 4.1: Summary of BAA results for the full bladed disk with engine order excitation 0

viscous damping ratio value of $\zeta = 0.001$. The commercial software ANSYS was used to obtain the mass and stiffness matrices.

BAA utilizes mode shapes of both the open and sliding states of the full bladed disk to obtain the overlapping space $\mathbf{\Phi}$ in which the energy and momentum of the system are transferred between the open and sliding states. The linear (open and sliding) mode shapes which dominate the motion in the frequency range of interest are computed using the mass and stiffness matrices of the system. These modes are used to compute the overlapping space. Figure 4.12 shows the steady state displacement amplitude at the excited node for the cracked blade using open and sliding modes of the full bladed disk over the frequency range of interest. The force applied is an engine order 0 excitation to one node along each blade with an amplitude of 1 kN over frequency ranges that excite the 1^{st}, 2^{nd}, 7^{th}, and 10^{th} mode families (one at a time). To select the dominant open and sliding modes $\mathbf{\Phi}_o$ and $\mathbf{\Phi}_s$ used to compute the overlapping space $\mathbf{\Phi}$, one selects modes $\mathbf{\Phi}_{\max}$ which result in the largest amplitude for the excited node (on the cracked blade) as well as all other modes that respond at the frequencies of the modes in $\mathbf{\Phi}_{\max}$ and near the bilinear resonant frequency of the system. Recall that the bilinear resonant frequency ω_{BFA} can be calculated using BFA. The overlapping space $\mathbf{\Phi}$ can then be calculated using an SVD for the selected open and sliding modes $\mathbf{\Phi}_o$ and $\mathbf{\Phi}_s$. Also, the transition relations in Eq. (4.8) can be enforced at just a few selected physical locations on each blade.

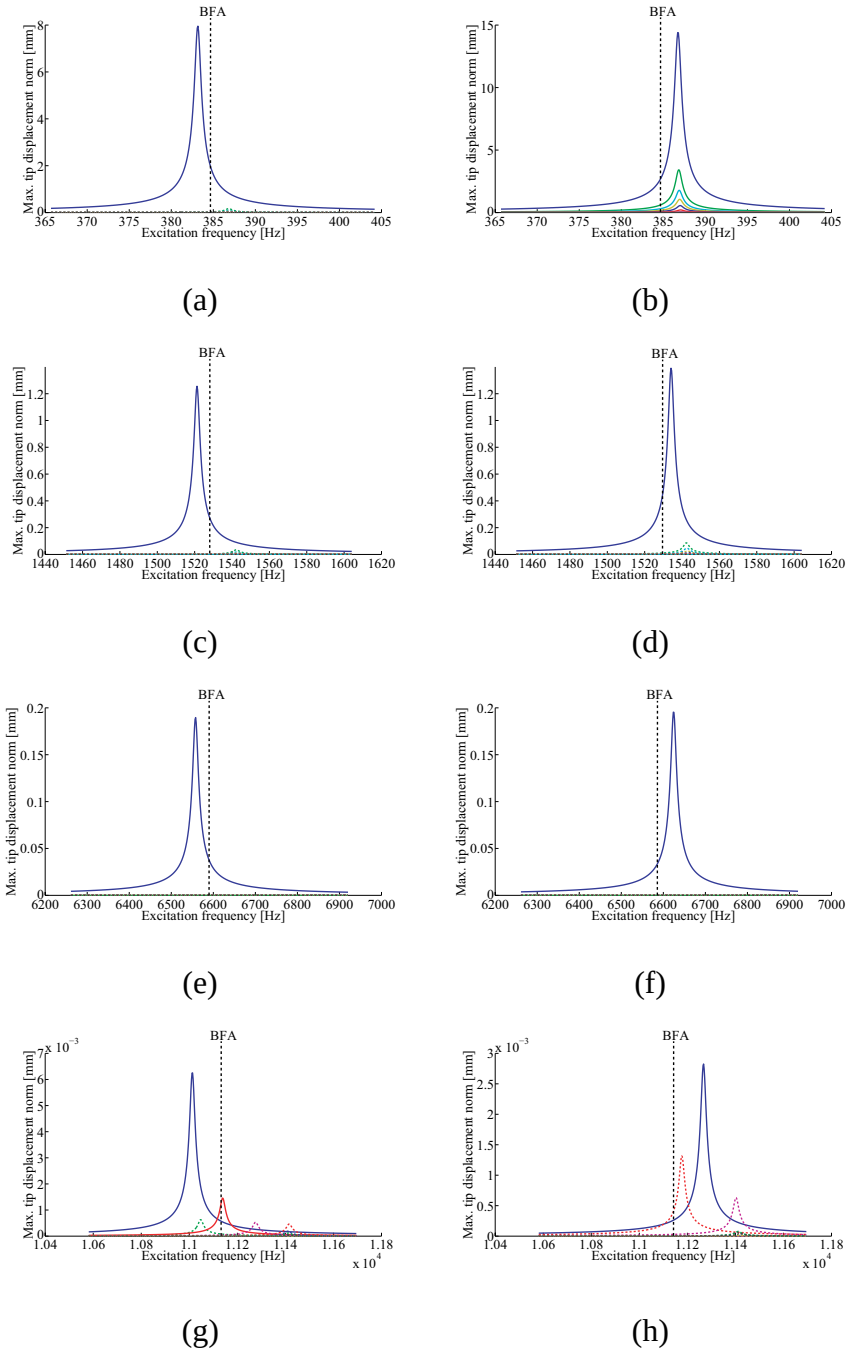

Figure 4.12: Steady state displacement amplitudes at the excited node for the cracked blade using open and sliding modes of the full bladed disk with engine order excitation 0: (a) open modes for the 1^{st} mode family, (b) sliding modes for the 1^{st} mode family, (c) open modes for the 2^{nd} mode family, (d) sliding modes for the 2^{nd} mode family, (e) open modes for the 7^{th} mode family, (f) sliding modes for the 7^{th} mode family, (g) open modes for the 10^{th} mode family, (h) sliding modes for the 10^{th} mode family

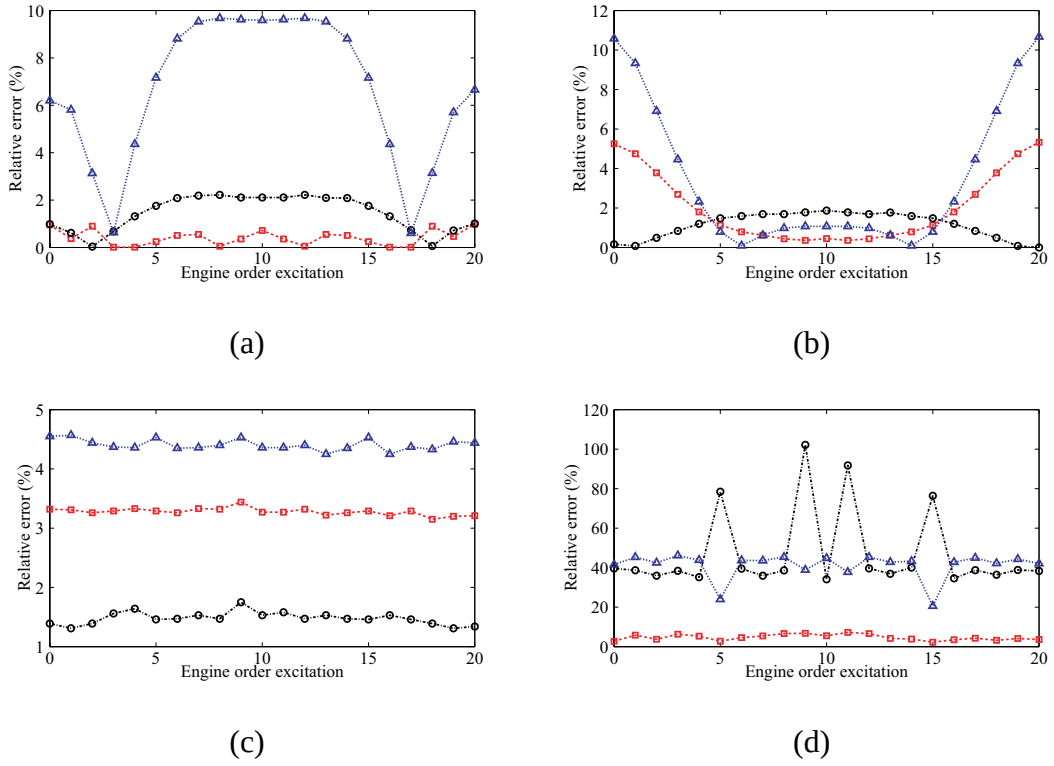

Figure 4.13: Relative errors of amplitudes predicted using BAA (□), open modes only (○), and sliding modes only (△) when compared to the nonlinear forced responses for various engine order excitations: (a) 1^{st} mode family, (b) 2^{nd} mode family, (c) 7^{th} mode family, (d) 10^{th} mode family

The vibration amplitude of the full bladed disk system with piecewise-linear nonlinearity was calculated using an in-house code based on a hybrid frequency/time (HFT) domain solver [39, 45, 46, 54, 101]. The results of calculating the nonlinear responses for the 1^{st}, 2^{nd}, 7^{th}, and 10^{th} mode families are summarized in Tab. 4.1 for engine order 0 excitation. Also, the amplitudes predicted by BAA as well as the number of open and sliding modes used in the BAA analysis are summarized in Tab. 4.1. The modes that were used for BAA are indicated as the solid lines in Fig. 4.12. The agreement between BAA and the nonlinear calculation is quite good.

BAA was also applied to approximate the nonlinear resonant amplitudes of the full

bladed disk at the other engine order excitations. To select the open and sliding modes used for computing the overlapping space $\mathbf{\Phi}$, the steady state displacement amplitude at the excited node for the cracked blade using the open and sliding modes of the full bladed disk was investigated by generating plots similar to those shown in Fig. 4.12. To show the accuracy of BAA, the relative errors of BAA compared to the nonlinear forced responses are presented in Fig. 4.13 along with the relative errors of the open amplitudes and the sliding amplitudes. For the 1^{st} mode family, BAA is more accurate than the open and sliding amplitudes for most engine order excitations. Also the open amplitudes tend to be more accurate than the sliding amplitudes. For the 2^{nd} mode family, there are regions where the BAA is best, open is best and sliding is best. For the 7^{th} mode family, open amplitudes are most accurate for all engine order excitations and BAA tend to be more accurate than the sliding amplitudes. For the 10^{th} mode family, BAA is most accurate for all engine order excitations. The key observation taken away from these results is that BAA is always the most accurate or between the accuracy of the open and sliding results. Since in general one will not know whether the open or sliding results are more accurate, there is a substantial improvement in using BAA if one wishes to use a fast linear approach to estimate the nonlinear resonant amplitudes. Therefore, BAA can provide approximated amplitudes of nonlinear resonant amplitudes with good accuracy for the full bladed disk. Also, the computational time required by BAA is approximately 100 times shorter than the time needed for the full-order nonlinear calculations.

4.4 Conclusions and Discussion

An efficient and novel methodology to approximate the steady-state amplitude of vibration of a system with piecewise-linear nonlinearity was developed. This method is referred to as bilinear amplitude approximation (BAA). BAA requires only a few linear

calculations to compute the mode shapes of the system when the system is in its open state and sliding state. Then, an overlapping space that is spanned by selected mode shapes are obtained by SVD. Next, a very low-dimensional nonlinear least square problem is solved to calculate unknowns to construct the approximated periodic vibration cycle of the system, and the BAA amplitude is calculated. BAA does not require numerical integration to calculate the nonlinear amplitude at resonant frequencies. Therefore BAA can drastically reduce the computational costs required in obtaining the nonlinear resonant amplitude. The method divides each cycle of the steady-state nonlinear response into two parts. The first portion of the response corresponds to the open case (if there is a crack that would mean that the crack is open). The second portion of the response corresponds to the sliding case (if there is a crack that would mean the crack is closed). The transition between each state is assumed to take place quickly. The method then enforces transitional compatibility at the contacting surfaces, namely that physical displacement and velocities are compatible when the system transitions from the open to sliding states and vice versa. The BAA method was demonstrated for a single-DOF system and a three-DOF system. The results were compared against the exact solutions, and good agreement was found. The method was also demonstrated on a full bladed disk model with a crack and found to obtain accurate results compared to a full-order nonlinear analysis.

CHAPTER V

Nonlinear Reduced-Order Models for the Structural Dynamics of Combustor Systems with Pre-Stress and Friction

5.1 Introduction

Life assessment has many benefits in industry. For example, life assessment for combustors can be utilized to determine periods of maintenance, which in turn leads to cost savings by avoiding unnecessary maintenance. For conducting life assessment one must consider several factors with one of the most critical being wear. The significance of wear is addressed using the value for total wear damage [103]. Combustor systems often experience wear at the interfaces between components due to flow-induced vibration. These vibrations can lead to sliding motions at the interfaces, which result in wear. To extend the life of combustor systems, there have been many efforts to reduce vibrations by optimal design and by controlling the dynamics of the system [104]. Using system dynamic modeling and experiments, it was verified [104] that the amount of wear at the interfaces can be reduced by decreasing the vibrations in the system. In practice, wear has been observed at interfaces between the transition piece and the hula seal, and between the hula seal and the liner. These interfaces are pre-stressed when the components are assembled. It was observed that the resulting vibratory response has a softening nonlinearity. It is

strongly believed that this nonlinear vibration can significantly affect the wear of the combustor system, therefore it is important to identify the physical reason for the nonlinearity. Possible causes for the nonlinearity include sliding contact with Coulomb friction at the interfaces, loss of contact (opening and closing of the gap at the interfaces), and buckling of the hula seal or nonlinearity in the hula seal. From a preliminary study, it was found that sliding contact with Coulomb friction at the interfaces causes the nonlinearity.

To model frictional contact in dynamic structures, several contact models have been developed [105–109]. These contact models are associated with contact parameters such as contact stiffness (tangential and normal) and the friction coefficient. Differentiations in the contact models relate to 1) whether the normal load is variable, and 2) the dimension of the model (i.e., one dimensional, two dimensional). A stick-slip condition for a contact model is determined by comparing the elastic force in tangential stiffness and the friction force. Therefore if the contacting areas at the interfaces of dynamic structures are modeled using multiple contact elements, a scenario can occur where the contact elements do not simultaneously enter the slip condition from the stick condition since the stick-slip condition is separately determined for each contact element by comparing the elastic force and the friction force. This scenarios is referred to as micro-slip [110–113], which differs from macro-slip (or gross-slip) where all contact elements simultaneously enter the slip condition from the stick condition. In detail, the micro-slip is defined as: “small relative tangential displacement in a contacting area at an interface, when the remainder of the interface in the contacting area is not relatively displaced tangentially” [114]. This micro-slip can affect resonant vibrations (amplitudes and frequencies) of dynamic systems, therefore it is necessary to consider micro-slip at contacting areas for accurately predicting system dynamics.

Finite element (FE) analysis is often employed to study the vibration of structures.

If a system is small and its geometry is simple, then the system can be modeled using a low dimensional FE model. For this low dimensional model, a full order analysis can be conducted. However, for large and complex structures such as turbine bladed disks, the system must be modeled using a high dimensional FE model for accurate analysis. For these systems, the computational cost required in analyzing full FE models can often be prohibitive. In order to overcome this difficulty, many investigators have developed reduced-order models (ROMs) for various systems [1, 13, 14, 30, 32, 39, 40, 45, 54, 101]. Structures that contain frictional contacts between contacting bodies can also be modeled using FE analysis. Frictional contacts can be modeled using contact elements provided in commercial FE software such as ANSYS. In order to calculate the forced responses of the structures with frictional contacts, a time marching for the full-order FE model including the contact elements should be employed. However this approach is often prohibitive due to the considerable computational cost. To reduce the computational cost, the harmonic balance method (HBM) can be used to obtain the steady state nonlinear forced response of structures with frictional contacts [107, 115]. The HBM has been utilized to calculate the steady-state nonlinear forced response of complex and large FE models with frictional contacts such as turbine bladed disks with a friction damper [116], but the computational cost is still formidable due to the large size of the governing equations (even when model reduction is used) and the required iterative calculation to obtain the converged solution. To resolve this issue, efficient ROMs that are specifically designed to capture the effects of Coulomb friction with micro-slip are developed. These ROMs have relatively small dimension (i.e., one or two), therefore they drastically reduce the computational cost required to obtain the nonlinear forced response of the system with frictional contacts.

This paper is organized in the following manner. First, it is shown that nonlinear responses observed in the combustor system are due to the Coulomb friction at the inter-

faces. An FE model representing a simplified hula seal and two rigid plates (which relate to the transition piece and the liner) is created in ANSYS. In this FE model, contact elements [106] are used to model the interface between the plates and the hula seal. Transient dynamic analysis (TDA) in ANSYS is performed with the full-order model to verify the softening nonlinearity and micro-slip at all levels of pre-stress. Then, an efficient ROM to analyze the vibration of the hula seal model is developed. To show that ROMs for this model are possible, proper orthogonal decomposition (POD) is used to verify that the dynamics of the system is dominated by a low number (i.e., one or two) of spatial coherences. For a variety of frequency ranges and pre-stress levels, it is shown that a single such coherence is dominant. Next, low order ROMs are proposed and their parameters are identified using a systematic method. Then, the ROMs developed are validated by comparing their predictions with results from TDA using the full-order model. It is shown that these ROMs can accurately predict the nonlinear response of the system while achieving considerable saving in computational costs. After developing ROMs for a simplified hula seal model, an extended hula seal model is introduced. This model is composed of a simplified hula seal and two long rigid plates where axial directional dimensions are similar to a realistic transient piece and liner. Efficient ROMs are developed for this model and they are validated using results of TDA obtained with a full-order FE model. Finally, conclusions are presented.

5.2 Methodology

In this section, a contact model used for modeling the interface between the transition piece and the hula seal, and the interface between the hula seal and the liner is presented. Then, a POD based method to find the spatial coherences in hula seal models is introduced. Finally, a procedure to develop ROMs utilizing the spatial coherences is explained with a

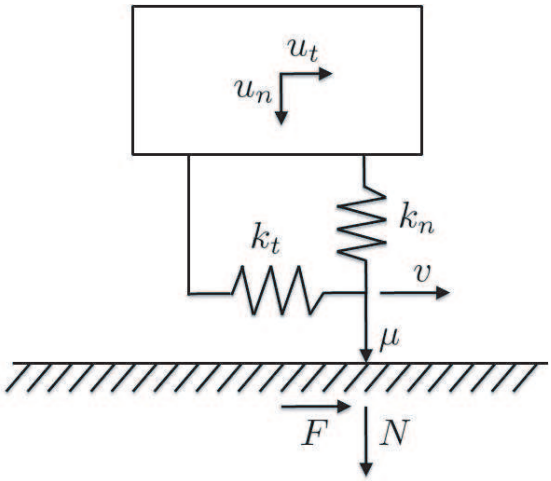

Figure 5.1: Contact model

systematic way to identify the parameters required to construct the ROMs.

5.2.1 Contact Model

Contacts between the components (the hula seal and the plates) are modeled using the contact elements [106,116] shown in Fig. 5.1. This contact element contains both a normal stiffness k_n and a tangential stiffness k_t. Also, the element models a varying normal load N which arises from the normal relative motion u_n. If the element experiences a large relative motion in the normal direction, (intermittent) separation of the contact surfaces can occur. The pre-stress or initial gap can be described using the initial distance between the two contacting bodies. There are three possible states that contact elements can have, which are stick, sliding, and separation. The contact force F changes based on the contact states. When the contact is in the stick state, sliding motion v does not exist and $F = k_t u_t$. When it is in the sliding state, $F = \mu N$ where μ is friction coefficient and $N = k_n u_n$. If it is in the separation state, $F = 0$. The criteria for the transition between states is determined by the contact forces (i.e., elastic force in stiffnesses and friction force) [116].

For example, when the system is in the stick condition, the contact force F can increase due to the relative tangential motion u_t. If the contact force F is greater than the maximum friction force μN, the contact starts to slide.

5.2.2 Proper Orthogonal Decomposition

To investigate spatial coherences of the hula seal model, proper orthogonal decomposition (POD) is employed [117]. If the dynamics of the model is dominated by a low number of spatial coherences, developing efficient ROMs may be possible. POD requires measured data of the system dynamics such as displacement. If the system dynamics is measured at M locations and the displacement is sampled N times at each location, then one can form displacement history arrays at each location, such that $\mathbf{x}_i = (x_i(t_1), x_i(t_2), ..., x_i(t_N))^{\mathrm{T}}$ for $i = 1, ..., M$. The mean of each displacement arrays is typically subtracted from each displacement history. POD utilizes these displacement histories to form an $N \times M$ ensemble matrix $\mathbf{X}$,

$$\mathbf{X} = [\mathbf{x}_1, \mathbf{x}_2, ..., \mathbf{x}_M]. \tag{5.1}$$

Next, the correlation matrix $\mathbf{R} = \mathbf{X}^{\mathrm{T}}\mathbf{X}$ that has a size of $M \times M$ is constructed. Then, eigenvectors and eigenvalues of $\mathbf{R}$ are computed. The eigenvectors are called proper orthogonal modes (POMs) and the eigenvalues are called proper orthogonal values (POVs). Dominant POMs are determined based on POVs. Namely, POMs corresponding to relatively large POVs are considered dominant modes. In this work, physical displacement data obtained from TDA is used instead of measured displacement data. The procedure to perform TDA is as follows. First, a pre-stress is applied by quasi-statically loading a pre-displacement on the transition piece plate. Next, a distributed harmonic force is applied to the transition piece plate with the pre-load associated with a pre-displacement. Then, the time series of steady state responses for all degrees of freedom (DOFs) (in x, y, and

z direction) of the hula seal model are collected. The mean displacements are subtracted from the displacement histories for each DOF, and the correlation matrix $\mathbf{R}$ is constructed. Then, eigenvectors and eigenvalues of the matrix $\mathbf{R}$ are computed and the dominant POMs are determined based on the POVs. If the number of dominant POMs is low (i.e., one or two), then the dynamics of the model is dominated by a low number of spatial coherences.

5.2.3 Reduced Order Modeling

For efficient vibration analysis of combustor systems it is necessary to develop ROMs. The procedure to construct ROMs starts from developing efficient ROMs for the hula seal since nonlinear vibrations caused by Coulomb friction in the hula seal significantly affect the vibration of the systems. Hence, the focus is placed on developing ROMs for the hula seal first. These ROMs will be validated by comparing their predictions with results obtained from the full-order model (TDA in ANSYS).

The equations of motion for a hula seal FE model can be described in matrix form as

$$\mathbf{M}\ddot{\mathbf{x}}(t) + \mathbf{C}\dot{\mathbf{x}}(t) + \mathbf{K}\mathbf{x}(t) + \mathbf{F}_f(\mathbf{x}, \dot{\mathbf{x}}) = \mathbf{F}(t), \tag{5.2}$$

where m is the total number of DOFs in the model, $\mathbf{x} \in \mathbb{R}^m$ is a vector of nodal displacements, $\mathbf{M}$, $\mathbf{C}$, $\mathbf{K} \in \mathbb{R}^{m \times m}$ are mass, damping, and stiffness matrices, $\mathbf{F} \in \mathbb{R}^m$ is the external force vector, and $\mathbf{F}_f \in \mathbb{R}^m$ is the nonlinear force vector caused by Coulomb friction. The nonlinear force $\mathbf{F}_f$ is determined based on the state of the contact elements (i.e., stick, sliding, or separation). If it is assumed that the dynamics of the system is dominated by a low number of spatial coherences, for example a single spatial coherence, Eq. (5.2) can be transformed into Eq. (5.3) using the modal transformation $\mathbf{x} = \mathbf{\Phi} q$ where $\mathbf{\Phi}$ is the dominant POM obtained by POD.

$$\ddot{q}(t) + c\dot{q}(t) + kq(t) + f_f(q, \dot{q}) = f(t), \tag{5.3}$$

where q is the modal coordinate satisfying $\mathbf{x} = \mathbf{\Phi} q$. The nonlinear force f_f can be described as

$$\begin{aligned} f_f &= g\,\mathrm{sgn}(\dot{q}), \ \text{when the contact element is in the sliding state} \\ f_f &= k_t(q - q_c), \ \text{when the contact element is in the stick state,} \end{aligned} \tag{5.4}$$

where g represents the friction force, k_t represents the tangential stiffness in the contact element and q_c refers to a position in which the contact element experiences sticking. The elastic force due to the tangential stiffness is computed using the relative displacement of q and q_c. Contact parameters k, g, and k_t can be identified by a systematic method using static analysis.

Parameter Identification

In this work, the parameters k, g, and k_t representing the stiffness of the hula seal, the friction force and the tangential stiffness of contact element are investigated using quasi-static analysis. The analysis is conducted for the hula seal FE model, which is composed of a simplified hula seal and two plates. First, pre-displacement (meaning pre-stress) y_o in the vertical direction is applied on top of the transition piece plate without friction. One can consider the state of the system after applying the pre-displacement as the pre-stressed equilibrium position of the system. Next, friction is turned on and additional vertical displacement δy is applied on top of the transition piece plate. Reaction forces generated due to the additional displacement are collected at contact nodes or nodes on top of the transition piece plate. Finally, the summation of the reaction forces δP are calculated. One can repeat this procedure by increasing and decreasing δy. By doing that, one can obtain a hysteresis loop. In this loop, there exist four regions that describe forward sliding, backward sliding, and two sticking regions as shown in Fig. 5.2. In the sliding regions, one can identify the stiffness of the hula seal k using the slope of the region. Also, g is

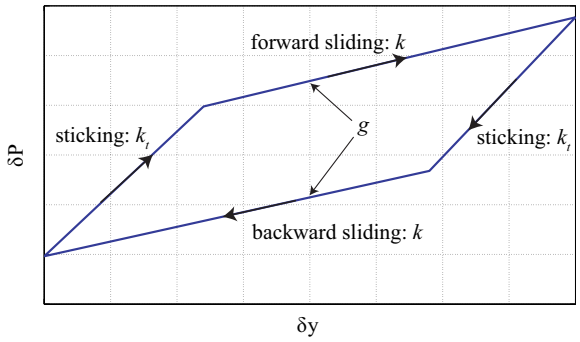

Figure 5.2: Sample of hysteresis loop

calculated using two intercept values with the δP axis in the sliding regions. Parameter k_t is obtained using the slope in the sticking regions. After identifying the contact parameters, one can construct the ROM.

5.3 Results

In this section, a softening nonlinearity is observed at the interfaces of the combustor system and is verified for a simplified hula seal FE model using TDA in ANSYS. TDA is applied using the full-order model to obtain steady state responses of the system. Next, parameter identification required for constructing ROMs of the hula seal model is addressed. Then, ROMs are developed using these parameters. ROMs are validated by comparing their results with TDA results. After developing ROMs for a simplified hula seal model, another (more realistic) hula seal model is introduced. This model has a hula seal and two long plates which relate to the transition piece and liner. The lengths of the two plates are obtained from the original axial directional dimensions of the transition piece and liner. In this paper, this model is referred to as the extended hula seal model. A ROM for analyzing the vibration of the extended hula seal model is developed using the parameters identified

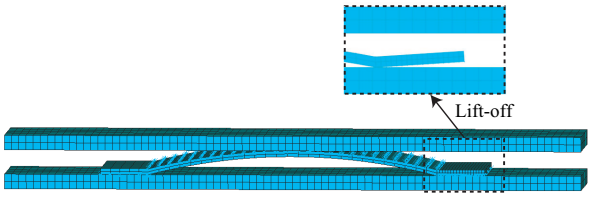

Figure 5.3: Simplified hula seal model

for a simplified hula seal model. The results calculated using this ROM are compared to those of TDA for the full-order FE model.

5.3.1 FE Model

The hula seal and the two rigid plates are modeled in ANSYS using solid brick elements (SOLID185) as shown in Fig. 5.3. The full-order model has $14,256$ DOFs. One of the plates (the upper plate) is placed on top of the hula seal and represents the transition piece. The other plate (the lower plate) is placed under the hula seal and represents the liner. Actual dimensions of a hula seal were used. The upper plate has contact with the top area of the hula seal. The lower plate is in contact with the hula seal in two regions. Contact elements CONTA175 were used to model the contact between the plates and the hula seal. The node-to-surface contact option was chosen with the augmented Lagrange method [118](ANSYS default). The fixed foot of the hula seal was bonded to the lower plate. The contact between the sliding foot of the hula seal and the lower plate does not allow penetration (but it does allow separation). The contact between the hula seal and upper plate is also set up to not allow penetration but to allow separation. The key controllable parameter for the contact element in terms of (maximum allowable) elastic slip is the tangential stiffness which is determined by 1) maximum allowable sliding distance (denoted by SLTO in ANSYS), tangential stiffness factor (denoted by FKT in ANSYS),

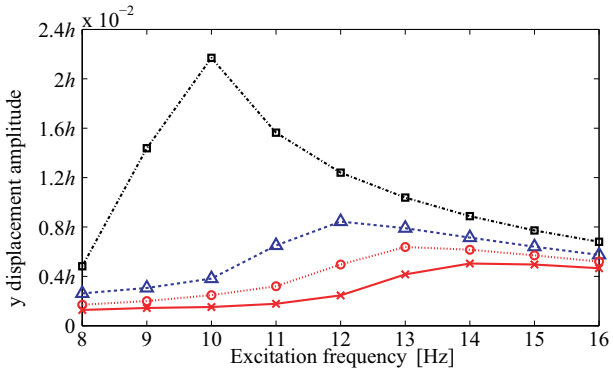

Figure 5.4: Softening nonlinearity observed in the hula seal model with pre-displacement of y_o = 32.8% of h and various forcing amplitudes: $F = 8$ lbf (□), $F = 6$ lbf (△), $F = 5$ lbf (○), and $F = 2$ lbf (×)

coefficient of friction (denoted by μ in ANSYS), and normal pressure (denoted by PRES in ANSYS). It was found that each contact element can start to slide separately since the normal pressure at each contact element can be different, which changes the maximum friction force. This explains how micro-slip occurs in contact elements. Actual material properties of a hula seal were used. The plates are modeled using a large Young's modulus ($1,000$ times larger compared to that of the hula seal) so that they behave almost as rigid bodies. The upper plate is constrained to move in the vertical direction only. The lower plate is constrained in all directions. The coefficient of friction μ is set to 0.15. The ratio of the dynamic and static friction coefficient was set to 1.

5.3.2 Softening Nonlinearity

TDA was applied to the full-order FE model of the hula seal and two plates. Pre-stress can be applied either as a force or as a displacement. For best convergence, displacement is preferred. Thus, a pre-displacement in the y direction was quasi-statically applied to the upper plate. After that, a distributed harmonic force was applied with the static load and a full transient analysis was performed (i.e., inertia effects were considered). This procedure

was repeated for various pre-stress levels, and various harmonic excitation amplitudes. It was observed that the sliding foot of the hula seal experiences lift-off due to the pre-load as shown in Fig. 5.3. The model and simulation conditions are not those of an actual GE product or process, and were introduced solely for the academic purpose of verifying the proposed reduced-order formulation. It was also found that the normal force acting on the sliding foot of the hula seal was only about 20% of the pre-load. The results obtained from TDA with various levels of forcing amplitude and pre-load showed a softening nonlinearity in terms of y displacement amplitude of the hula seal. The results of TDA with various levels of forcing amplitude and pre-displacement y_o = 32.8% of h is shown in Fig. 5.4, where h is the vertical size (height) of the hula seal.

5.3.3 Validation of Reduced Order Models Developed for a Simplified Hula Seal Model

A method based on POD was used to demonstrate that the dynamics of the full-order hula seal model is low dimensional. TDA was applied to the full-order model with pre-displacement y_o = 32.8% of h and harmonic force amplitude of 2 lbf. Time series of physical displacements for all DOFs in x, y, and z directions for the hula seal and in the y direction for the upper plate were collected from the responses obtained from TDA in ANSYS for the frequency range of interest. Then, the matrix $\mathbf{R}$ of sample displacement data in steady state were constructed. Here, the means of displacements were subtracted from the displacement histories for each DOF. Using this matrix $\mathbf{R}$, POVs and POMs in physical coordinates were computed. It was found that one POV was much larger than the other POVs (100 times larger compared to the second largest POV, and $100,000$ times larger compared to the third largest POV). Therefore, it was concluded that the hula seal model has a single dominant spatial coherence (of sliding motion), which means it has a single dominant POM. This POD method was applied for other pre-stress levels (y_o =

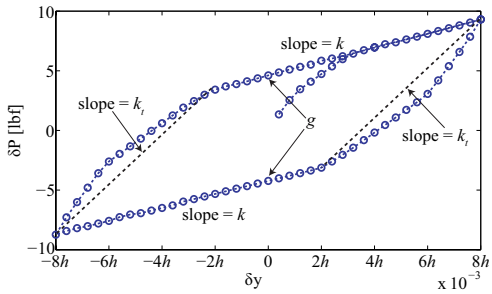

Figure 5.5: Hysteresis loop of the hula seal model obtained for pre-displacement y_o = 23.2% of h

23.2% of h, y_o = 25.6% of h , and y_o = 30.4% of h) and force amplitude levels ($F = 3$ lbf and $F = 8$ lbf). It was found that the model has single dominant spatial coherence also.

If a single dominant POM was used to construct the ROMs, the equation of motion of the system is described by Eq. (5.3) and parameters k, g, and k_t are required. To obtain the parameters, a systematic method using a hysteresis loop was utilized. A hysteresis loop is obtained using static analysis for the hula seal model. A pre-displacement of y_o = 23.2% of h in the vertical direction is applied to the top of the transition piece plate using no friction. Next, friction is turned on and an additional vertical displacement δy is applied to the top of the transition piece plate. Reaction forces generated due to additional displacement δy are measured at contact nodes (or nodes on top of the transition piece plate). The summation of the reaction forces δP are calculated. This procedure is repeated as δy increases and decreases. Finally a hysteresis loop which plots δP versus δy was obtained as shown in Fig. 5.5. In this figure, there exist four regions that describe forward sliding, backward sliding, and two sticking states. In the sliding regions, k representing the stiffness of the hula seal was obtained using the slopes of sliding regions. Also, g was calculated using the intercepts with the δP axis in sliding regions. Parameter k_t is obtained using the approximated slope in the sticking regions. Similarly, ROM parameters k, g, and k_t for

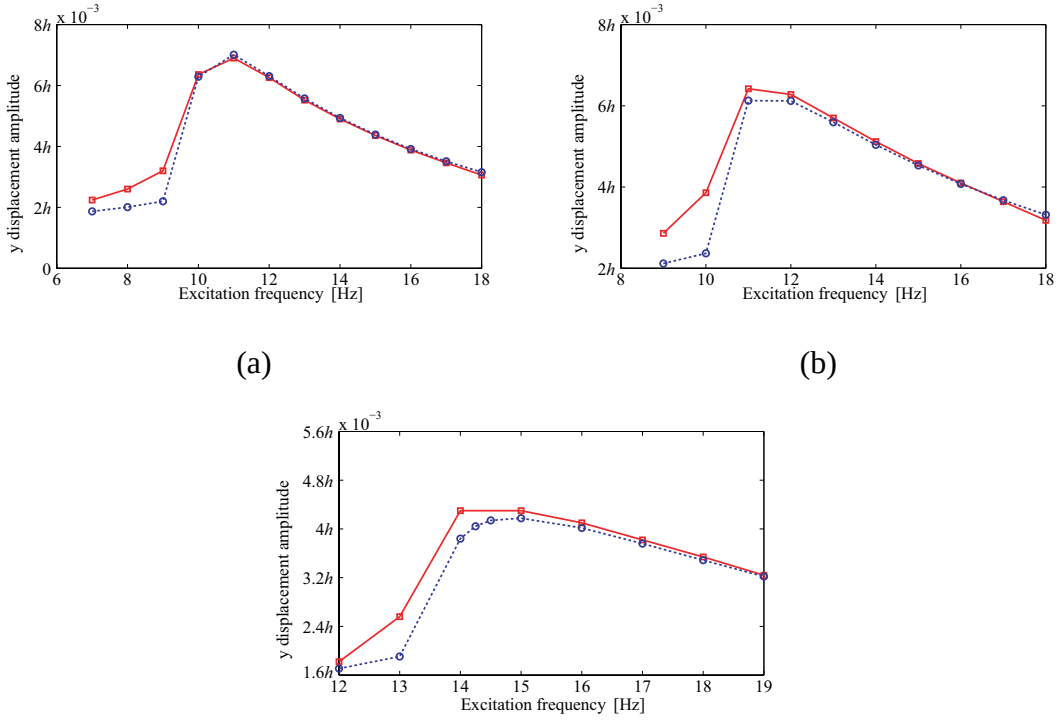

Figure 5.6: Validation of ROMs (○) developed for a simplified hula seal using TDA results (□) obtained for pre-displacement: (a) y_o = 23.2% of h, (b) y_o = 25.6% of h and (c) y_o = 30.4% of h

other pre-displacements (y_o = 25.6% of h, and y_o = 30.4% of h) were calculated using these hysteresis loops. After identifying these parameters, ROMs were developed for the hula seal model with various levels of pre-displacement (y_o = 23.2% of h, y_o = 25.6% of h, and y_o = 30.4% of h). Here, it should be noted that the ROMs change with the level of pre-stress since the contact parameters vary based on pre-stress.

To validate the ROMs, TDA was applied to the full-order model with a variety of pre-displacement (y_o = 23.2% of h, y_o = 25.6% of h, and y_o = 30.4% of h) and a harmonic force amplitude of 4 lbf. The displacement amplitudes of the transient piece plate in the y direction are compared. As shown in Fig. 5.6, it is found that the ROM accurately predicts the results of TDA for various levels of pre-stress. Also, it was observed that the

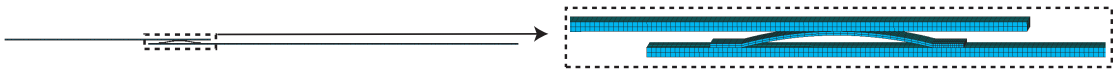

(a) (b)

Figure 5.7: Extended hula seal model: (a) overview and (b) close-up

resonant frequency shifts to a higher frequency and the vibration amplitudes decrease as pre-displacement increases.

5.3.4 Reduced Order Model for a Extended Hula Seal Model

After validating the ROM for the simplified hula seal model, a realistic extended hula seal model is introduced, which is shown in Fig. 5.7. This extended hula seal model has a hula seal and two long plates which relate to the transition piece (upper plate) and the liner (lower plate). The hula seal itself is the same as the one used in the simplified hula seal model. The full order model has $51,237$ DOFs. The length of the two plates in the axial direction was not determined from a real transition piece and liner. The plates are modeled using a large Young's modulus ($1,000$ times larger compared to that of the hula seal) so that they behave like rigid bodies. The coefficient of friction μ is set to 0.15. The ratio of dynamic and static friction coefficients is set to 1. Distributed harmonic forcing is applied on the bottom surface of the lower plate representing the liner. This harmonic forcing accounts for the effect of gas pressure in realistic combustor systems. To examine linear mode shapes and natural frequencies of the extended hula seal model, pre-stressed modal analysis was performed with a pre-displacement of 23.2% of h. For boundary conditions, one end (far from the hula seal) of the transition piece and the liner were fixed and the other end (close to the hula seal) were set to be free. The calculated natural frequencies in the frequency range of interest are $f_1 = 33.694$ Hz, $f_2 = 105.03$ Hz, $f_3 = 201.96$ Hz, and

$f_4 = 565.11$ Hz.

TDA with harmonic forcing amplitude 10 lbf was applied to the full-order model for a variety of pre-displacements (y_o = 23.2% of h, y_o = 25.6% of h, and y_o = 30.4% of h). The frequency range of interest was determined to capture the resonant frequency corresponding to target frequency f_1. The ROM for this extended model utilized the parameters identified for a simplified hula seal model since the parameters are concerned only with the hula seal (which is the same for both models) and the contact elements between the hula seal and the plates. In this ROM, the hula seal is like a nonlinear spring connecting the transition piece and liner. To develop the ROM, mass and stiffness matrices for the upper plate (transition piece) and the lower plate (liner) were first obtained using modal analysis. When obtaining those, the boundary conditions used for performing pre-stressed modal analysis were used. The calculated natural frequencies in the frequency range of interest for the transition piece and liner are 100.77 Hz and 31.095 Hz respectively and corresponding mode shape is used to construct the ROMs.

Using the obtained mass and stiffness matrices, the equations of motion for the transition piece and liner are described as

$$\begin{aligned} \mathbf{M}_T\ddot{\mathbf{X}}_T(t) + \mathbf{C}_T\dot{\mathbf{X}}_T(t) + \mathbf{K}_T\mathbf{X}_T(t) - \mathbf{F}_H &= \mathbf{0}, \\ \mathbf{M}_L\ddot{\mathbf{X}}_L(t) + \mathbf{C}_L\dot{\mathbf{X}}_L(t) + \mathbf{K}_L\mathbf{X}_L(t) + \mathbf{F}_H &= \mathbf{F}(t), \end{aligned} \tag{5.5}$$

where the subscript T refers to the transition piece, the subscript L refers to the liner, the subscript H refers to the hula seal, $\mathbf{M}$, $\mathbf{C}$, $\mathbf{K}$ are mass, damping, and stiffness matrices. The damping is modeled as Rayleigh damping (without mass matrix contribution), $\mathbf{C} = \beta\mathbf{K}$, where β is a scalar. $\mathbf{F}$ is the external force, and $\mathbf{F}_H$ is the nonlinear force due to the hula seal. The equation of motion for the transition piece in Eq. (5.5) can be reduced using a single mode shape $\mathbf{\Phi}_T$ computed using the mass and stiffness matrix of the transition

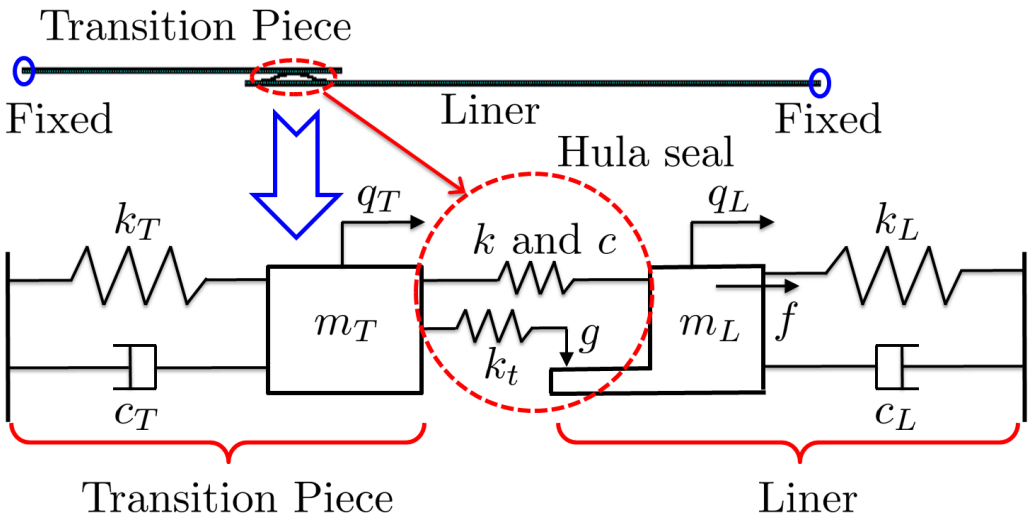

Figure 5.8: A schematic diagram of a ROM for the extended hula seal

piece. Prior to using the mode shape $\mathbf{\Phi}_T$, it is first normalized using the vertical directional modal displacement of a selected node that has contact with the hula seal.

Using modal transformation $\mathbf{X}_T = \mathbf{\Phi}_T q_T$, the equations of motion for the transition piece can be reduced to a single scalar equation. Similarly, the equation of motion for the liner is reduced using mode shape $\mathbf{\Phi}_L$ of the liner which is normalized using the vertical directional modal displacement of a selected node that has contact with the hula seal. The reduced equation of motions for the transition piece and liner are

$$\begin{aligned} m_T\ddot{q}_T(t) + c_T\dot{q}_T(t) + k_T q_T(t) - f_H &= 0, \\ m_L\ddot{q}_L(t) + c_L\dot{q}_L(t) + k_L q_L(t) + f_H &= f(t), \end{aligned} \tag{5.6}$$

where q_T and q_L are modal coordinate for the transition piece and liner, respectively. The nonlinear force f_H due to the hula seal can be described using identified parameters for the hula seal model (i.e., k, g, and k_t). Using these parameters, Eq. (5.6) when the system

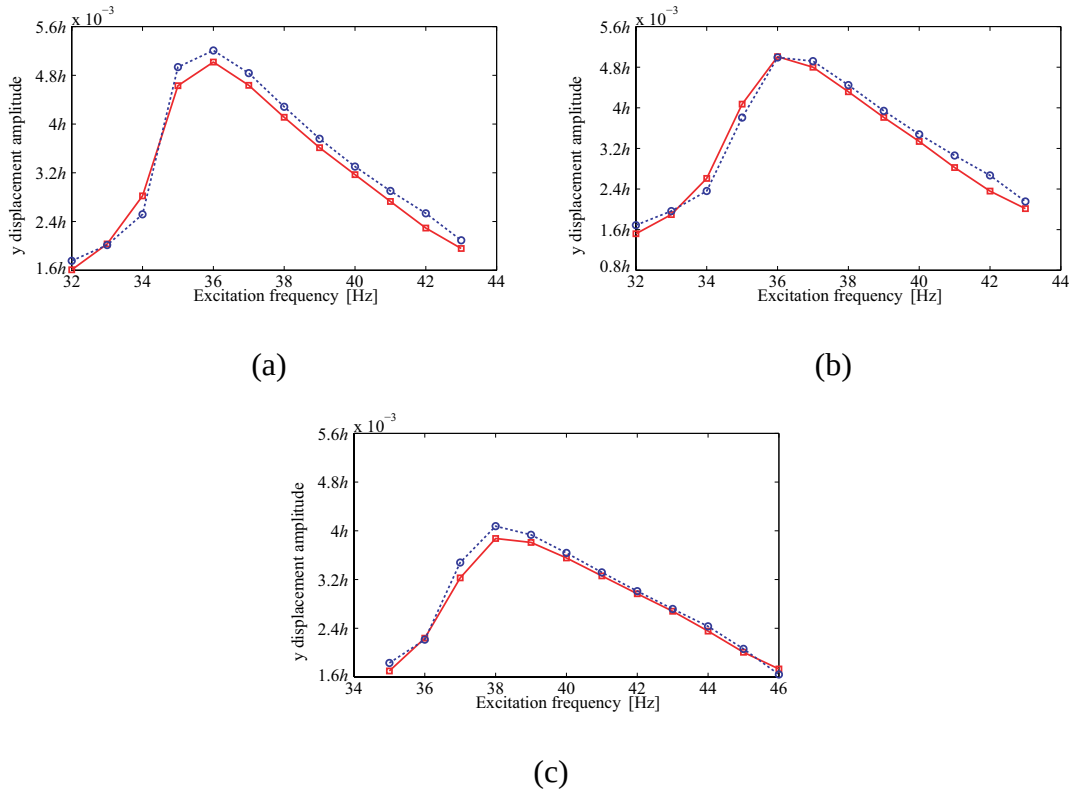

Figure 5.9: Results of ROMs (○) for the extended hula seal model compared to those of TDA (□): (a) pre-displacement y_o = 23.2% of h, (b) pre-displacement y_o = 25.6% of h and (c) pre-displacement y_o = 30.4% of h

is in the sliding state is expressed as

$$\begin{aligned} m_T\ddot{q}_T(t) + c_T\dot{q}_T(t) + k_T q_T(t) - c(\dot{q}_L - \dot{q}_T) - k(q_L - q_T) & \\ -g\ \mathrm{sgn}(\dot{q}) &= 0, \\ m_L\ddot{q}_L(t) + c_L\dot{q}_L(t) + k_L q_L(t) + c(\dot{q}_L - \dot{q}_T) + k(q_L - q_T) & \\ +g\ \mathrm{sgn}(\dot{q}) &= f(t). \end{aligned} \tag{5.7}$$

Eq. (5.6) when the system is in the sticking state is expressed as

$$\begin{aligned} m_T\ddot{q}_T(t) + c_T\dot{q}_T(t) + k_T q_T(t) - c(\dot{q}_L - \dot{q}_T) - k(q_L - q_T) & \\ -k_t((q_L - q_T) - q_c) &= 0, \\ m_L\ddot{q}_L(t) + c_L\dot{q}_L(t) + k_L q_L(t) + c(\dot{q}_L - \dot{q}_T) + k(q_L - q_T) & \\ +k_t((q_L - q_T) - q_c) &= f(t). \end{aligned} \tag{5.8}$$

The schematic diagram describing the ROM for the extended hula seal is shown in Fig. 5.8. The results calculated from the ROM are compared to those of TDA in Fig. 5.9. The displacement amplitudes of the liner plate in the y direction are compared. It was found that the resonant frequencies are higher than the natural frequency f_1. Moreover, it was observed that the resonant frequency shifts to a higher frequency and vibration amplitudes decrease as pre-displacement increases. It can be noted that the maximum error near the resonant frequency is 6.66% at a frequency of 35 Hz when y_o = 23.2% of h, 6.48% at a frequency of 35 Hz when y_o = 25.6% of h, and 5.21% at a frequency of 38 Hz when y_o = 30.4% of h. Based on these results, one can conclude that the ROMs developed for the extended hula seal model accurately predict the nonlinear forced responses of the system.

5.4 Conclusions

An efficient methodology to predict nonlinear responses of dynamic systems with pre-stress and frictional contacts was developed. First, it was verified that the softening non-linearity observed at the interfaces of combustor systems is caused by Coulomb friction using TDA in ANSYS. To develop ROMs for a simplified hula seal model, spatial co-herences of the model were discovered using a POD based method and the system was found to be of a low order. Namely, the system has a single dominant POM. Also, contact parameters which can be obtained from a hysteresis cycle using static analysis were cal-

culated. After completing the investigation of the spatial coherence and obtaining contact parameters, efficient ROMs for a simplified hula seal model were developed and it was validated using TDA in ANSYS. It was shown that the results of the ROMs matched the TDA. After developing the ROMs for a simplified hula seal model, a more realistic hula seal model was introduced. This extended hula seal model has longer plates (which do not have a similar axial length of a real transition piece and liner) than the simplified hula seal model. Using the parameters obtained from the simplified hula seal model, ROMs for the extended model were developed. These ROMs were compared with TDA results, and showed good agreement.

CHAPTER VI

Conclusions and Future Work

6.1 Contributions

The work described in this dissertation proposes efficient methods to accurately analyze vibrations of nonlinear systems and novel techniques to detect damages in bladed disks. The primary contributions of this dissertation are as follows:

- In Chapter II, a novel method to construct multi-stage reduced order models (ROMs) with aerodynamic effects was presented. The method can for the first time efficiently compute many realizations of the structural portion of the system for many different mistuning patterns. The method requires only single sector models of each stage, and uses cyclic symmetry analysis, component mode synthesis (CMM), and a projection of the interstage degrees of freedom onto a set of harmonic basis functions. The aerodynamics are accounted for using the complex aerodynamic matrix for the system, which are calculated separately for each tuned stage. Only a tuned analysis of the flow is necessary due to a new approximation of the complex aerodynamic matrices for mistuned systems, which accounts for the shift in structural frequencies due to mistuning. It can be noted that the proposed approach is general and can be used when other methods are employed to compute the complex

aerodynamic matrix. The interactions of structural and aerodynamic damping, mistuning and multi-stage structural coupling were investigated. It was shown that the aerodynamic damping can have a significant impact on lowering or increasing the vibrational response of the system.

- In Chapter III, a novel methodology to investigate the nonlinear forced response of mistuned bladed disks with a cracked blade was described. Efficient ROMs were constructed from a hybrid component mode synthesis (CMS) and CMM. The forced response of mistuned bladed disks with a cracked blade was obtained by using the proposed models and a hybrid frequency/time domain (HFT) method. It was shown that blade mistuning can be projected efficiently to reduce the computational cost. This is an advantage which plays an important role when the calculation of system normal modes of a mistuned bladed disk is needed for many mistuning patterns. Furthermore, a novel methodology to detect the presence of a crack in mistuned bladed disks was presented. By investigating mode localizations due to cracks and mistuning, and observing that mode shapes of the cracked structure are not a linear combination of tuned system modes, the effects of cracks were differentiated from the effects of mistuning. Based on this result, the proposed method is able for the first time to detect the presence of damage by using tip timing data only even in the presence of nonlinearities caused by cracks. This is accomplished by using the residuals introduced which can be gathered through experimental measurements. They prove to be the key for identifying the presence of damage and even more importantly, statistically detecting the blade where the damage is present even in the presence of measurement noise.

- In Chapter IV, a new methodology to approximate the steady-state amplitude of vi-

bration of a system with piecewise-linear nonlinearity was presented. This method is referred to as bilinear amplitude approximation (BAA). BAA requires only a few linear calculations to compute the mode shapes of linear systems and an overlapping space that is spanned by selected mode shapes. BAA does not require numerical integration to calculate the nonlinear amplitude at resonant frequencies. Therefore, BAA can drastically reduce the computational costs required to obtain the nonlinear resonant amplitude. The method divides each cycle of the steady-state nonlinear response into an open state and a sliding state. The transition between each state is assumed to take place quickly. The method then enforces transitional compatibility at the contacting surfaces, namely that physical displacement and velocities along overlapping space are compatible when the system transitions from the open to sliding states and vice versa. The BAA method was demonstrated for simple systems (i.e., a single-degree-of-freedom system and a three-degree-of-freedom system) as well as a complex system (i.e., a full bladed disk model with a crack). The results were compared against the nonlinear solutions, and a good agreement was found.

- In Chapter V, an efficient methodology to predict nonlinear responses of dynamic systems with pre-stress and frictional contacts was developed. For validation, frictional contacts at interfaces (e.g., those found in combustors between the transition piece and the hula seal, and between the hula seal and the liner) were modeled using contact elements provided in ANSYS. Using transient dynamic analysis (TDA) in ANSYS, it was verified that the softening nonlinearity observed experimentally at the interface of an actual combustor system is caused by Coulomb friction. To develop nonlinear ROMs, spatial coherences in the dynamics of the system were investigated using POD. It was found that the system has dominant spatial coherences. This observation means that it is possible to drastically reduce the size of the

full-order models. Consequently, computational cost savings can be gained when predicting the response of the system to excitations. Contact parameters were obtained from a hysteresis cycle using static analysis. After investigating the spatial coherence and obtaining contact parameters, for the first time efficient ROMs for hula seal models were developed. It was shown that the results of ROMs match those of TDA for the full order system, which indicates that the novel ROMs accurately capture the effects of friction (and micro-slip) in these systems with pre-stress.

6.2 Future Research

The following are suggestions for future research based on the studies presented in this dissertation.

- **Aerodynamic matrices for multi-stage structures**

  The analysis in Chapter II is for a multi-stage structure with the loads from the aerodynamics computed at a stage level. Accounting for the full multi-stage aerodynamics can enhance the accuracy of the forced response predictions. Therefore, future work includes developing a method for efficiently computing multi-stage complex aerodynamic matrices that couple the upstream and downstream stages, and experimental validation of the analysis.

- **Detection of multiple simultaneous damages**

  The damage detection method developed for mistuned bladed disks with a cracked blade in Chapter III utilizes vibration data such as measured displacements. Vibrations of cracked structures can change when there are multiple cracks. The effects of multiple cracks on the vibration characteristics need to be investigated. Consequently, the method developed needs to be validated for mistuned bladed disks

with multiple cracked blades. In addition, the vibration of bladed disks is affected by aerodynamic effects (stiffness and damping) since bladed disks interact with flows in operating conditions. Therefore, vibration analysis for damage detection in bladed disks should consider aerodynamic effects. For accurate and efficient vibration analysis of damaged blade disks experiencing aerodynamic loads, reduced order modeling method addressed in Chapter III can be used.

- **Experimental validation of nonlinear ROMs developed for capturing the effects of Coulomb friction in combustor systems**

  In Chapter V, ROMs for hula seal models were developed using identified contact parameters. To extend this work components with a more complex geometry should be considered while the hula seal model remains the same. After that, experimental validation is desirable.

BIBLIOGRAPHY

BIBLIOGRAPHY

[1] K. D'Souza and B. I. Epureanu. A statistical characterization of the effects of mistuning in multistage bladed disks. *Journal of Engineering for Gas Turbines and Power*, 134(1):012503, 2012.

[2] E. Nissim. Optimization of cascade blade mistuning, Part I: Equations of motion and basic inherent properties. *AIAA Journal*, 23(8):1213–1222, 1985.

[3] E. F. Crawley and K. C. Hall. Optimization and mechanisms of mistuning in cascades. *ASME Journal of Engineering for Gas Turbines and Power*, 107(2):418–426, 1985.

[4] M. Imregun. Prediction of flutter stability using aeroelastic frequency response functions. *Journal of Fluids and Structures*, 9(4):419–434, 1995.

[5] M. Sadeghi and F. Liu. Computation of mistuning effects on cascade flutter. *AIAA Journal*, 39(1):22–28, 2001.

[6] C. Pierre and D. Murthy. Aeroelastic model characteristics of mistuned blade assemblies: Mode localization and loss of eigenstructure. *AIAA Jounal*, 30(10):2483–2496, 1992.

[7] F. Moyroud and T. Fransson. A modal coupling for fluid and structure analyses of turbomachine flutter: Application to a fan stage. In *Proceedings of ASME Turbo Expo*, pages 1–10, 1996.

[8] R. Bladh, M. P. Castanier, and C. Pierre. Component-mode-based reduced order modeling techniques for mistuned bladed disks - Part I: Theoretical models. *Journal of Engineering for Gas Turbines and Power - Transactions of the ASME*, 123(1):89–99, 2001.

[9] R. Bladh, M. P. Castanier, and C. Pierre. Component-mode-based reduced order modeling techniques for mistuned bladed disks - Part II: Application. *Journal of Engineering for Gas Turbines and Power - Transactions of the ASME*, 123:100–108, 2001.

[10] E. Seinturier, C. Dupont, M. Berthillier, and M. Dumas. A new aeroelastic model for mistuned bladed disks. In *Proceedings of the 43rd AIAA/ASME/ASCE/AHS/ASC Structures, Structural Dynamics, and Materials Conference*, volume 4, pages 2628–2638, 2002.

[11] T. S. R. Reddy, J. B. Min, and J. J. Trudell. Mistuned bladed disk analysis with unsteady aerodynamics using Turbo-REDUCE. In *Proceedings of the 46th AIAA/ASME/ASCE/AHS/ASC Structures, Structural Dynamics, and Materials Conference*, pages 2850–2874, 2005.

[12] S.-H. Lim, R. Bladh, M. P. Castanier, and C. Pierre. Compact, generalized component mode mistuning representation for modeling bladed disk vibration. *AIAA Journal*, 45(9):2285–2298, 2007.

[13] Z. He, B. I. Epureanu, and C. Pierre. Fluid-structural coupling effects on the dynamics of mistuned bladed disks. *AIAA Journal*, 45(3):552–561, 2007.

[14] Z. He, B. I. Epureanu, and C. Pierre. Parametric study of the aeroelastic response of mistuned bladed disks. *Computers and Structures*, 85(11-14):852–865, 2007.

[15] A. V. Srinivasan. Flutter and resonant vibration characteristics of engine blades. *Journal of Engineering for Gas Turbines and Power*, 119(4):742–775, 1997.

[16] J. C. Slater, G. R. Minkiewicz, and A. J. Blair. Forced response of bladed disk assemblies - a survey. *Shock and Vibration Digest*, 31(1):17–24, 1999.

[17] M. P. Castanier and C. Pierre. Modeling and analysis of mistuned bladed disk vibration: Status and emerging directions. *Journal of Propulsion and Power*, 22(2):384–396, 2006.

[18] J. T. Wagner. Coupling of turbomachine blade vibrations through the rotor. *Journal of Engineering for Power*, 89(4):502–512, 1967.

[19] R. C. F. Dye and T. A. Henry. Vibration amplitudes of compressor blades resulting from scatter in blade natural frequencies. *Journal of Engineering for Power*, 91(3):182–188, 1969.

[20] D. J. Ewins. The effects of detuning upon the forced vibrations of bladed disks. *Journal of Sound and Vibration*, 9(4):65–79, 1969.

[21] D. J. Ewins. A study of resonance coincidence in bladed discs. *Journal of Mechanical Engineering Science*, 12(5):305–312, 1970.

[22] L. E. El-Bayoumy and A. A. Srinivasan. Influence of mistuning on rotor-blade vibrations. *AIAA Journal*, 13(4):460–464, 1975.

[23] J. H. Griffin and T. M. Hoosac. Model development and statistical investigation of turbine blade mistuning. *Journal of Vibration, Acoustics, Stress, and Reliability in Design*, 106(2):204–210, 1984.

[24] S. T. Wei and C. Pierre. Localization phenomena in mistuned assemblies with cyclic symmetry, part 1: Free vibrations. *Journal of Vibration, Acoustics, Stress, and Reliability in Design*, 110(4):429–438, 1988.

[25] S. T. Wei and C. Pierre. Localization phenomena in mistuned assemblies with cyclic symmetry, part 2: Forced vibrations. *Journal of Vibration, Acoustics, Stress, and Reliability in Design*, 110(4):439–449, 1988.

[26] Ji-Yi Lin and H. S. Cheng. An analytical model for dynamic wear. *Journal of Tribology*, 111:468–474, 1989.

[27] J. A. Kenyon, J. H. Griffin, and D. M. Feiner. Maximum bladed disk forced response from distortion of a structural mode. *ASME J. Turbomach.*, 125(2):352–363, 2002.

[28] A. J. Rivas-Guerra and M. P Mignolet. Maximum amplification of blade response due to mistuning: Localization and mode shapes aspects of the worst disks. *ASME J. Turbomach*, 125(3):442–454, 2003.

[29] A. J. Rivas-Guerra and M. P. Mignolet. Local/global effects of mistuning on the forced response of bladed. *Journal of Engineering for Gas Turbines and Power*, 126(1):131–141, 2004.

[30] A. Madden, M. P. Castanier, and B. I. Epureanu. Reduced-order model construction procedure for robust mistuning identification of blisks. *AIAA Journal*, 46(11):2890–2898, 2008.

[31] D. E. Holland, S. Filippi, M. P. Castanier, S. L. Ceccio, and B. I. Epureanu. Testing and calibration procedures for mistuning identification and traveling wave excitation of blisks. *Journal of Engineering for Gas Turbines and Power*, 132(4):042502, 2010.

[32] Z. He, B. I. Epureanu, and C. Pierre. Convergence predictions for aeroelastic calculations of tuned and mistuned tuned bladed disks. *Journal of Fluids and Structures*, 24(5):732–749, 2008.

[33] J. H. Kuang and B. W. Huang. The effect of blade crack on mode localization in rotating bladed disks. *Journal of Sound and Vibration*, 227(1):85–103, 1999.

[34] J. H. Kuang and B.W. Huang. Mode localization of a cracked blade disk. *Journal of Engineering for Gas Turbines and Power*, 121(2):335–341, 1999.

[35] B. W. Huang and J. H. Kuang. Variation in the stability of a rotating blade disk with a local crack defect. *Journal of Sound and Vibration*, 294(3):486–502, 2006.

[36] X. Fang, J. Tang, E. Jordan, and K. D. Murphy. Crack induced vibration localization in simplified bladed-disk structures. *Journal of Sound and Vibration*, 291(1-2):395–418, 2006.

[37] J. F. Hou. Cracking-induced mistuning in bladed disks. *AIAA Journal*, 44(11):2542–2546, 2006.

[38] D. A. McAdams, D. Comella, and I. Y. Tumer. Exploring effective methods for simulating damaged structures with geometric variation: Toward intelligent failure detection. *Journal of Applied Mechanics-Transactions of the ASME*, 74(2):191–202, 2007.

[39] K. D'Souza, A. Saito, and B. I. Epureanu. Reduced-order modeling for nonlinear analysis of cracked mistuned multistage bladed-disk systems. *AIAA Journal*, 50(2):304–312, 2012.

[40] O. Marinescu, B. I. Epureanu, and M. Banu. Reduced-order models of mistuned cracked bladed disks. *Journal of Vibration and Acoustics*, 133(5):051014, 2011.

[41] A. Saito and B. I. Epureanu. Bilinear modal representations for reduced-order modeling of localized piecewise-linear oscillators. *Journal of Sound and Vibration*, 330:3442–3457, 2011.

[42] M. H. H. Shen and Y. C. Chu. Vibrations of beams with a fatigue crack. *Computers and Structures*, 45:79–93, 1992.

[43] T. G. Chondros, A. D. Dimarogonas, and J. Yao. Vibration of a beam with a breathing crack. *Journal of Sound and Vibration*, 239:57–67, 2001.

[44] N. Pugno, C. Surace, and R. Ruotolo. Evaluation of the non-linear dynamic response to harmonic excitation of a beam with several breathing cracks. *Journal of Sound and Vibration*, 235(5):749–762, 2000.

[45] A. Saito, M. P. Castanier, and C. Pierre. Effects of a cracked blade on mistuned turbine engine rotor vibration. *Journal of Vibration and Acoustics*, 131(6):061006, 2009.

[46] A. Saito, B. I. Epureanu, M. P. Castanier, and C. Pierre. Node sampling for nonlinear vibration analysis of structures with intermittent contact. *AIAA Journal*, 48(9):1903–1915, 2010.

[47] A. Nayfeh and D. Mook. *Nonlinear Oscillations*. John Wiley and Sons, 1979.

[48] J. Guillen and C. Pierre. Analysis of the forced response of dry-friction damped structural systems using an efficient hybrid frequency-time method. *Nonlinear Dynamics and Controls*, DE-91:41–49, 1996.

[49] J. Guillen and C. Pierre. An efficient, hybrid, frequency-time domain method for the dynamics of large-scale dry-friction damped structural systems. *IUTAM Symposium on Unilateral Multibody Contacts*, pages 169–178, 1999.

[50] O. Poudou and C. Pierre. Hybrid frequency-time domain methods for the analysis of complex structural systems with dry friction damping. *Collection of Technical Papers: AIAA/ASME/ASCE/AHS/ASC Structures, Structural Dynamics and Materials Conference*, 1:111–124, 2003.

[51] M. C. C. Bampton and R. R. Craig. Coupling of substructures for dynamic analyses. *AIAA Journal*, 6(7):1313–1319, 1968.

[52] O. Poudou, C. Pierre, and B. Reisser. A new hybrid frequency-time domain method for the forced vibration of elastic structures with friction and intermittent contact. *Proceedings of the Tenth International Symposium on Transport Phenomena and Dynamics of Rotating Machinery*, 2004. Paper No. ISROMAC10-2004-068.

[53] O. Poudou and C. Pierre. A new method for the analysis of the nonlinear dynamics of structures with cracks. *Proceedings of NOVEM 2005*, 2005.

[54] A. Saito, M. P. Castanier, C. Pierre, and O. Poudou. Efficient nonlinear vibration analysis of the forced response of rotating cracked blades. *Journal of Computational and Nonlinear Dynamics*, 4(1):011005, 2009.

[55] I. B. Carrington, J. R. Wright, J. E. Cooper, and G. Dimitriadis. A comparison of blade tip timing data analysis methods. *Proc. Inst. Mech. Eng. Part G J. Aerosp. Eng.*, 215(5):301–312, 2001.

[56] W. C. Hurty. Dynamic analysis of structural systems using component modes. *AIAA Journal*, 3(4):678–685, 1965.

[57] M. T. Yang and J. H. Griffin. A reduced-order model of mistuning using a subset of nominal system modes. *Journal of Engineering for Gas Turbines and Power - Transactions of the ASME*, 123:893–900, Oct. 2001.

[58] R. Bladh, M. P. Castanier, and C. Pierre. Effects of multistage coupling and disk flexibility on mistuned bladed disk dynamics. *Journal of Engineering for Gas Turbines and Power - Transactions of the ASME*, 125(1):121–130, 2003.

[59] Alok Sinha. Reduced-order model of a mistuned multi-stage bladed rotor. *International Journal of Turbo and Jet Engines*, 25(3):145–153, 2008.

[60] Sang Heon Song, Matthew P. Castanier, and Christophe Pierre. Multi-stage modeling of turbine engine rotor vibration. In *Proceedings of the ASME 2005 Design Engineering Technical Conference and Computers and Information in Engineering Conference*, Long Beach, CA, USA, September 2005. DETC2005-85740.

[61] Sang Heon Song, Matthew P. Castanier, and Christophe Pierre. System identification of multistage turbine engine rotors. In *Proceedings of GT2007 ASME Turbo Expo*, Montreal, Canada, May 2007. GT2007-28307.

[62] Sang Heon Song. *Vibration Analysis and System Identification of Mistuned Multistage Turbine Engine Rotors*. PhD thesis, The University of Michigan, 2007.

[63] Denis Laxalde, Jean-Pierre Lombard, and Fabrice Thouverez. Dynamics of multistage bladed disks systems. *Journal of Engineering for Gas Turbines and Power*, 129(4):1058–1064, 2007.

[64] D. Laxalde, F. Thouverez, and J.-P. Lombard. Dynamical analysis of multi-stage cyclic structures. *Mechanics Research Communications*, 34(4):379–384, 2007.

[65] Eric Chatelet, Flavio D'Ambrosio, and Georges Jacquet-Richardet. Toward global modeling approaches for dynamic analyses of rotating assemblies of turbomachines. *Journal of Sound and Vibration*, 282(1-2):163–178, 2005.

[66] R. Rzadkowski and J. Sokolowski. Coupling effects between the shaft and two bladed-discs. *Advances in Vibration Engineering*, 4(3):249–266, 2005.

[67] Özgür Turhan and Gökhan Bulut. Linearly coupled shaft-torsional and blade-bending vibrations in multi-stage rotor-blade systems. *Journal of Sound and Vibration*, 296(1-2):292–318, 2006.

[68] Bartolomè Seguì and Euro Casanova. Application of a reduced order modeling technique for mistuned bladed disk-shaft assemblies. In *Proceedings of GT2007 ASME Turbo Expo*, May 2007. GT2007-27594.

[69] Romuald Rzadkowski and Marcin Drewczynski. Coupling of vibration of several bladed discs on the shaft, part i: Free vibration analysis. *Advances in Vibration Engineering*, 8(2):125–137, 2009.

[70] D. S. Whitehead. The vibration of cascade blades treated by actuator disk methods. In *Proceedings of the Institution of Mechanical Engineering*, volume 173, pages 555–557, 1959.

[71] F. O. Carta. Coupled blade-disk-shroud flutter instabilities in turbojet engine rotors. *Journal of Engineering for Power*, 89(3):419–426, 1967.

[72] M. Karpel. Design for active flutter suppression and gust alleviation using state-space aeroelastic modeling. *AIAA Journal of Aircraft*, 19(3):221–227, 1982.

[73] T. Udea and E. H. Dowell. Flutter analysis using nonlinear aerodynamic forces. *AIAA Journal of Aircraft*, 21:101–109, 1984.

[74] J. G. Marshall and M. Imregun. A review of aeroelasticity methods with emphasis on turbomachinery applications. *Journal of Fluids and Structures*, 10(3):237–267, 1996.

[75] D. B. Kholodar, J. P. Thomas, E. H. Dowell, and K. C. Hall. Parametric study of flutter for an airfoil in inviscid transonic flow. *Journal of Aircraft*, 40(2):303–313, 2003.

[76] U. Iemma and M. Gennaretti. Reduced-order modeling for linearized aeroelasticity of fixed wings in transonic flight. *Journal of Fluids and Structures*, 21(3):243–255, Nov 2005.

[77] J. P. Thomas, E. H. Dowell, and K. C. Hall. Static/dynamic correction approach for reduced-order modeling of unsteady aerodynamics. *Jourrnal of Aircraft*, 43(4):865–878, 2006.

[78] F. Sabri and A. A. Lakis. Hybrid finite element method applied to supersonic flutter of an empty or partially liquid-filled truncated conical shell. *Journal of Sound and Vibration*, 329(3):302–316, Feb 2010.

[79] Z. He. *Effects of Aeroelastic Phenomena on the Vibration Localization in Mistuned Bladed Disks*, PhD Thesis. Mechanical Engineering Department, University of Michigan, 2007.

[80] T. H. Fransson and J. M. Verdon. Updated report on standard configurations for unsteady flow through vibrating axial-flow turbomachine cascades: Status as of July 1991. Technical report, Royal Institute of Technology, Stockholm, Sweden and United Technologies Research Center, East Hartford, Connecticut, USA, 1992.

[81] T. H. Fransson, M. Jöcker, A. Bölcs, and P. Ott. Viscous and inviscid linear/nonlinear calculations versus quasi-three-dimensional experimental cascade data for a new aeroelastic turbine standard configuration. *Journal of Turbomachinery*, 121(4):717–725, 1999.

[82] B. I. Epureanu, E. H. Dowell, and K. C. Hall. Mach number influence on reduced order models of inviscid potential flows in turbomachinery. *Journal of Fluids Engineering*, 124(4):977–987, 2002.

[83] K. C. Hall. Deforming grid variational principle for unsteady small disturbance flows in cascades. *AIAA Journal*, 31(5):891–900, 1993.

[84] J. S. Parkinson and R. J. Wynne. Reduced-order modeling and state estimation applied to gas distribution systems. *IEEE Transactions on Automatic Control*, AC-31(8):701–708, 1986.

[85] J. V. Ramakrishnan, S. V. Rao, and L. R. Koval. Reduced-order modeling of flexible structures. *Journal of Guidance*, 11(5):459–464, 1988.

[86] K. Tsuchiya, T. Kashiwase, and K. Yamada. Reduced-order models of a large flexible spacecraft. *Journal of Guidance*, 12(6), 1989.

[87] B. Yang and H. Chen. Redued-order shaft system models of turbogenerators. *IEEE Transactions on Power Systems*, 8(3):1366–1374, 1993.

[88] D. Tang, M. D. Conner, and E. H. Dowell. Reduced-order aerodynamic model and its application to a nonlinear aeroelastic system. *Journal of Aircraft*, 35(2):332–338, 1998.

[89] M. A. Mohiuddin, M. Bettayeb, and Y. A Khulief. Dynamic analysis and reduced order modelling of flexible rotor-bearing systems. *Computers and Structures*, 69:349–359, 1998.

[90] R. Bladh, M. P. Castanier, and C. Pierre. Reduced order modeling and vibration analysis of mistuned bladed disk assemblies with shrouds. *Journal of Engineering for Gas Turbines and Power*, 121:515–522, 1999.

[91] M. I. Friswell and D. J. Inman. Reduced-order models of structures with viscoelastic components. *AIAA Journal*, 37(10):1318–1325, 1999.

[92] D. F. Li and E. J. Gunter. Compenet mode synthesis of large rotor systems. *Journal of Engineering for Power-Transactions of the ASME*, 104:552–560, 1982.

[93] J. Moon and D. Cho. A component mode synthesis applied to mechanisms for an investigation of vibration. *Journal of Sound and Vibration*, 157:67–79, 1992.

[94] M. I. Friswell, J. E. T. Penny, and S. D. Garvey. Using linear model reduction to investigate the dynamics of structures with local non-linearities. *Mechanical Systems and Signal Processing*, 9:317–328, 1995.

[95] M. I. Friswell, J. E. T. Penny, and S. D.. Garvey. The application of the irs and balanced realization methods to obtain reduced models of structures with local non-linearity. *Journal of Sound and Vibration*, 196:453–468, 1996.

[96] D. J. Segalman. Model reduction of systems with localized nonlinearities. *Journal of Computational and Nonlinear Dynamics*, 2:249–266, 2007.

[97] E. A. Butcher and R. Lu. Order reduction of structural dynamic systems with static piecewise linear nonlinearities. *Nonlinear Dynamics*, 49:375–399, 2007.

[98] S. L. Chen and S. W. Shaw. Normal modes for piecewise linear vibratory systems. *Nonlinear Dynamics*, 10:135–164, 1996.

[99] D. Jiang, C. Pierre, and S. W. Shaw. Large-amplitude non-linear normal modes of piecewise linear systems. *Journal of Sound and Vibration*, 272:869–891, 2004.

[100] P. Apiwattanalunggarn, S. W. Shaw, and C. Pierre. Component mode synthesis using nonlinear normal modes. *Nonlinear Dynamics*, 41:17–46, 2005.

[101] Chulwoo Jung, Akira Saito, and Bogdan I. Epureanu. Detection of cracks in mistuned bladed disks using reduced-order models and vibration data. *Journal of Vibration and Acoustics*, 134:061010, 2012.

[102] S. W. Shaw and P. J. Holmes. A periodically forced piecewise linear oscillator. *Journal of Sound and Vibration*, 90(1):129–155, 1983.

[103] Ernest Rabinowicz. The least wear. *Wear*, 100:533–541, 1984.

[104] O. S. Dinc, R. Cromer, and S. J. Calabrese. Redesigning mechanical systems for low wear using system dynamics modeling. *Journal of Tribology*, 118:415–422, 1996.

[105] J. H. Griffin. Friction damping of resonant stresses in gas turbine engine airfoils. *Journal of Engineering for Power*, 102:329–333, 1980.

[106] B. D. Yang, M. L. Chu, and C. H. Menq. Stick-slip-separation analysis and non-linear stiffness and damping characterization of friction contacts having variable normal load. *Journal of Sound and Vibration*, 210(4):461–481, 1998.

[107] K. Y. Sanliturk and D. J. Ewins. Modelling two-dimensional friction contact and its application using harmonic balance method. *Journal of Sound and Vibration*, 193(2):511–523, 1996.

[108] C. H. Menq and B. D. Yang. Non-linear spring resistance and friction damping of frictional constraint having two-dimensional motion. *Journal of Sound and Vibration*, 217(1):127–143, 1998.

[109] B. D. Yang and C. H. Menq. Characterization of 3d contact kinematics and prediction of resonant response of structures having 3d frictional constraint. *Journal of Sound and Vibration*, 217(5):909–925, 1998.

[110] Sergio Filippi, Adnan Akay, and Muzio M. Gola. Measurement of tangential contact hysteresis during microslip. *Journal of Tribology*, 126:482–489, 2004.

[111] K. H. Koh, J. H. Griffin, S. Filippi, and A. Akay. Characterization of turbine blade friction dampers. *Journal of Engineering for Gas Turbines and Power*, 127:856–862, 2005.

[112] Ender Cigeroglu, Ning An, and Chia-Hsiang Menq. A microslip friction model with normal load variation induced by normal motion. *Nonlinear Dynamics*, 50:609–626, 2007.

[113] M. Allara. A model for the characterization of friction contacts. *Journal of Sound and Vibration*, 320:527–544, 2009.

[114] Ulf Sellgre and Ulf Olofsson. Application of a constitutive model for micro-slip in finite element analysis. *Computer Methods in Applied Mechanics and Engineering*, 170:65–77, 1999.

[115] E. P. Petrov and D. J. Ewins. Analytical formulation of friction interface elements for analysis of nonlinear multi-harmonic vibrations of bladed disks. *Journal of Turbomachinery*, 125:364–371, 2003.

[116] Stefano Zucca, Juan Borrajo, and Muzio M. Gola. Forced response of bladed disks in cyclic symmetry with underplatform dampers. *Proceedings of ASME Turbo Expo*, 2006. Barcelona, Spain, Paper No. GT2006-90785.

[117] B. F. Feeny. On proper orthogonal co-ordinates as indicators of modal activity. *Journal of Sound and Vibration*, 255(5):805–817, 2002.

[118] J. C. Simo and T. A. Laursen. An augmented lagrangian treatment of contact problems involving friction. *Computers and Structures*, 42(1):97–116, 1992.